nature cell biology

Article

https://doi.org/10.1038/s41556-024-01489-6

RNA sequestration in P-bodies sustains myeloid leukaemia

Received: 18 September 2023

Accepted: 18 July 2024

Published online: 21 August 2024

Check for updates

Srikanth Kodali[1,2,3,4,5,20], Ludovica Proietti[6,20], Gemma Valcarcel[7], Anna V. López-Rubio[7], Patrizia Pessina[1,2,3,4,5], Thomas Eder[6], Junchao Shi[8], Annie Jen[9], Núria Lupión-Garcia[1,2,3,4,5], Anne C. Starner[10], Mason D. Bartels[10], Yingzhi Cui[1,2,3,4,5], Caroline M. Sands[1,2,3,4,5], Ainoa Planas-Riverola[7], Alba Martínez[7], Talia Velasco-Hernandez[7], Laureano Tomás-Daza[7], Bernhard Alber[6], Gabriele Manhart[6], Isabella Maria Mayer[11], Karoline Kollmann[11], Alessandro Fatica[12], Pablo Menendez[7], Evgenia Shishkova[9,13], Rachel E. Rau[1,2,3,14], Biola M. Javierre[7], Joshua Coon[9,13,15,16], Qi Chen[17], Eric L. Van Nostrand[10], Jose L. Sardina[7] ✉, Florian Grebien[6,18,19] ✉ & Bruno Di Stefano[1,2,3,4,5] ✉

Post-transcriptional mechanisms are fundamental safeguards of progenitor cell identity and are often dysregulated in cancer. Here, we identified regulators of P-bodies as crucial vulnerabilities in acute myeloid leukaemia (AML) through genome-wide CRISPR screens in normal and malignant haematopoietic progenitors. We found that leukaemia cells harbour aberrantly elevated numbers of P-bodies and show that P-body assembly is crucial for initiation and maintenance of AML. Notably, P-body loss had little effect upon homoeostatic haematopoiesis but impacted regenerative haematopoiesis. Molecular characterization of P-bodies purified from human AML cells unveiled their critical role in sequestering messenger RNAs encoding potent tumour suppressors from the translational machinery. P-body dissolution promoted translation of these mRNAs, which in turn rewired gene expression and chromatin architecture in leukaemia cells. Collectively, our findings highlight the contrasting and unique roles of RNA sequestration in P-bodies during tissue homoeostasis and oncogenesis. These insights open potential avenues for understanding myeloid leukaemia and future therapeutic interventions.

Acute myeloid leukaemia (AML) is a highly aggressive blood cancer characterized by the uncontrolled growth of immature myeloblasts arrested in differentiation[1]. Its genetic complexity and diversity have made treatment challenging, causing 5-year survival rates to languish at ~30%[1]. Thus, a deeper mechanistic understanding of AML biology is required to identify additional molecular vulnerabilities of this disease and develop precision therapies.

Leukaemic transformation requires subversion of gene expression programmes maintaining haematopoietic cell identity. Cell type-specific gene expression is influenced by post-transcriptional mechanisms that orchestrate the protein output of the cellular transcriptome. Dysregulated protein synthesis has emerged as a hallmark of oncogenic transformation, with malignant cells reprogramming the translation of messenger RNAs that modulate cell survival and proliferation[2]. Nevertheless, the precise mechanisms by which leukaemia cells manipulate mRNA translation remain poorly understood. Moreover, the crosstalk between mRNA translation and the organization of chromatin architecture in driving leukaemia cell survival remains largely unexplored.

A full list of affiliations appears at the end of the paper. ✉e-mail: jsardina@carrerasresearch.org; Florian.Grebien@vetmeduni.ac.at; bruno.distefano@bcm.edu

The subcellular localization of RNA molecules influences their post-transcriptional fates, including their translation rate[3]. RNAs can be targeted to membrane-less ribonucleoprotein (RNP) condensates that vary in form, function and location[4]. P-bodies are RNP condensates that form when RNAs, RNA-binding proteins (RBPs) and scaffold proteins condense together in the cytoplasm. While initially thought to be sites for mRNA decay[5], recent evidence suggests that P-bodies serve as reservoirs that selectively sequester untranslated mRNAs from the translation machinery[6–11]. Congruently, mRNAs stored in P-bodies can re-enter translation in response to changing cellular conditions[7,9,12]. For instance, triggering P-body dissolution in *Caenorhabditis elegans* oocytes releases a burst of mRNAs available for translation, dramatically increasing their cytosolic concentration (~ninefold)[13]. In stem and progenitor cells, P-bodies sequester mRNAs coding for key fate-instructive regulators that influence cellular plasticity[8]. Furthermore, emerging research indicates that P-bodies contribute to human diseases[14]. In cancer, P-body components have been shown to be aberrantly expressed[15–18], suggesting that altered RNA sequestration may contribute to the destabilization of cell identity and modulate oncogenesis across tissue types. However, the implications of the interplay between translation suppression, RNA sequestration in P-bodies and cancer have not yet been explored.

In this study, we conducted unbiased CRISPR/Cas9 screens in both healthy and malignant haematopoietic progenitors, identifying post-transcriptional regulators linked to translational suppression and P-body formation as specific dependencies in myeloid leukaemia. Additionally, we uncovered dysregulated P-body homoeostasis in AML. Mechanistically, we discovered that AML cells hijack P-body function to sequester and translationally repress mRNAs encoding potent tumour-suppressive epigenetic and transcriptional regulators, thereby promoting the establishment of leukaemic chromatin and transcriptional landscapes. Our findings establish a molecular node between mRNA translation, storage in P-bodies and chromatin remodelling in the nucleus of leukaemia cells, which could potentially be exploited to design precision therapies for AML and other malignancies.

Results

P-body homoeostasis is dysregulated in AML

To uncover genetic vulnerabilities in AML, we performed parallel genome-wide CRISPR dropout screens in mouse leukaemia cells (*Cebpa*$^{N\text{-mut/C-mut}}$ (CNC), modelling AML with biallelic *CEBPA* mutations) and the normal haematopoietic stem and progenitor cell line, HPC7 (Extended Data Fig. 1a,b and Supplementary Table 1)[19,20]. We found 308 genes required for survival in CNC cells but not HPC7 cells (Fig. 1a, Extended Data Fig. 1c and Supplementary Table 1). Gene Ontology (GO) analysis of these hits revealed enrichment for post-transcriptional regulators linked to translational repression and P-bodies (Fig. 1b and Supplementary Table 1)[21]. We verified the AML-specific essentiality of several top hits through competitive growth assays in CNC and HPC7 cells (Extended Data Fig. 1d,e). Overall, our screens raise the intriguing possibility that leukaemia cells might rely on P-body-linked translation control.

We next investigated whether P-body-associated genes might be dysregulated in human AML. Surveying cancer gene expression datasets revealed several of these genes to be upregulated in AML cells compared with normal haematopoietic stem and progenitor cells (HSPCs) (Fig. 1c and Extended Data Fig. 1f). Analysis of published chromatin immunoprecipitation (ChIP)-seq data (GSM1003586)[22] indicated increased levels of H3K27ac, an active chromatin-related histone mark, at enhancers and promoters of P-body-associated genes in AML cells compared with normal HSPCs (Extended Data Fig. 1g). Importantly, elevated expression of *DDX6* and *EIF4ENIF1*, which encode two key proteins indispensable for the translational repression and sequestration of mRNAs in P-bodies[11], was correlated and associated with worse survival in patients with AML (Fig. 1c and Extended Data Fig. 1h–j). *DDX6* was also overexpressed in AML, compared with other cancers, and across different cytogenetic subtypes relative to normal HSPCs (Extended Data Fig. 1k–m).

Finally, we examined whether differential expression of P-body-associated genes might correlate with differences in P-body numbers. Indeed, leukaemia cells across patients with AML harboured significantly more P-bodies than normal HSPCs, based on immunocytochemistry for the P-body markers DDX6 and EDC4 (ref. 23) (Fig. 1d,e and Supplementary Table 3). This is consistent with our finding that *DDX6* overexpression is sufficient to increase P-body numbers in haematopoietic progenitor cells (Extended Data Fig. 2a,b).

Our data reveal dysregulated P-body homoeostasis in AML cells. Together with the results of our parallel CRISPR screens, these findings raise the intriguing possibility that RNA sequestration within P-bodies might play a key role in myeloid leukaemia.

Fig. 1 | P-body regulators are AML dependencies. a, Comparative analysis of genome-wide CRISPR/Cas9 dropout screens in normal haematopoietic progenitor cells (HPC7 Cas9) and *Cebpa*$^{N\text{-mutant/C-mutant}}$ leukaemia cells (CNC Cas9). Axes show enrichment/depletion as $\log_2$ FC. Blue dots represent genes that selectively impair ($\log_2$FC < −0.5) CNC Cas9 cell proliferation. Grey dots represent all other genes. **b**, GO biological processes and cellular components enrichment analyses of genes identified as specific dependencies of murine leukaemia cells. Two-tailed Fisher's exact test. **c**, mRNA expression of P-body-related genes in AML compared with healthy tissue, based on data from The Cancer Genome Atlas (TCGA) database. Data are presented as mean $\log_2$ expression with range. **d**, Representative immunofluorescence (IF) imaging of EDC4 (green) and DDX6 (red) punctae in primary CD34$^+$ cells and AML patient cells. Nuclei were counterstained with DAPI (blue). Scale bar, 10 µm. **e**, Quantification of EDC4$^+$DDX6$^+$ punctae in two primary CD34$^+$ samples and four AML patient samples by IF. CD34$^+$ #1 (n = 20 cells), CD34$^+$ #2 (n = 28 cells), AML #1 (n = 50 cells), AML #2 (n = 42 cells), AML #3 (n = 66 cells), AML #4 (n = 22 cells), one-way analysis of variance (ANOVA) with Dunnett's post-hoc correction, mean ± s.e.m. **f**, Representative IF imaging of EDC4 (green) and DDX6 (red) punctae in control and *DDX6* KD MOLM-13 cells. Nuclei were counterstained with DAPI (blue). Scale bar, 10 µm. **g**, Quantification of EDC4$^+$DDX6$^+$ punctae in control and *DDX6* KD MOLM-13 cells by IF. Unpaired two-tailed Student's t-test, n = 24–30 cells per group, mean ± s.e.m. **h**, Proliferation assay for shCTRL and shDDX6 MOLM-13 cells at the indicated time points after transduction. Two-way ANOVA with Dunnett's post-hoc test, n = 3 biologically independent samples, mean ± s.e.m. **i**, Flow cytometric analysis of myeloid differentiation in MOLM-13 cells 7 d after *DDX6* silencing (CD68 and CD123 MFI). Unpaired two-tailed Student's t-test, n = 3 biologically independent samples, mean ± s.e.m. **j**, Heatmap of RNA-seq data for shCTRL and shDDX6 MOLM-13 cells (n = 2 biologically independent samples, FC > 1.5; P < 0.05, Wald test with Benjamini–Hochberg correction). Upregulated genes are depicted in red and blue depicts downregulated genes. **k**, GO enrichment analysis of differentially expressed genes in control versus *DDX6* KD MOLM-13 cells. Two-tailed Fisher's exact test. **l**, Representative IF imaging of EDC4 (green) and DDX6 (red) punctae in control, *LSM14A* and *EIF4ENIF1* KD MOLM-13 cells. Nuclei were counterstained with DAPI (blue). Scale bar, 10 µm. **m**, Quantification of EDC4$^+$DDX6$^+$ punctae in control, *LSM14A* and *EIF4ENIF1* KD MOLM-13 cells by IF. Unpaired two-tailed Student's t-test, n = 17–31 cells per group, mean ± s.e.m. **n**, Cell numbers 9 d after shRNA-mediated silencing of *LSM14A* and *EIF4ENIF1* in MOLM-13 cells. Unpaired two-tailed Student's t-test, n = 3 biologically independent samples, mean ± s.e.m. **o**, Schematic showing homozygous insertion of FKBP12^{F36V}-HA-P2A-mCherry sequence into the stop codon of the endogenous *DDX6* allele of Cas9-expressing MOLM-13 cells (top). Representative western blot showing HA-tagged endogenous DDX6 protein levels in DDX6-FKBP12^{F36V} MOLM-13 cells at the indicated time points following dTAG-13 treatment (bottom). n = 3 independent experiments. **p**, Proliferation of DDX6-FKBP12^{F36V} MOLM-13 cells cultured in the presence of the indicated concentrations of dTAG-13 for 5 d. n = 3 biologically independent samples, mean ± s.e.m. **q**, Schematic of dTAG-13 administration and washout for DDX6-FKBP12^{F36V} MOLM-13 cells. In brief, DDX6-FKBP12^{F36V} MOLM-13 cells were either vehicle-treated (DMSO), continuously treated with 1 µM dTAG-13 or treated with 1 µM dTAG-13 for 2, 5 or 6 days, followed by washout and culture. **r**, Proliferation of DDX6-FKBP12^{F36V} MOLM-13 cells treated as in **q**, n = 3 biologically independent samples, mean ± s.e.m. KD, knockdown; DAPI, 4,6-diamidino-2-phenylindole; DMSO, dimethylsulfoxide; MFI, median fluorescence intensity; CTRL, control.

https://doi.org/10.1038/s41556-024-01489-6

P-body regulators are crucial for AML cell survival

Given its role in translational suppression and its absolute requirement for P-body assembly[11,21,24], we next examined the functional role of DDX6 in human AML cells. We initially confirmed DDX6's cytoplasmic localization (Extended Data Fig. 2c) and enrichment within P-bodies, based on colocalization with the P-body markers EDC4 or LSM14A[21], in AML cells (Fig. 1f,g and Extended Data Fig. 2d,e). Next, we silenced *DDX6* in human AML cell lines of varying subtype and mutations (MOLM-13, HEL, SKM-1, THP-1, MV411 and HL-60)[25,26] (Supplementary Table 4). shRNA-mediated knockdown, CRISPR/Cas9-mediated knockout and CRISPR interference (CRISPRi)-mediated silencing of *DDX6* triggered P-body dissolution and impaired proliferation across AML cell lines (Fig. 1f–h and Extended Data Fig. 2f–n). Furthermore, *DDX6* suppression triggered myeloid differentiation in the acute monocytic leukaemia line MOLM-13 and megakaryocytic differentiation in the erythroleukaemia line HEL and induced apoptosis in multiple AML cell lines (Fig. 1i and Extended Data Figs. 2o,p and 3a). Together, these data indicate that DDX6 sustains human AML cells.

We next examined gene expression changes induced by *DDX6* silencing in the cytogenetically distinct AML lines MOLM-13 and HL-60 by RNA-seq (Fig. 1j and Extended Data Fig. 3b–d). We observed mRNAs downregulated in *DDX6*-depleted cells to be enriched for factors

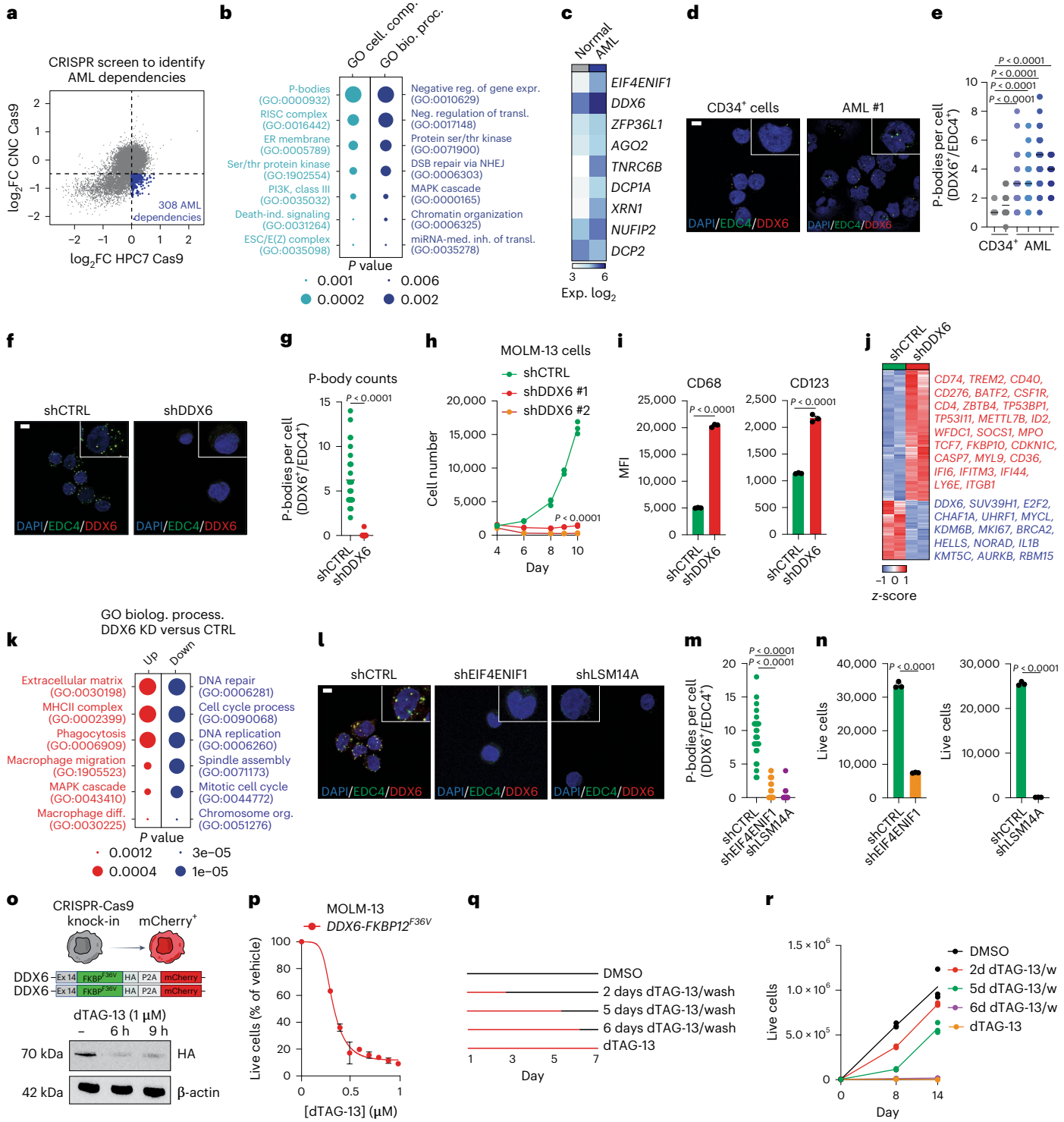

https://doi.org/10.1038/s41556-024-01489-6

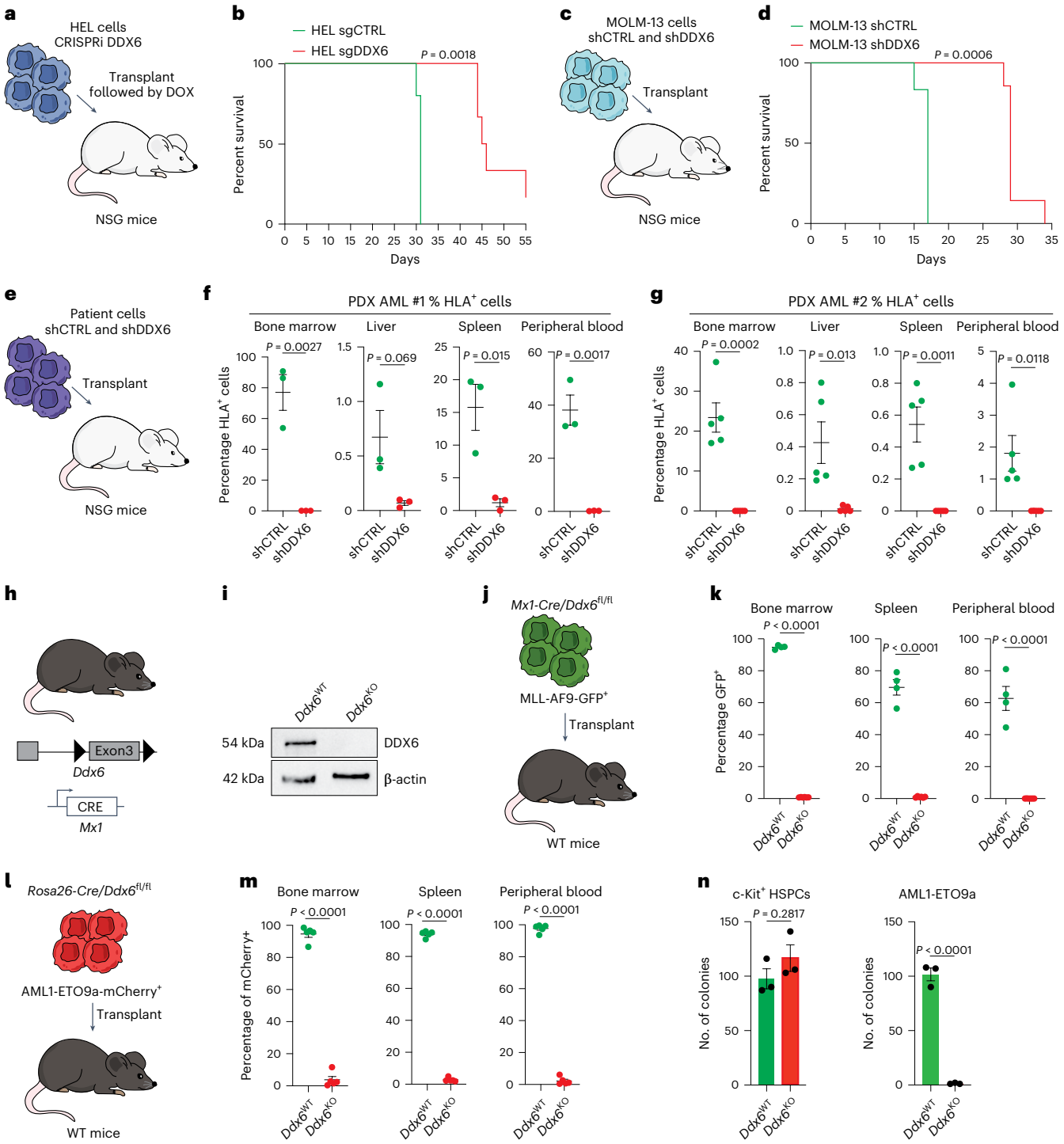

Fig. 2 | DDX6 is crucial for human and mouse AML progression in vivo. a, NSG mice were injected with sgCTRL or sgDDX6 CRISPRi HEL cells and placed on a doxycycline (DOX) diet 7 d later. **b**, Kaplan–Meier survival curves of NSG mice transplanted as in **a** are shown. Mantel–Cox test, sgCTRL $n = 5$ mice, sgDDX6 $n = 6$ mice. **c**, NSG mice were injected with shCTRL or shDDX6 MOLM-13 AML cells. **d**, Kaplan–Meier survival curves of NSG mice transplanted with shCTRL or shDDX6 MOLM-13 cells. Mantel–Cox test, shCTRL $n = 6$ mice, shDDX6 $n = 7$ mice. **e**, NSG mice were injected with shCTRL or shDDX6 patient primary AML cells. **f**,**g**, Percentages of control or *DDX6* KD AML cells in the indicated organs of NSG mice at 60 d post-transplant, quantified by flow cytometry. Unpaired two-tailed Student's *t*-test, $n = 3$ mice per group, mean ± s.d. **h**, Schematic of the *Ddx6*$^{fl/fl}$ transgenic mice and breeding strategy. **i**, Representative western blot analysis for DDX6 in c-Kit$^+$ haematopoietic progenitor cells. $n = 3$ independent experiments. **j**, c-Kit$^+$ bone-marrow cells from *Mx1-Cre* or *Mx1-Cre*/*Ddx6*$^{fl/fl}$ mice were transduced with MLL-AF9 and transplanted into WT recipient mice, followed by poly(I:C) treatment 3 weeks later. **k**, Percentages of transduced CD45$^+$ cells (GFP$^+$) in the indicated organs at 90 d post-transplantation. Unpaired two-tailed Student's *t*-test, *Ddx6*^{WT} $n = 4$ mice, *Ddx6*^{KO} $n = 6$ mice, mean ± s.e.m. **l**, c-Kit$^+$ bone-marrow cells from *Rosa26-Cre* or *Rosa26-Cre*/*Ddx6*$^{fl/fl}$ mice were transduced with AML1-ETO9a and transplanted into WT recipient mice, followed by tamoxifen treatment 3 weeks later. **m**, Percentages of transduced CD45$^+$ cells (mCherry$^+$) in the indicated organs at 48 d post-transplantation. Unpaired two-tailed Student's *t*-test, *Ddx6*^{WT} $n = 5$, *Ddx6*^{KO} $n = 5$ mice per group, mean ± s.e.m. **n**, Colony-forming assay of *Ddx6*^{WT} and *Ddx6*^{KO} (left) normal c-Kit$^+$ HSPCs or (right) AML1-ETO9a$^+$ leukaemic cells. Cells were plated 2 d after 4-hydroxytamoxifen treatment and colony-forming units were counted 7 d later. Unpaired two-tailed Student's *t*-test, $n = 3$ biologically independent samples, mean ± s.e.m.

important for chromatin organization and cell cycle progression, including *CHAF1B*, *UHRF1*, *MKI67* and *AURKB* (Fig. 1j,k and Extended Data Fig. 3c,e). In contrast, upregulated genes were enriched for mediators of myeloid differentiation and function, including *CD40*, *CD14*, *IRF8* and the tumour suppressors *CDKN1A* and *ID2* (Fig. 1j,k and Extended Data Fig. 3c,e). Together, these data underscore the pivotal role of DDX6 in maintaining AML-associated gene expression programmes.

We then evaluated whether depletion of other translation repressors necessary for P-body assembly could replicate the phenotypes observed upon *DDX6* suppression. Indeed, suppression of *EIF4ENIF1* and *LSM14A*[11] resulted in P-body loss and growth arrest in MOLM-13 cells to a similar extent as *DDX6* knockdown (Fig. 1l–n and Extended Data Fig. 3f,g). These results highlight the essential contribution of P-body regulators to AML cell survival.

To explore the potential of fine-tuning DDX6 protein levels, we established a model for ligand-induced, reversible DDX6 degradation via homozygous CRISPR/Cas9-mediated knock-in of a FKBP12^{F36V}-HA-P2A-mCherry cassette into the *DDX6* locus in MOLM-13 and HL-60 cells (Fig. 1o). Using dTAG-13 (ref. 27), we achieved rapid, efficient and reversible DDX6 protein degradation in these cells within 6 h (Fig. 1o and Extended Data Fig. 3h), with even low concentrations of dTAG-13 (62.5 nM) attenuating proliferation (Fig. 1p). Continuous dTAG-13 treatment for 6 days irreversibly suppressed AML cell proliferation, as re-expression of DDX6 failed to rescue the initial proliferation defect (Fig. 1q,r and Extended Data Fig. 3h–l). These data suggest the possibility of leveraging time and dosage windows to target RNA sequestration in AML.

Collectively, our results indicate P-body-associated translation repressors as crucial dependencies in human AML cells.

DDX6 is essential for leukaemia progression in vivo

We next asked whether DDX6 is essential to maintain AML in vivo. To address this question, we transplanted doxycycline-inducible CRISPRi HEL cells carrying either a non-targeting control sgRNA or a *DDX6*-targeting sgRNA into immunodeficient NSG mice (Fig. 2a). Doxycycline-induced *DDX6* silencing in the transplanted cells significantly prolonged the median survival of recipient mice (Fig. 2b). We obtained comparable results upon transplantation of control or *DDX6*-shRNA-transduced MOLM-13 cells (Fig. 2c,d). Consistent with extended lifespan, we initially observed strongly diminished numbers of *DDX6*-depleted MOLM-13 cells in the spleen and bone marrow of a separate cohort of recipient mice (Extended Data Fig. 3m). Of note, *DDX6* shRNA-transduced MOLM-13 cells remaining in moribund recipient mice several weeks later no longer exhibited *DDX6* knockdown (Extended Data Fig. 3n), indicating that they had escaped shRNA-mediated *DDX6* silencing. We next silenced *DDX6* in leukaemia cells isolated from two patients with AML with distinct cytogenetic abnormalities and transplanted them into NSG mice (Fig. 2e). Critically, *DDX6* knockdown AML cells were severely reduced in recipient mice, as shown by examination of spleen, bone marrow, peripheral blood and liver 60 days after transplantation (Fig. 2f,g). Thus, our data indicate that *DDX6* is crucial for human AML maintenance in vivo.

Next, we examined whether DDX6 plays an important role in leukaemia onset and progression in vivo. To this end, we generated *Ddx6* conditional knockout mice carrying two LoxP sites flanking exon 3 of the *Ddx6* locus (*Ddx6*$^{fl/fl}$) (Fig. 2h). Crossing these mice with *Mx1-Cre* mice enabled us to delete *Ddx6* in the haematopoietic compartment upon treatment with polyinosinic:polycytidylic acid (poly (I:C)). Western blot and genomic PCR confirmed poly (I:C)-induced *Ddx6* knockout in haematopoietic cells of *Mx1-Cre*/*Ddx6*$^{fl/fl}$ mice, while immunocytochemistry confirmed loss of P-bodies (Fig. 2i and Extended Data Fig. 3o–q). To induce leukemogenesis, we retrovirally transformed HSPCs from *Mx1-Cre* (*Ddx6*^{WT}) or *Mx1-Cre*/*Ddx6*$^{fl/fl}$ (*Ddx6*^{KO}) mice with the MLL-AF9 fusion oncogene, modelling human AML driven by mixed lineage leukemia (MLL) rearrangement, and transplanted them into wild-type (WT) recipient mice (Fig. 2j). We then ablated *Ddx6* by poly(I:C) administration in vivo 3 weeks after transplantation. Mice transplanted with MLL-AF9-transduced *Ddx6*^{WT} cells exhibited enlarged spleens and nearly complete takeover of the haematopoietic compartment by leukaemia cells 90 days post-transplant (Fig. 2k and Extended Data Fig. 4a–c). In contrast, MLL-AF9-transduced cells were virtually undetectable in recipient mice following *Ddx6* deletion (Fig. 2k and Extended Data Fig. 4c).

Similar results were obtained using a transplantation-based model of human AML driven by the (t8;21) chromosomal translocation, which gives rise to the *RUNX1::RUNX1T1* (AML1-ETO9a) fusion gene[28]. We crossed *Ddx6*$^{fl/fl}$ mice with *Rosa26-ERT2-Cre* mice to enable *Ddx6* ablation upon tamoxifen treatment. We expressed the AML1-ETO9a oncogene in HSPCs from *Rosa26-ERT2-Cre* or *Rosa26-ERT2-Cre*/*Ddx6*$^{fl/fl}$ mice and transplanted them into recipient animals

Fig. 3 | DDX6 plays a minor role during homoeostatic haematopoiesis but is important for regenerative haematopoiesis. a, Proliferation assay for shCTRL and shDDX6 human CD34$^+$ primary HSPCs at the indicated time points after transduction. Unpaired two-tailed Student's *t*-test, $n = 3$ biologically independent samples per group, mean ± s.d. **b**, Colony-forming assay of shCTRL and shDDX6 human bone marrow-derived CD34$^+$ cells. Colony-forming units were counted 13 d after seeding. Unpaired two-tailed Student's *t*-test, $n = 3$ biologically independent samples per group, mean ± s.e.m. **c**,**d**, Proliferation assay for shCTRL, shLSM14A (**c**) and shEIF4ENIF1 (**d**) human CD34$^+$ primary HSPCs at the indicated time points after transduction. Unpaired two-tailed Student's *t*-test, $n = 3$ biologically independent samples per group, mean ± s.d. **e**,**f**, Absolute numbers of nucleated cells in the spleen (**e**) and bone marrow (**f**) of *Mx1-Cre* and *Mx1-Cre/Ddx6*$^{fl/fl}$ mice 110 d after *Ddx6* deletion. Unpaired two-tailed Student's *t*-test, *Ddx6*^{WT} $n = 5$ mice, *Ddx6*^{KO} $n = 5$ mice, mean ± s.e.m. **g**, Representative flow cytometry plots showing percentages of Lin$^-$c-Kit$^+$Sca-1$^+$ (LSK) cells and Lin$^-$c-Kit$^+$Sca-1$^-$ (LK) cells in the bone marrow of *Mx1-Cre* and *Mx1-Cre/Ddx6*$^{fl/fl}$ mice 110 d after *Ddx6* deletion. **h**, Frequency of LSK cells in the bone marrow. Unpaired two-tailed Student's *t*-test, *Ddx6*^{WT} $n = 5$ mice, *Ddx6*^{KO} $n = 5$ mice, mean ± s.e.m. **i**, Representative flow cytometry plots showing percentages of HSC, MPP1, MPP2 and MPP4 populations, gated on LSK cells, in the bone marrow of *Mx1-Cre* and *Mx1-Cre/Ddx6*$^{fl/fl}$ mice 110 d after *Ddx6* deletion. **j**, Quantification of HSC, MPP1, MPP2 and MPP4 populations, as a percentage of LSK cells, in the bone marrow of *Mx1-Cre* and *Mx1-Cre/Ddx6*$^{fl/fl}$ mice 110 d after *Ddx6* deletion. Unpaired two-tailed Student's *t*-test, *Ddx6*^{WT} $n = 5$ mice, *Ddx6*^{KO} $n = 5$ mice, mean ± s.e.m. **k**, Quantification of B cells (CD19$^+$), T cells (CD3$^+$) and myeloid cells (CD11b$^+$) as a percentage of CD45$^+$ cells in the peripheral blood of *Mx1-Cre* and *Mx1-Cre/Ddx6*$^{fl/fl}$ mice at the indicated time points after *Ddx6* deletion. *Ddx6*^{WT} $n = 5$ mice, *Ddx6*^{KO} $n = 5$ mice, two-way ANOVA with Bonferroni's multiple comparisons test, mean ± s.d. **l**, *Ddx6*^{WT} and *Ddx6*^{KO} HSC, MPP1, MPP2 and MPP4 populations were sorted 24 d after *Ddx6* deletion and subjected to RNA-seq. PCA of all replicates of all populations is shown. **m**, GO analysis showing enrichment of indicated gene categories in genes upregulated in each *Ddx6*^{KO} population, relative to its *Ddx6*^{WT} counterpart. Two-tailed Fisher's exact test. **n**, Representative flow cytometry plots and quantification of percentages of Ki-67$^+$ cells in *Ddx6*^{WT} and *Ddx6*^{KO} HSCs, 24 d after *Ddx6* deletion. Unpaired two-tailed Student's *t*-test, $n = 3$ mice per group, mean ± s.e.m. **o**, MFI quantification of MitoTracker Green FM and TMRM staining in *Ddx6*^{WT} and *Ddx6*^{KO} HSCs, 24 d after *Ddx6* deletion. Unpaired two-tailed Student's *t*-test, $n = 3$ mice per group, mean ± s.e.m. **p**, Quantification of *Ddx6*^{WT} and *Ddx6*^{KO} chimerism within donor LSKs and LSK subpopulations in the bone marrow, 187 d after primary competitive transplantation. Unpaired two-tailed Student's *t*-test, $n = 5$ mice per group, mean ± s.e.m. **q**, Quantification of *Ddx6*^{WT} and *Ddx6*^{KO} chimerism within donor myeloid, T cell and B cell populations in the peripheral blood, at the indicated timepoints after primary competitive transplantation. Unpaired two-tailed Student's *t*-test, $n = 5$ mice per group, mean ± s.e.m. **r**, Quantification of *Ddx6*^{WT} and *Ddx6*^{KO} chimerism within the donor haematopoietic compartment (CD45$^+$) in peripheral blood, bone marrow and spleen, 63 d after secondary competitive transplantation. Unpaired two-tailed Student's *t*-test, $n = 5$ mice per group, mean ± s.e.m. TMRM, tetramethylrhodamine, methyl ester.

https://doi.org/10.1038/s41556-024-01489-6

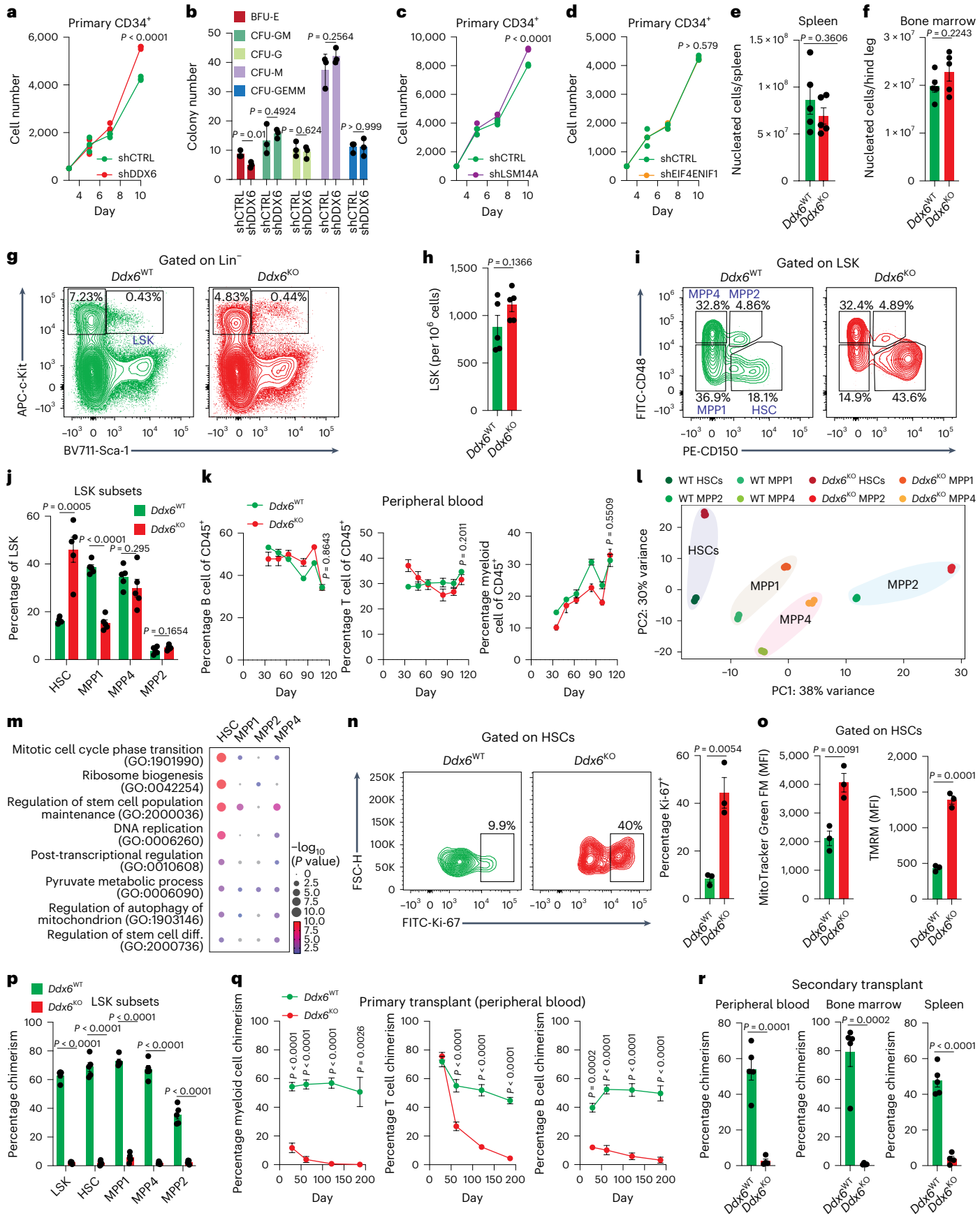

(Fig. 2l). Tamoxifen-induced *Ddx6* deletion in WT recipients ablated AML1-ETO9a-transformed cells in the haematopoietic compartment, consistent with our findings using the MLL-AF9 model (Fig. 2m). These data show that DDX6 is indispensable for leukemogenesis induced by different driver oncogenes.

In conclusion, these comprehensive in vivo experiments underscore the pivotal role of DDX6 in sustaining AML driven by distinct oncogenic mutations.

Loss of DDX6 does not derail homoeostatic haematopoiesis

While DDX6's broad role in embryonic development is well established[29], its function in adult tissue homoeostasis remains elusive. As our CRISPR screens suggested that DDX6 loss might have distinct effects in AML cells compared with their normal counterparts, we set out to determine its consequences on normal HSPCs. To this end, we induced *Rosa-Cre-ERT2*-mediated deletion of *Ddx6* in murine AML1-ETO9a leukaemia cells and normal c-Kit$^+$ progenitors. Notably, while *Ddx6* deletion markedly diminished colony formation by AML1-ETO9a leukaemia cells, it did not affect the colony-forming ability of their normal counterparts (Fig. 2n). Reinforcing these data, *DDX6* silencing did not impair survival, proliferation, or differentiation in primary human HSPCs or in an induced pluripotent stem (iPS) cell-derived human HSPC line[30] (Fig. 3a,b and Extended Data Fig. 4d–i). Congruently, silencing *LSM14A* or *EIF4ENIF1* also did not impair proliferation of primary human HSPCs (Fig. 3c,d and Extended Data Fig. 4j,k). These findings corroborate and extend the results of our CRISPR screens to human HSPCs.

Next, we examined the requirement for DDX6 in normal, homoeostatic haematopoiesis in vivo using our *Mx1-Cre/Ddx6*$^{fl/fl}$ mice. Four months after *Ddx6* deletion, we observed no significant changes in spleen and bone-marrow cellularity or overall frequency of HSPCs (Lin$^-$Sca-1$^+$c-Kit$^+$ (LSK)) (Fig. 3e–h). However, among LSK cells, *Ddx6* deletion resulted in a nearly threefold expansion of the haematopoietic stem cell (HSC) fraction (LSK CD150$^+$CD48$^-$), with concomitant reduction of the multipotent MPP1 population, whereas the lineage-biased MPP2 and MPP4 subsets remained unchanged (Fig. 3i,j). However, apart from a moderate decrease in the common myeloid progenitor (CMP) fraction, loss of *Ddx6* did not markedly impact the populations of committed progenitors or differentiated progeny (lymphoid, myeloid and erythroid cells) over a 4-month period (Fig. 3k and Extended Data Fig. 4l–p). Similar results were obtained using *Rosa26-Cre-ERT2* to globally delete *Ddx6* in adult mice, with HSC expansion but normal mature blood cell production and organismal survival over a 4-month period (Extended Data Fig. 4q–v).

Collectively, these data reveal that *Ddx6* deletion expands HSCs but has little downstream effect upon steady-state haematopoiesis.

DDX6 controls HSC function in regenerative haematopoiesis

To gain mechanistic insights into the role of DDX6 in LSK cells, we examined the transcriptomes of the HSC and MPP populations three weeks after inducing *Ddx6* deletion. Principal-component analysis (PCA) and unsupervised hierarchical clustering segregated each *Ddx6*$^{-/-}$ population from its WT counterpart, indicating widespread transcriptional changes in LSK cells upon loss of *Ddx6* (Fig. 3l and Extended Data Fig. 5a). Given the observed preferential expansion of HSCs in the absence of *Ddx6*, we focused on the transcriptional changes between *Ddx6*^{WT} and *Ddx6*^{KO} HSCs. Notably and in contrast to MPPs, upregulated transcripts in HSCs following *Ddx6* deletion were linked to cell cycle progression and increased metabolic activity, hallmarks of exit from quiescence and increased proliferation (Fig. 3m). Congruently, we observed a significant increase in dividing cells within the HSC fraction following *Ddx6* deletion (Fig. 3n). Moreover, *Ddx6*^{KO} HSCs harboured increased numbers of both total and active mitochondria, relative to *Ddx6*^{WT} controls (Fig. 3o and Extended Data Fig. 5b), corroborating our gene expression data. Together, these data led us to hypothesize that DDX6 regulates HSC function during stress haematopoiesis.

To test this hypothesis, we performed serial, competitive transplantation of *Ddx6*^{WT} or *Ddx6*^{KO} bone-marrow cells into lethally irradiated, congenic CD45.1 recipients. Loss of *Ddx6* profoundly impaired the ability of transplanted cells to engraft and contribute to donor-derived haematopoietic stem, progenitor and differentiated populations in recipient mice (Fig. 3p–r and Extended Data Fig. 5c), suggesting that DDX6 is crucial for HSC function upon stress. To exclude potential effects of *Ddx6* loss upon homing, we also performed competitive transplantation of sorted *Ddx6*^{WT} and *Ddx6*$^{fl/fl}$ HSCs, inducing *Ddx6* deletion 34 days later, after confirming successful engraftment by both populations (Extended Data Fig. 5d). Loss of *Ddx6* resulted in rapid and sustained loss of donor chimerism in the haematopoietic compartment, independent of homing (Extended Data Fig. 5d). These data highlight DDX6 as an important regulator of emergency HSC function.

Fig. 4 | P-bodies sequester translationally repressed mRNAs encoding key tumour suppressors. a, *DDX6* KD MOLM-13 cell numbers after rescue with DDX6 WT or DDX6 EQ. One-way ANOVA with Dunnett's post-hoc test, $n = 3$ biologically independent samples per group, mean ± s.e.m. **b**, Representative IF imaging of EDC4 punctae (green) and DDX6 punctae (red) in *DDX6* KD MOLM-13 cells after rescue with DDX6 WT or DDX6 EQ. Nuclei were counterstained with DAPI (blue). Scale: 5 µm. **c**, Quantification of EDC4$^+$DDX6$^+$ punctae in the indicated cells by IF. One-way ANOVA with Dunnett's post-hoc test, $n = 29–40$ cells per group, mean ± s.e.m. **d**, *LSM14A* KD HEL cell numbers after rescue with LSM14A WT, LSM14A ΔTFG or LSM14A ΔFFD. One-way ANOVA with Dunnett's post-hoc test, $n = 3$ biologically independent samples per groups, mean ± s.e.m. **e**, Quantification of EDC4$^+$DDX6$^+$ punctae in the indicated cells by IF. One-way ANOVA with Dunnett's post-hoc test, $n = 15–36$ cells per group, mean ± s.e.m. **f**, Representative IF imaging of EDC4 punctae (green) and DDX6 punctae (red) in *LSM14A* KD HEL cells after rescue with LSM14A WT, LSM14A ΔTFG or LSM14A ΔFFD. Nuclei were counterstained with DAPI (blue). Scale bar, 5 µm. **g**, MOLM-13 cell numbers 13 d after forced expression of NBDY. Unpaired two-tailed Student's *t*-test, $n = 3$ biologically independent samples per group, mean ± s.e.m. **h**, Representative IF imaging of EDC4 punctae (red) and FLAG (green) in control and *NBDY*-expressing MOLM-13 cells. Nuclei were counterstained with DAPI (blue). Scale bar, 5 µm. **i**, Quantification of EDC4$^+$ punctae in the indicated cells by IF. Unpaired two-tailed Student's *t*-test, $n = 59-129$ cells per group, mean ± s.e.m. **j**, Schematic for the purification and transcriptomic profiling of P-bodies from MOLM-13 cells based on the expression of GFP-LSM14A$^+$. **k**, Representative flow cytometry plots showing gating for GFP-LSM14A$^+$ P-bodies in MOLM-13 cells. **l**, Heatmap showing expression levels of differentially enriched mRNAs between purified P-body and cytoplasmic fractions in MOLM-13 cells ($n = 2$ biologically independent samples per group), FC > 1.5, $P < 0.05$, Wald test with Benjamini–Hochberg correction. Highlighted in green, putative tumour suppressors, transcription factors and chromatin factors. **m**, GSEA plot showing enrichment of a tumour-suppressor gene signature[75] in P-bodies versus cytoplasmic fractions of MOLM-13 cells. Normalized enrichment score (NES) = 1.26, $P = 0.0038$. **n**, Gene tracks of RNA-seq data showing individual mRNAs enriched in P-bodies or cytoplasm of MOLM-13 cells. **o**, Representative smFISH images of *KDM5B* mRNA molecules (red) and GFP-LSM14A$^+$ punctae (green). Nuclei were counterstained with DAPI (blue). Scale bar, 5 µm. **p**, Quantification of the fraction of *KDM5B* mRNA transcripts colocalizing with GFP-LSM14A$^+$ punctae in individual cells ($n = 33$, mean 48.98%). **q**, Ribosome density negatively correlates with mRNA enrichment in P-bodies in MOLM-13 cells. Polysome profiling data from GSE202227 (ref. 76). **r**, Translation rate fold changes following P-body dissolution (shDDX6) positively correlated with mRNA enrichment in P-bodies. **s**, Balloon plot showing TargetScan miRNA enrichment analysis for miRNA binding within P-body enriched mRNAs that change translation level (left). Heatmap showing expression levels of miRNAs (small RNA-seq) identified by TargetScan in control versus *DDX6* KD MOLM-13 cells ($n = 2$ biologically independent samples per group) (right). **t**, Heatmap of protein expression for tumour suppressors in CTRL and *DDX6* KD MOLM-13 cells that increase in both translation and protein levels upon *DDX6* silencing ($n = 3$). **u**, Cell numbers 6 d after lentivirus-mediated overexpression of the indicated genes in MOLM-13 cells. Unpaired two-tailed Student's *t*-test, $n = 3$ biologically independent samples per group, mean ± s.e.m.

https://doi.org/10.1038/s41556-024-01489-6

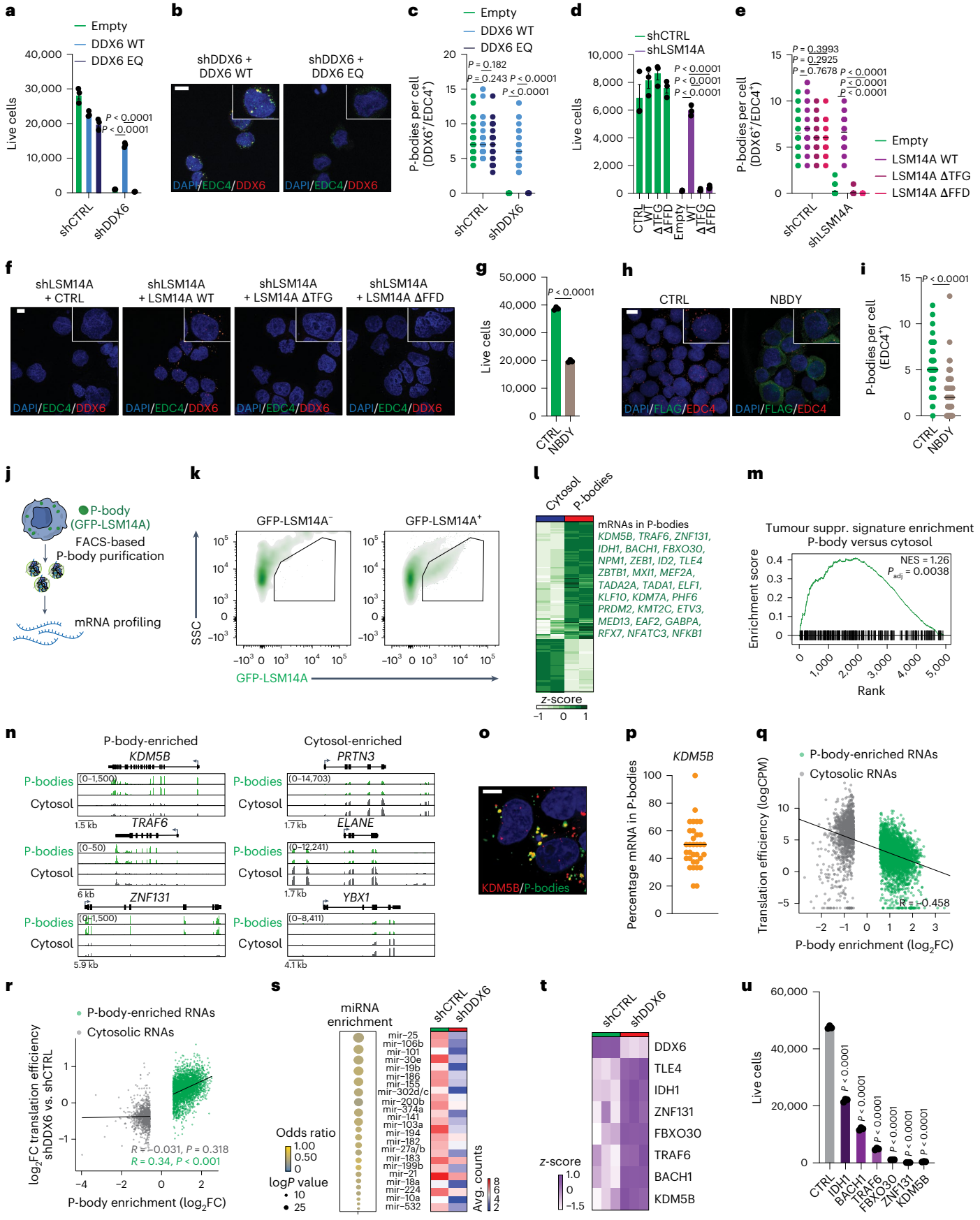

Collectively, our data show that DDX6-mediated RNA sequestration is not essential for homoeostatic haematopoiesis, but protects HSPCs undergoing severe stress, such as regeneration and leukaemic transformation.

AML cell survival is coupled to P-body assembly

Given the critical role of DDX6 in leukaemia, we next investigated the molecular mechanisms by which loss of DDX6 abrogates AML cell survival. Considering that the depletion of the other proteins essential for P-body assembly, EIF4ENIF1 and LSM14A, also diminishes AML cell survival, we asked whether the loss of P-bodies could underlie this phenotype. To explore this, we examined if treatment with differentiation-inducing compounds[31,32] could trigger the dissolution of P-bodies. Treatment of HEL cells with phorbol 12-myristate 13-acetate (PMA) resulted in differentiation[32] and P-body loss (Extended Data Fig. 5e– i). Similarly, treatment of MOLM-13 cells with the clinical-stage DOT1L inhibitor EPZ-5676 (ref. 33) induced differentiation and P-body dissolution (Extended Data Fig. 5j,k). These findings suggest that P-body loss might be a shared characteristic of multiple distinct anti-leukaemic pathways.

Subsequently, we investigated whether the ability of DDX6 and LSM14A to mediate P-body assembly is required to sustain AML cells. Initially, we expressed shRNA-resistant forms of either WT DDX6 or a catalytically inactive point mutant (DDX6 E247Q)[8,34] in DDX6 knockdown MOLM-13 cells (Extended Data Fig. 5l). *DDX6*-depleted cells expressing DDX6 WT maintained proliferation and P-bodies, similar to control cells, while the expression of the DDX6 E247Q mutant failed to restore P-bodies and rescue the proliferation defect (Fig. 4a–c and Extended Data Fig. 5m–q).

We then assessed whether disrupting LSM14A's capacity to mediate P-body formation would yield similar results. To this end, we utilized two LSM14A mutants, ΔTFG and ΔFFD, both incapable of mediating P-body formation due to defective interaction with DDX6 or EDC4, respectively[35,36]. We expressed shRNA-resistant forms of either WT LSM14A (LSM14A WT), LSM14A ΔTFG, or LSM14A ΔFFD in *LSM14A*-depleted HEL cells (Extended Data Fig. 6a). Similar to our observations with helicase-deficient DDX6, the LSM14A mutants failed to rescue the P-body formation and proliferation defect of LSM14A-knockdown HEL cells (Fig. 4d–f and Extended Data Fig. 6b–e). These data suggest a connection between the roles of DDX6 and LSM14A in P-body assembly and AML cell proliferation.

We further probed the requirement for P-bodies in leukaemia cells by modulating P-body numbers using the human microprotein NBDY, which localizes to and destabilizes P-bodies through its interaction with EDC4 (refs. 36–39). Overexpression of NBDY in MOLM-13 and HEL cells decreased P-bodies by nearly twofold, accompanied by a proportional decrease in cell numbers (Fig. 4g–i and Extended Data Fig. 6f–h). These data suggest that proliferation and viability of leukaemia cells is correlated with the numbers of P-bodies.

Taken together, these results, using multiple orthogonal approaches to modulate P-body homoeostasis in different AML cell lines, strengthen our conclusion that AML cells rely upon post-transcriptional mechanisms associated with P-body assembly for their survival.

P-bodies sequester untranslated mRNAs encoding tumour suppressors

We next sought to examine the identity and fate of the mRNAs sequestered in P-bodies of AML cells. To this end, we adapted a method for the isolation of intact P-bodies[9] (Fig. 4j). In brief, P-bodies are fluorescently labelled in cells engineered to express a green fluorescent protein (GFP)-tagged form of the P-body marker LSM14A[9]. We initially validated this system in MOLM-13 cells, showing that *DDX6* silencing in LSM14A-GFP-transduced cells abolished GFP$^+$ particles, consistent with P-body dissolution and confirming that this method labels bona fide P-bodies (Extended Data Fig. 6i). Subsequently, we isolated LSM14A-GFP$^+$ P-bodies from MOLM-13 and HEL cellular lysates by fluorescence-activated particle sorting and performed RNA-seq, using total cytoplasmic fractions as a control (Fig. 4k). We detected similar numbers of transcripts (~12,000) between P-bodies and cytoplasm in both MOLM-13 and HEL cells, with the majority corresponding to protein-coding RNAs (Extended Data Fig. 6j). Of the cytoplasmic transcripts, 3,390 were enriched in P-bodies of MOLM-13 cells and 2,972 were enriched in P-bodies of HEL cells (fold change (FC) > 1.5, $P < 0.05$) (Fig. 4l). The distribution of P-body-targeted RNAs was comparable across expression level quartiles, indicating that their enrichment in P-bodies is independent of their overall expression (Extended Data Fig. 6k).

Next, we examined the identity of the mRNAs targeted to P-bodies in AML cells. Notably, gene set enrichment analysis (GSEA) revealed enrichment for a tumour-suppressor gene signature among P-body-targeted mRNAs (Fig. 4m). For example, P-bodies sequestered transcripts encoding the tumour suppressors *KDM5B* and *TRAF6* (refs. 40–42), whereas transcripts encoding genes important for leukaemia cell function (for example *PRNT3*, *ELANE* and *YBX1*)[43–45] were enriched in the cytoplasm (Fig. 4n). These data led us to hypothesize that AML cells might sequester tumour-suppressive mRNAs in P-bodies to regulate their post-transcriptional fate. We corroborated our P-body-seq using single-molecule fluorescence in situ hybridization (smFISH) for the P-body-enriched transcripts *KDM5B*, *POLK* and *RSRC2*, showing that P-bodies harbour substantial fractions (~50–70%) of P-body-enriched mRNAs, consistent with recent data in *C. elegans*[13] (Fig. 4o,p and Extended Data Fig. 6l–n). Of note, compared with RNAs enriched in the cytoplasm, P-body-enriched RNAs exhibited a stronger overlap between MOLM-13 and HEL cells (Extended Data Fig. 7a,b), highlighting RNA condensation as a mechanism for depleting the cytoplasm of specific mRNAs across AML subtypes. Collectively, these data indicate that a substantial fraction of cytoplasmic RNAs localize to P-bodies in AML cells.

To corroborate the involvement of DDX6 in targeting mRNAs to P-bodies, we performed enhanced UV crosslinking and immunoprecipitation sequencing (eCLIP-seq)[46] to identify direct DDX6 targets in MOLM-13 cells. Analysis of DDX6 binding patterns revealed a preferential association with exons over introns, consistent with previous reports[8,47] and a significant correlation among biological replicates (Extended Data Fig. 7c,d). As expected, intersection of P-body-targeted and DDX6-targeted mRNAs revealed a large overlap (54%), with enrichment for biological processes related to transcription, chromatin regulation, cell cycle and cell death (Extended Data Fig. 7e,f).

Last, we sought to investigate the fate of mRNAs sequestered in P-bodies of AML cells. Loss of RNA sequestration did not alter the levels of P-body-associated mRNAs (Extended Data Fig. 7g,h), leading us to hypothesize that they might be preferentially subjected to translational repression rather than degradation. Indeed, analysis of polysome profiling in MOLM-13 cells revealed that enrichment in P-bodies strongly correlated with reduced ribosomal association (Fig. 4q), indicative of translational repression. Congruently, transcripts targeted to P-bodies in MOLM-13 cells exhibited features associated with inefficient translation, including increased length and adenylate/uridylate (AU) content[6,8] (Extended Data Fig. 7i).

Taken together, our data suggest that AML cells sequester translationally repressed mRNAs encoding tumour-suppressive chromatin and transcription factors in P-bodies. These findings raise the possibility that P-body dissolution might translationally de-repress P-body-targeted tumour-suppressive mRNAs in AML cells.

Loss of RNA sequestration de-represses tumour-suppressor mRNAs

To investigate how loss of RNA sequestration impacts the fate of P-body-associated mRNAs, we conducted polysome profiling of AML

https://doi.org/10.1038/s41556-024-01489-6

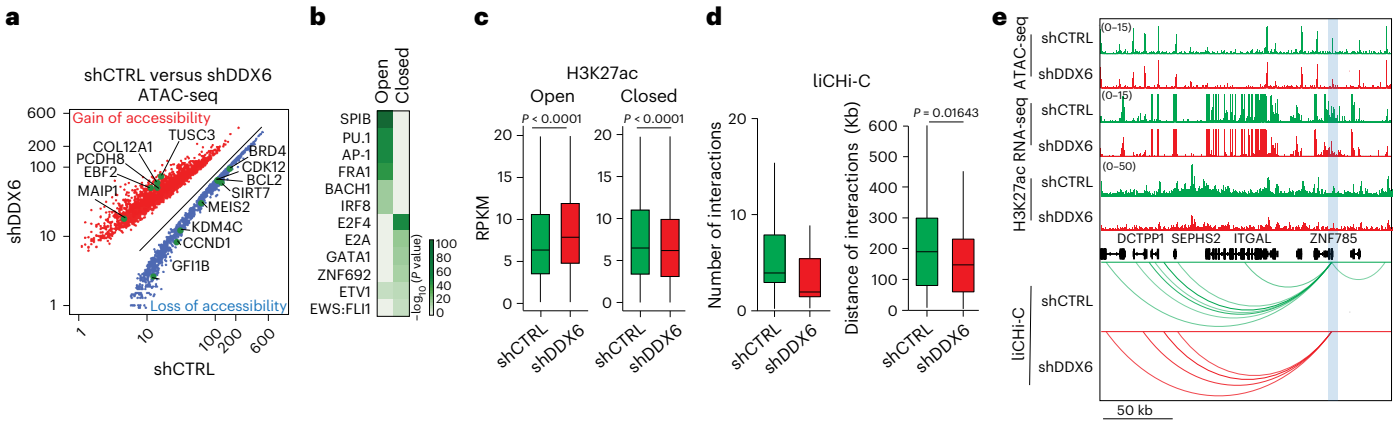

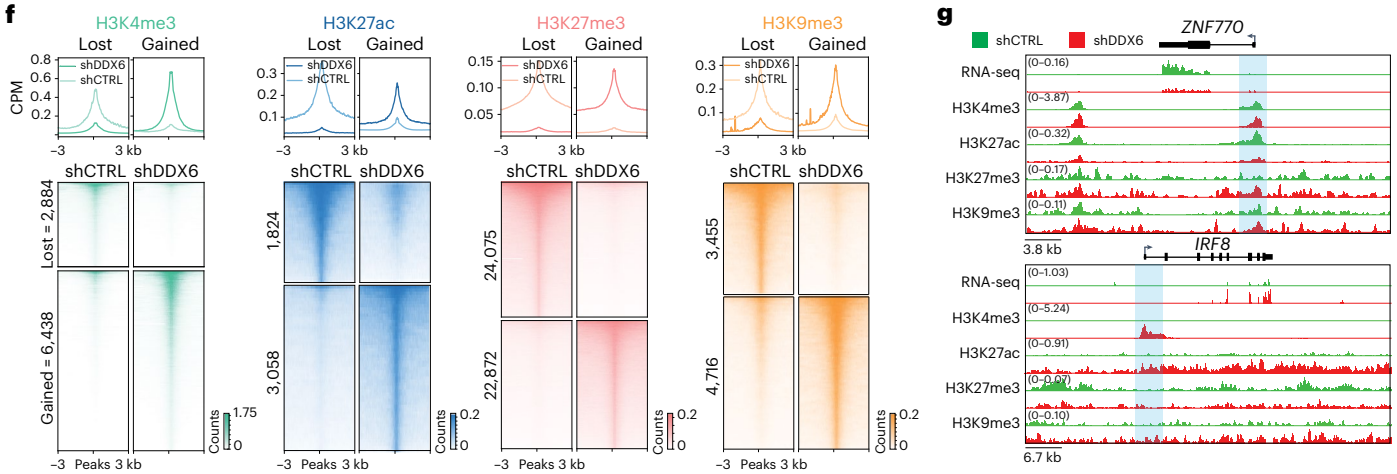

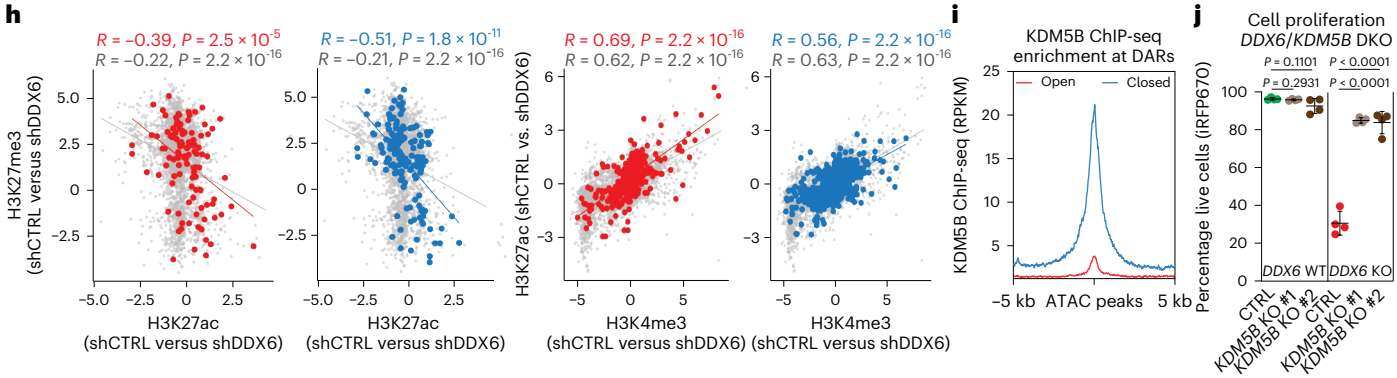

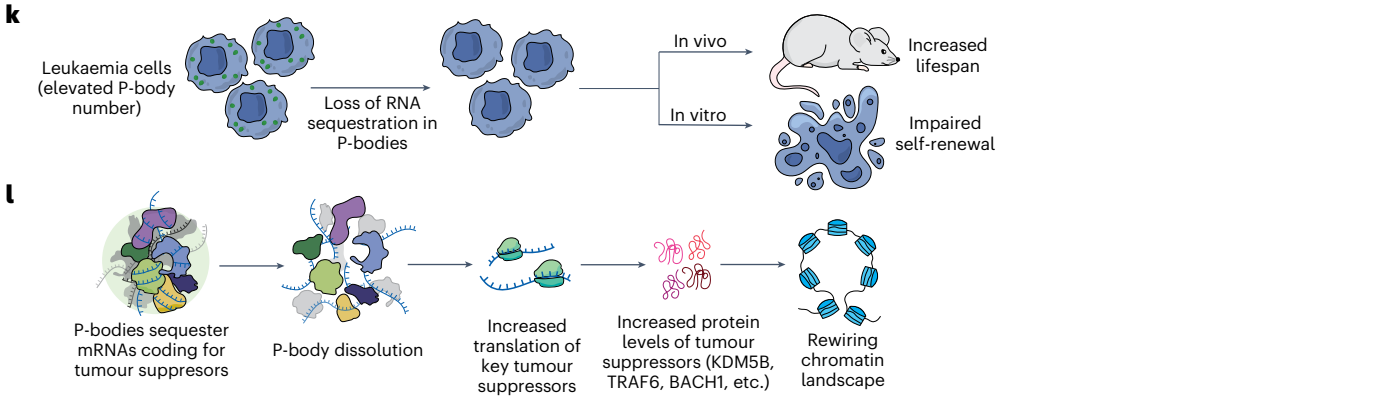

cells following *DDX6* silencing. In line with our hypothesis, the translation rate of P-body-associated mRNAs significantly increased after *DDX6* suppression compared with total cytoplasmic RNAs ($P = 22 \times 10^{-16}$) (Fig. 4r and Extended Data Fig. 7j). Given the known involvement of DDX6 and P-bodies in miRNA-mediated translational suppression[48–50], we explored the potential contribution of miRNAs to the translational repression of sequestered mRNAs. To this end, we performed small RNA-seq, detecting expression changes in miRNAs as well as other

Fig. 5 | Loss of DDX6 impacts the chromatin architecture of AML cells. **a**, Scatter-plot showing ATAC-seq analysis of chromatin accessibility for shCTRL ($n = 2$) and shDDX6 ($n = 2$) MOLM-13 cells. Blue dots indicate genomic regions showing significantly decreased chromatin accessibility in *DDX6*-depleted cells (FC > 1.5, $P < 0.05$, $n = 1{,}222$); red dots indicate genomic regions showing significantly increased chromatin accessibility in *DDX6*-depleted cells (FC > 1.5, $P < 0.05$, $n = 2{,}345$). **b**, TF motif enrichment on shDDX6 gained and lost ATAC-seq peaks. **c**, Boxplots showing H3K27ac levels (RPKM) at loci of genes that gained or lost chromatin accessibility after *DDX6* KD. Wilcoxon rank-sum test, shCTRL open ($n = 1{,}974$), shDDX6 open ($n = 2{,}039$), shCTRL closed ($n = 1{,}041$) and shDDX6 closed ($n = 1{,}075$). Box centre line indicates median, box limits indicate upper (Q3) and lower quartiles (Q1), lower whisker indicates Q1 − 1.5 × interquartile range (IQR) and upper whisker indicates Q3 + 1.5 × IQR. **d**, Low-input promoter capture Hi-C (liCHi-C) results showing loss of looping interactions (left) and average distance of interactions at promoters of genes (right) with significantly decreased chromatin accessibility and expression following *DDX6* knockdown. Unpaired two-tailed Student's *t*-test, $n = 28$ per group. Box centre line indicates median, box limits indicate upper (Q3) and lower quartiles (Q1), lower whisker indicates Q1 − 1.5 × IQR and upper whisker indicates Q3 + 1.5 × IQR. **e**, Gene tracks of ATAC-seq, RNA-seq, H3K27ac CUT&RUN and liCHi-C data for the genomic region surrounding *ZNF785*. Blue shadow highlights the gene promoter. Arcs represent significant promoter interactions (CHiCAGO score > 5). **f**, Genomic heatmaps (CUT&Tag) showing gain and loss of peaks for the indicated histone modifications in control versus *DDX6* KD HL-60 cells (bottom). Average plot showing CUT&Tag signal at the genomic heatmaps (bottom) in control versus *DDX6* KD HL-60 cells (top). **g**, Gene tracks of RNA-seq and CUT&Tag data for the indicated histone modifications for the genomic regions surrounding (top) *ZNF770* and (bottom) *IRF8*. Blue shadow highlights the gene promoter. **h**, Scatter-plots showing correlations in histone marks dynamics for all regions (grey dots and lines), regions associated with upregulated genes (red dots and lines) or regions associated with downregulated genes (blue dots and lines) in *DDX6* KD MOLM-13 cells. Correlation coefficients and the corresponding *P* values are shown. **i**, Average plot showing KDM5B enrichment at differentially accessible regions (DARs) as defined by ATAC-seq in **a**. KDM5B ChIP-seq data were taken from GSM1003586 (ref. 22). **j**, Competition-based proliferation assays upon *DDX6* and *KDM5B* double knockout in AML cells. Unpaired two-tailed Student's *t*-test, $n = 3$ biologically independent samples per group, mean ± s.e.m. **k**, Model summarizing the phenotypic consequences of losing P-body-targeted RNA sequestration in AML cells. **l**, A mechanistic model proposing how the interplay between RNA sequestration in P-bodies and chromatin architecture impacts AML. DKO, double knockout.

small noncoding RNAs (for example, tRNA and rRNA-derived small RNAs (tsRNAs and rsRNAs)) following *DDX6* silencing in MOLM-13 cells (Extended Data Fig. 7k,l). Of note, we found that P-body-targeted mRNAs that underwent increased translation in *DDX6* knockdown AML cells were enriched for binding sites of miRNAs that became downregulated upon *DDX6* silencing (Fig. 4s). Among the target mRNAs translationally upregulated upon P-body dissolution, we observed tumour suppressors with known anti-leukaemic function (for example, *IDH1*, *TRAF6* and *KDM5B*[40,42,51,52]), as well as those with unknown roles in leukaemia (for example, *FBXO30*, *ZNF131* and *BACH1*), paralleling our P-body sequencing data. We next asked whether these tumour suppressors also became upregulated at the protein level following *DDX6* depletion. To this end, we performed proteomics in MOLM-13 cells, first establishing the quality of these data by confirming the expected downregulation of P-body components upon loss of DDX6 (ref. 8) (Extended Data Fig. 8a–e). Further analyses revealed increased protein levels of P-body-targeted tumour suppressors in *DDX6*-depleted AML cells (Fig. 4t). We therefore hypothesized that an important function of RNA sequestration in AML is to sustain translational repression of tumour-suppressor genes. Congruently, forced expression of *IDH1*, *FBXO30*, *BACH1*, *ZNF131*, *TRAF6* and *KDM5B* significantly impaired the proliferation of MOLM-13 cells (Fig. 4u and Extended Data Fig. 8f,g).

Together, these data indicate that loss of RNA sequestration in AML cells promotes the translation of mRNAs encoding potent tumour suppressors.

RNA sequestration maintains leukaemic chromatin architecture

Our discovery that AML cells sequester untranslated mRNAs encoding tumour-suppressive chromatin regulators (for example, *KDM5B*, *IDH1*, *KMT2C* and *KDM7A*) suggests a potentially critical, albeit indirect, connection between P-body function and the aberrant chromatin state characteristic of AML cells. To explore this hypothesis, we performed an assay for transposase-accessible chromatin with sequencing (ATAC-seq) to assess changes in chromatin accessibility after *DDX6* knockdown in MOLM-13 and HEL cells (Extended Data Fig. 8h,i). We observed an overall increase in accessible chromatin regions in *DDX6*-silenced AML cells relative to controls (Fig. 5a and Extended Data Fig. 8j). Of note, we observed multiple putative tumour-suppressor genes among the regions that gained accessibility upon *DDX6* depletion (for example, *PCDH8*, *TUSC3*, *GATA2*, *PRDM11* and *ARID1B*[53–57]) (Fig. 5a and Extended Data Fig. 8j). Conversely, multiple pro-leukaemic genes were among the sites that lost accessibility upon *DDX6* depletion (for example, *BCL2*, *SIRT7*, *MEIS2*, *BRD4* and *IKZF2* (refs. 58–62); Fig. 5a and Extended Data Fig. 8j). Moreover, TF motif analysis revealed enrichment for potential tumour-suppressive TFs such as SPIB, PU.1, AP-1, BACH1 and IRF8 (refs. 63–67) in regions that gained accessibility upon *DDX6* knockdown (Fig. 5b and Extended Data Fig. 8k).

To gain further insights, we measured the active chromatin marks H3K27ac and H3K4me1 by cleavage under targets & release using nuclease (CUT&RUN) and analysed changes in the three-dimensional (3D) genome structure by low-input promoter capture Hi-C (liCHi-C) in control and DDX6-depleted MOLM-13 cells. Our findings revealed concomitant changes in both histone marks at regions undergoing changes in chromatin accessibility (Fig. 5c and Extended Data Fig. 8l). Additionally, at loci of genes that became less accessible and downregulated after DDX6 depletion, we observed decreased frequency and distance of promoter interactions, consistent with reduced transcriptional output (Fig. 5d and Extended Data Fig. 8m). Thus, DDX6 depletion in AML cells rewires chromatin organization, as illustrated at the *ZNF785* and *AGO4* loci (Fig. 5e and Extended Data Fig. 8n).

To investigate whether our observations extend to another AML subtype, we assessed the genome-wide distribution of histone marks commonly associated with transcriptional activation (that is, H3K4me3 and H3K27ac) and repression (H3K27me3 and H3K9me3) using cleavage under targets and tagmentation (CUT&Tag). Similar to MOLM-13 cells, HL-60 cells exhibited widespread changes in histone mark deposition following *DDX6* knockdown, compared with controls (Fig. 5f). By analysing the dynamics of the aforementioned histone marks profiled, we observed changes in H3K27ac and H3K4me3 to be positively correlated and changes in H3K27ac and H3K27me3 to be negatively correlated (Fig. 5g,h and Extended Data Fig. 8n). Notably, we also noticed significant correlations at regulatory regions of genes that are differentially expressed upon *DDX6* knockdown, indicating that these modules of epigenome reshaping might be operating to regulate gene expression (Fig. 5h).

These findings provide a direct perspective on the epigenetic changes underlying the transcriptional programme switching taking place after P-body dissolution. While chromatin remodelling is expected during differentiation, the sequestration of chromatin regulator mRNAs and their increased translation upon P-body dissolution led us to examine a direct contribution of implicated candidates to the observed epigenetic rewiring.

Among DDX6-bound P-body-targeted genes in AML cells, the H3K4 demethylase *KDM5B*[68] emerged as a potential candidate, due to its increased translation rate and protein expression following

DDX6 depletion as well as its potent suppression of MOLM-13 cell survival (Fig. 4r,t,u). Indeed, analysis of ChIP-seq data in leukaemia cells[22] revealed enrichment of KDM5B at regions that lost accessibility in *DDX6*-depleted MOLM-13 cells (Fig. 5i). To assess the role of KDM5B in our observed phenotype, we knocked it out in both *DDX6* WT and *DDX6* knockout MOLM-13 cells. Notably, while knockout of *KDM5B* in the WT background did not affect cell proliferation, double knockout of *DDX6* and *KDM5B* abrogated the effect of P-body dissolution and restored proliferation to levels close to WT cells. Mechanistically, these data place KDM5B directly downstream of P-body dissolution, providing a molecular link to the resultant chromatin remodelling (Fig. 5j and Extended Data Fig. 8o).

In summary, our findings unveil an indirect crosstalk between cytoplasmic RNA processing and genome architecture, highlighting the intricate role of DDX6 in AML pathogenesis.

Discussion

Corrupted translation control sustains cancer cells, though the underlying mechanisms remain unclear. Here, our results indicate a crucial coupling between dysregulated translation and RNA sequestration in P-bodies in AML. We find that disrupting RNA sequestration in P-bodies abrogated leukaemia cell survival and disease progression in vivo (Fig. 5k). We further show that P-bodies in AML cells harbour translationally repressed mRNAs encoding critical tumour suppressors with roles in epigenetic and transcriptional regulation. Loss of RNA sequestration led to increased translation rates and protein levels of these tumour suppressors and dismantling of leukaemic transcriptional and chromatin architecture (Fig. 5l).

In contrast to AML, loss of RNA sequestration did not derail steady-state haematopoiesis, instead promoting HSC cycling and mitochondrial activity. HSCs are particularly sensitive to perturbations in translation and mitochondrial metabolism, which can impair their long-term capacity to tolerate stress and self-renew[69–73]. Indeed, we observed that RNA sequestration was crucial to preserve HSC regenerative capacity. HSCs rely upon conserved pathways to resist the profound stresses associated with both. We speculate that RNA sequestration is crucial to safeguard HSC longevity and function during emergency conditions, such as regenerative and malignant haematopoiesis.

A key question that remains is how AML cells select transcripts for sequestration in P-bodies. Our data hint at P-body-enriched mRNAs being longer and more AU-rich on average than their cytosolic counterparts, in line with previous work[6]. AU-rich mRNAs are inefficiently translated[6] and as mRNA translation and sequestration are competing processes, we speculate that increasing the RNA sequestration machinery tilts the balance in favour of translational repression of these transcripts. If oncogenic mRNAs are more favourably translated than tumour-suppressor mRNAs, they may preferentially escape sequestration. P-bodies have also been studied as possible sites for miRNA-mediated translational repression[74]. Accordingly, we discovered that mRNAs that experienced increased translation in *DDX6*-depleted AML cells were enriched for binding sites of miRNAs that become downregulated upon *DDX6* silencing. Thus, differential miRNA expression adds another layer of selectivity to mRNA translation control and storage in P-bodies. Indeed, this principle could be hijacked in other tissues as well, as P-body-associated genes are dysregulated in various cancer types[15–18].

In summary, we have uncovered a previously unrecognized link between dysregulated translation control and P-body formation in myeloid leukaemia. These findings deepen our understanding of the interplay between post-transcriptional regulation and oncogenesis and point to innovative avenues for reprogramming RNA processing in cancer treatment.

Online content

Any methods, additional references, Nature Portfolio reporting summaries, source data, extended data, supplementary information, acknowledgements, peer review information; details of author contributions and competing interests; and statements of data and code availability are available at https://doi.org/10.1038/s41556-024-01489-6.

References

1. van Galen, P. et al. Single-cell RNA-seq reveals AML hierarchies relevant to disease progression and immunity. *Cell* **176**, 1265–1281 e1224 (2019).
2. Fabbri, L., Chakraborty, A., Robert, C. & Vagner, S. The plasticity of mRNA translation during cancer progression and therapy resistance. *Nat. Rev. Cancer* **21**, 558–577 (2021).
3. Buxbaum, A. R., Haimovich, G. & Singer, R. H. In the right place at the right time: visualizing and understanding mRNA localization. *Nat. Rev. Mol. Cell Biol.* **16**, 95–109 (2015).
4. Roden, C. & Gladfelter, A. S. RNA contributions to the form and function of biomolecular condensates. *Nat. Rev. Mol. Cell Biol.* **22**, 183–195 (2021).
5. Sheth, U. & Parker, R. Decapping and decay of messenger RNA occur in cytoplasmic processing bodies. *Science* **300**, 805–808 (2003).
6. Courel, M. et al. GC content shapes mRNA storage and decay in human cells. *eLife* **8**, e49708 (2019).
7. Brengues, M., Teixeira, D. & Parker, R. Movement of eukaryotic mRNAs between polysomes and cytoplasmic processing bodies. *Science* **310**, 486–489 (2005).
8. Di Stefano, B. et al. The RNA helicase DDX6 controls cellular plasticity by modulating P-body homeostasis. *Cell Stem Cell* **25**, 622–638 e613 (2019).
9. Hubstenberger, A. et al. P-body purification reveals the condensation of repressed mRNA regulons. *Mol. Cell* **68**, 144–157 e145 (2017).
10. Teixeira, D., Sheth, U., Valencia-Sanchez, M. A., Brengues, M. & Parker, R. Processing bodies require RNA for assembly and contain nontranslating mRNAs. *RNA* **11**, 371–382 (2005).
11. Ayache, J. et al. P-body assembly requires DDX6 repression complexes rather than decay or Ataxin2/2L complexes. *Mol. Biol. Cell* **26**, 2579–2595 (2015).
12. Wilbertz, J. H. et al. Single-molecule imaging of mRNA localization and regulation during the integrated stress response. *Mol. Cell* **73**, 946–958 e947 (2019).
13. Cardona, A. H. et al. Self-demixing of mRNA copies buffers mRNA:mRNA and mRNA:regulator stoichiometries. *Cell* **186**, 4310–4324 e4323 (2023).
14. Hallacli, E. et al. The Parkinson's disease protein alpha-synuclein is a modulator of processing bodies and mRNA stability. *Cell* **185**, 2035–2056 e2033 (2022).
15. Lavalee, M., Curdy, N., Laurent, C., Fournie, J. J. & Franchini, D. M. Cancer cell adaptability: turning ribonucleoprotein granules into targets. *Trends Cancer* **7**, 902–915 (2021).
16. Nsengimana, B. et al. Processing body (P-body) and its mediators in cancer. *Mol. Cell. Biochem.* **477**, 1217–1238 (2022).
17. Ghashghaei, M. et al. miR-148a-3p and DDX6 functional link promotes survival of myeloid leukemia cells. *Blood Adv.* **7**, 3846–3861 (2023).
18. Hernandez, G. et al. Decapping protein EDC4 regulates DNA repair and phenocopies BRCA1. *Nat. Commun.* **9**, 967 (2018).
19. Heyes, E. et al. Identification of gene targets of mutant C/EBPα reveals a critical role for MSI2 in CEBPA-mutated AML. *Leukemia* **35**, 2526–2538 (2021).
20. Brandstoetter, T. et al. SBNO2 is a critical mediator of STAT3-driven hematological malignancies. *Blood* https://doi.org/10.1182/blood.2022018494 (2023).
21. Luo, Y., Na, Z. & Slavoff, S. A. P-bodies: composition, properties, and functions. *Biochemistry* **57**, 2424–2431 (2018).
22. Consortium, E. P. An integrated encyclopedia of DNA elements in the human genome. *Nature* **489**, 57–74 (2012).

23. Rasch, F., Weber, R., Izaurralde, E. & Igreja, C. 4E-T-bound mRNAs are stored in a silenced and deadenylated form. *Genes Dev.* **34**, 847–860 (2020).
24. Kamenska, A. et al. The DDX6-4E-T interaction mediates translational repression and P-body assembly. *Nucleic Acids Res.* **44**, 6318–6334 (2016).
25. Zong, H. et al. A hyperactive signalosome in acute myeloid leukemia drives addiction to a tumor-specific Hsp90 species. *Cell Rep.* **13**, 2159–2173 (2015).
26. Nakagawa, T. et al. Establishment of a leukaemic cell line from a patient with acquisition of chromosomal abnormalities during disease progression in myelodysplastic syndrome. *Br. J. Haematol.* **85**, 469–476 (1993).
27. Erb, M. A. et al. Transcription control by the ENL YEATS domain in acute leukaemia. *Nature* **543**, 270–274 (2017).
28. Yan, M. et al. A previously unidentified alternatively spliced isoform of t(8;21) transcript promotes leukemogenesis. *Nat. Med.* **12**, 945–949 (2006).
29. Kim, J. et al. The RNA helicase DDX6 controls early mouse embryogenesis by repressing aberrant inhibition of BMP signaling through miRNA-mediated gene silencing. *PLoS Genet.* **18**, e1009967 (2022).
30. Doulatov, S. et al. Induction of multipotential hematopoietic progenitors from human pluripotent stem cells via respecification of lineage-restricted precursors. *Cell Stem Cell* **13**, 459–470 (2013).
31. Brzezinka, K. et al. Functional diversity of inhibitors tackling the differentiation blockage of MLL-rearranged leukemia. *J. Hematol. Oncol.* **12**, 66 (2019).
32. Hong, Y., Martin, J. F., Vainchenker, W. & Erusalimsky, J. D. Inhibition of protein kinase C suppresses megakaryocytic differentiation and stimulates erythroid differentiation in HEL cells. *Blood* **87**, 123–131 (1996).
33. Stein, E. M. et al. The DOT1L inhibitor pinometostat reduces H3K79 methylation and has modest clinical activity in adult acute leukemia. *Blood* **131**, 2661–2669 (2018).
34. Jangra, R. K., Yi, M. & Lemon, S. M. DDX6 (Rck/p54) is required for efficient hepatitis C virus replication but not for internal ribosome entry site-directed translation. *J. Virol.* **84**, 6810–6824 (2010).
35. Brandmann, T. et al. Molecular architecture of LSM14 interactions involved in the assembly of mRNA silencing complexes. *EMBO J.* **37**, e97869 (2018).
36. Brothers, W. R., Fakim, H., Kajjo, S. & Fabian, M. R. P-bodies directly regulate MARF1-mediated mRNA decay in human cells. *Nucleic Acids Res.* **50**, 7623–7636 (2022).
37. Na, Z. et al. The NBDY microprotein regulates cellular RNA decapping. *Biochemistry* **59**, 4131–4142 (2020).
38. Na, Z. et al. Phosphorylation of a human microprotein promotes dissociation of biomolecular condensates. *J. Am. Chem. Soc.* **143**, 12675–12687 (2021).
39. D'Lima, N. G. et al. A human microprotein that interacts with the mRNA decapping complex. *Nat. Chem. Biol.* **13**, 174–180 (2017).
40. Ren, Z. et al. A PRC2-Kdm5b axis sustains tumorigenicity of acute myeloid leukemia. *PNAS* **119**, e2122940119 (2022).
41. Wong, S. H. et al. The H3K4-methyl epigenome regulates leukemia stem cell oncogenic potential. *Cancer Cell* **28**, 198–209 (2015).
42. Muto, T. et al. TRAF6 functions as a tumor suppressor in myeloid malignancies by directly targeting MYC oncogenic activity. *Cell Stem Cell* **29**, 298–314 e299 (2022).
43. Gudgeon, C. J. et al. High expression of neutrophil elastase predicts improved survival in pediatric acute myeloid leukemia: a report from the Children's Oncology Group. *Leuk. Lymphoma* **54**, 202–204 (2013).
44. Perner, F. et al. YBX1 mediates translation of oncogenic transcripts to control cell competition in AML. *Leukemia* **36**, 426–437 (2022).
45. Jiang, L. et al. Multidimensional study of the heterogeneity of leukemia cells in t(8;21) acute myelogenous leukemia identifies the subtype with poor outcome. *PNAS* **117**, 20117–20126 (2020).
46. Van Nostrand, E. L. et al. Robust transcriptome-wide discovery of RNA-binding protein binding sites with enhanced CLIP (eCLIP). *Nat. Methods* **13**, 508–514 (2016).
47. Sloan, K. E. & Bohnsack, M. T. Unravelling the mechanisms of RNA helicase regulation. *Trends Biochem. Sci.* **43**, 237–250 (2018).
48. Chan, S. P. & Slack, F. J. microRNA-mediated silencing inside P-bodies. *RNA Biol.* **3**, 97–100 (2006).
49. Freimer, J. W., Hu, T. J. & Blelloch, R. Decoupling the impact of microRNAs on translational repression versus RNA degradation in embryonic stem cells. *eLife* **7**, e38014 (2018).
50. Kulkarni, M., Ozgur, S. & Stoecklin, G. On track with P-bodies. *Biochem. Soc. Trans.* **38**, 242–251 (2010).
51. Xue, S. et al. Histone lysine demethylase KDM5B maintains chronic myeloid leukemia via multiple epigenetic actions. *Exp. Hematol.* **82**, 53–65 (2020).
52. Patel, K. P. et al. Acute myeloid leukemia with IDH1 or IDH2 mutation: frequency and clinicopathologic features. *Am. J. Clin. Pathol.* **135**, 35–45 (2011).
53. Bluemn, T. et al. Differential roles of BAF and PBAF subunits, Arid1b and Arid2, in MLL-AF9 leukemogenesis. *Leukemia* **36**, 946–955 (2022).
54. Fog, C. K. et al. Loss of PRDM11 promotes MYC-driven lymphomagenesis. *Blood* **125**, 1272–1281 (2015).
55. Horak, P. et al. TUSC3 loss alters the ER stress response and accelerates prostate cancer growth in vivo. *Sci. Rep.* **4**, 3739 (2014).
56. Katerndahl, C. D. S. et al. Tumor suppressor function of Gata2 in acute promyelocytic leukemia. *Blood* **138**, 1148–1161 (2021).
57. Yu, J. S. et al. PCDH8, the human homolog of PAPC, is a candidate tumor suppressor of breast cancer. *Oncogene* **27**, 4657–4665 (2008).
58. Konopleva, M. & Letai, A. BCL-2 inhibition in AML: an unexpected bonus? *Blood* **132**, 1007–1012 (2018).
59. Park, S. M. et al. IKZF2 drives leukemia stem cell self-renewal and inhibits myeloid differentiation. *Cell Stem Cell* **24**, 153–165 e157 (2019).
60. Roe, J. S. & Vakoc, C. R. The essential transcriptional function of BRD4 in acute myeloid leukemia. *Cold Spring Harb. Symp. Quant. Biol.* **81**, 61–66 (2016).
61. Shi, X. et al. Nuclear NAD(+) homeostasis governed by NMNAT1 prevents apoptosis of acute myeloid leukemia stem cells. *Sci. Adv.* **7**, eabf3895 (2021).
62. Vegi, N. M. et al. MEIS2 is an oncogenic partner in AML1-ETO-positive AML. *Cell Rep.* **16**, 498–507 (2016).
63. Buenrostro, J. D. et al. Integrated single-cell analysis maps the continuous regulatory landscape of human hematopoietic differentiation. *Cell* **173**, 1535–1548 e1516 (2018).
64. Itoh-Nakadai, A. et al. The transcription repressors Bach2 and Bach1 promote B cell development by repressing the myeloid program. *Nat. Immunol.* **15**, 1171–1180 (2014).
65. Iwasaki, H. et al. Distinctive and indispensable roles of PU.1 in maintenance of hematopoietic stem cells and their differentiation. *Blood* **106**, 1590–1600 (2005).
66. Santaguida, M. et al. JunB protects against myeloid malignancies by limiting hematopoietic stem cell proliferation and differentiation without affecting self-renewal. *Cancer Cell* **15**, 341–352 (2009).
67. Gaillard, C. et al. Identification of IRF8 as a potent tumor suppressor in murine acute promyelocytic leukemia. *Blood Adv.* **2**, 2462–2466 (2018).
68. Xhabija, B. & Kidder, B. L. KDM5B is a master regulator of the H3K4-methylome in stem cells, development and cancer. *Semin. Cancer Biol.* **57**, 79–85 (2019).

69. Hinge, A. et al. Asymmetrically segregated mitochondria provide cellular memory of hematopoietic stem cell replicative history and drive HSC attrition. *Cell Stem Cell* **26**, 420–430 e426 (2020).
70. Ho, T. T. et al. Autophagy maintains the metabolism and function of young and old stem cells. *Nature* **543**, 205–210 (2017).
71. Spevak, C. C. et al. Hematopoietic stem and progenitor cells exhibit stage-specific translational programs via mTOR- and CDK1-dependent mechanisms. *Cell Stem Cell* **26**, 755–765 e757 (2020).
72. Herrejon Chavez, F. et al. RNA binding protein SYNCRIP maintains proteostasis and self-renewal of hematopoietic stem and progenitor cells. *Nat. Commun.* **14**, 2290 (2023).
73. Hidalgo San Jose, L. et al. Modest declines in proteome quality impair hematopoietic stem cell self-renewal. *Cell Rep.* **30**, 69–80 e66 (2020).
74. Liu, J., Valencia-Sanchez, M. A., Hannon, G. J. & Parker, R. MicroRNA-dependent localization of targeted mRNAs to mammalian P-bodies. *Nat. Cell Biol.* **7**, 719–723 (2005).
75. Zhao, M., Kim, P., Mitra, R., Zhao, J. & Zhao, Z. TSGene 2.0: an updated literature-based knowledgebase for tumor suppressor genes. *Nucleic Acids Res.* **44**, D1023–D1031 (2016).
76. Park, H. J. et al. Therapeutic resistance in acute myeloid leukemia cells is mediated by a novel ATM/mTOR pathway regulating oxidative phosphorylation. *eLife* **11**, e79940 (2022).

[1]Stem Cells and Regenerative Medicine Center, Baylor College of Medicine, Houston, TX, USA. [2]Center for Cell and Gene Therapy, Baylor College of Medicine, Houston, TX, USA. [3]Department of Molecular and Cellular Biology, Baylor College of Medicine, Houston, TX, USA. [4]Dan L Duncan Comprehensive Cancer Center, Baylor College of Medicine, Houston, TX, USA. [5]Center for Cancer Epigenetics, The University of Texas MD Anderson Cancer Center, Houston, TX, USA. [6]Institute for Medical Biochemistry, University of Veterinary Medicine Vienna, Vienna, Austria. [7]Josep Carreras Leukaemia Research Institute, Badalona, Spain. [8]Division of Biomedical Sciences, School of Medicine, University of California, Riverside, Riverside, CA, USA. [9]Department of Biomolecular Chemistry, University of Wisconsin, Madison, WI, USA. [10]Verna & Marrs McLean Department of Biochemistry & Molecular Biology and Therapeutic Innovation Center, Baylor College of Medicine, Houston, TX, USA. [11]Institute of Pharmacology and Toxicology, University of Veterinary Medicine Vienna, Vienna, Austria. [12]Department of Biology and Biotechnology 'Charles Darwin', Sapienza University of Rome, Rome, Italy. [13]National Center for Quantitative Biology of Complex Systems, Madison, WI, USA. [14]Department of Pediatrics, Baylor College of Medicine, Texas Children's Hospital, Houston, TX, USA. [15]Department of Chemistry, University of Wisconsin, Madison, WI, USA. [16]Morgridge Institute for Research, Madison, WI, USA. [17]Molecular Medicine Program, Division of Urology, Department of Surgery, University of Utah School of Medicine, Salt Lake City, UT, USA. [18]St. Anna Children's Cancer Research Institute (CCRI), Vienna, Austria. [19]CeMM Research Center for Molecular Medicine of the Austrian Academy of Sciences, Vienna, Austria. [20]These authors contributed equally: Srikanth Kodali, Ludovica Proietti. ✉e-mail: jsardina@carrerasresearch.org; Florian.Grebien@vetmeduni.ac.at; bruno.distefano@bcm.edu

Methods

The research conducted in this study complies with all relevant ethical regulations. Experiments using mice were approved and overseen by the Institutional Animal Care and Use Committee of Baylor College of Medicine (IACUC AN-8464) or the Animal Care Committee of the Barcelona Biomedical Research Park (AMM2-17-0030/Daam 9667 and AMM2-22-0031/Daam11883). Experiments using primary human AML cells obtained from patients were approved by the Institutional Ethical Review Board of the Hospital Clinic of Barcelona (HCB/2018/0020) or the Institutional Review Board of Baylor College of Medicine (H-7122/H-3343/H-18245).

Mouse breeding and maintenance

Ddx6$^{fl/fl}$ mice were generated using CRISPR/Cas9-initiated homology-directed repair (HDR) in C57BL/6J background mouse embryos. LoxP sequences were inserted in introns 2 and 3 of the *Ddx6* locus using single-stranded oligodeoxynucleotides. The following sgRNAs were used for targeting: sgRNA intron2: GGGTACTGCGCC AAACTAGA and sgRNA intron3: TAAGGTTATGATATGCAGCT. *Ddx6*$^{fl/fl}$ mice were crossed with *Mx1-Cre* mice (Jackson Laboratory strain 003556, a kind gift of the M. Goodell laboratory) or *Rosa26-ERT2-Cre* mice (Jackson Laboratory strain 008463) to generate mice with inducible knockout of *Ddx6* in haematopoietic cells (*Mx1-Cre*/*Ddx6*$^{fl/fl}$) or in all tissues (*Rosa26-ERT2-Cre*/*Ddx6*$^{fl/fl}$), respectively. To induce *Mx1-Cre*-mediated *Ddx6* deletion in vivo, 250 µg of poly (I:C) (Sigma-Aldrich, cat. no. P1530-100MG) was administered to mice via intraperitoneal (i.p.) injection, every other day for 6 days. To induce *Rosa26-ERT2-Cre*-mediated *Ddx6* deletion, 2 mg of tamoxifen was administered to mice via i.p. injection, every day for 5 days. C57BL/6J (Jackson strain 000664), CD45.1 (Jackson strain 002014) and NSG (Jackson strain 005557, a kind gift of the J. Yustein laboratory and Maksim Mamonkin laboratory) mice were used as recipients for transplantation experiments. Experiments were performed using sex and age-matched mice, ranging from 6–12 weeks old. All mice were maintained in specific-pathogen-free animal facilities.

Cell lines and maintenance

Human AML cells (HEL (DSMZ, ACC 11), SKM-1 (DSMZ, ACC 547), MOLM-13 (DSMZ, ACC 554), HL-60 (DSMZ, ACC 3), MV411 (DSMZ, ACC 102) and THP-1 (ATCC, TIB-202)) were cultured in RPMI 1640 (Sigma-Aldrich) supplemented with 10% FBS (for HEL, HL-60, MV411, THP-1) or 20% FBS (for SKM-1 and MOLM-13), 100 U ml^{-1} penicillin, 100 µg ml^{-1} streptomycin, 2 mM L-glutamine and 50 µM β-mercaptoethanol. HPC7 cells[77] were cultured in IMDM (Sigma-Aldrich) supplemented with 10% FBS, 100 U ml^{-1} penicillin, 100 µg ml^{-1} streptomycin, 2 mM L-glutamine, 1 mM sodium pyruvate, 75 µM monothioglycerol and 100 µg ml^{-1} SCF. Murine CNC cells stably expressing Cas9 (ref. 19) were cultured in RPMI 1640 supplemented with 10% FBS, 100 U ml^{-1} penicillin, 100 µg ml^{-1} streptomycin, 2 mM L-glutamine and 5 ng ml^{-1} IL-3. HEK293T (DSMZ, ACC 635) and Platinum-E (Cell Biolabs, RV-101) cells were cultured in DMEM (Sigma-Aldrich) supplemented with 10% FBS, 100 U ml^{-1} penicillin, 100 µg ml^{-1} streptomycin and 2 mM L-glutamine. Lenti-X cells (Takara Bio, 632180) were cultured in DMEM (Gibco) supplemented with 10% FBS, 100 U ml^{-1} penicillin, 100 µg ml^{-1} streptomycin and 4 mM L-glutamine. All cells were maintained in a humidified incubator at 37 °C and 5% CO_2. Cells were confirmed negative for *Mycoplasma* contamination weekly using a *Mycoplasma* PCR Detection kit (Applied Biological Materials).

Patient AML samples

Primary AML samples were obtained during routine diagnostic procedures from the Hospital Clinic of Barcelona or Baylor College of Medicine, after informed consent from patients. Primary AML cells were cultured in RPMI 1640 supplemented with 20% FBS, 5% L-glutamine, 1% gentamycin, 1% penicillin/streptomycin, 0.6% insulin/transferrin/sodium selenite (ITS) solution (Life Technologies, cat. no. 41400045), 1 mM sodium pyruvate and 0.1× β-mercaptoethanol.

Genome-wide CRISPR/Cas9 dropout screens

The experimental workflow for loss-of-function screening has been previously described[78–80]. In brief, murine CNC and HPC7 cells stably expressing Cas9 were infected with the lentivirally packaged murine Vienna sgRNA library (U6-sgRNA-IT-EIF1as-Thy1.1-P2A-Neo) at a low multiplicity of infection to achieve 500- to 1,000-fold library representations[20]. Transduction efficiency was assessed 3 d after transduction by flow cytometry for Thy1.1. Library-transduced cells were selected using G418 (0.5 mg ml^{-1}) and cell pellets corresponding to at least 500-fold library representations were collected after 14 population doublings. Preparation of next-generation sequencing libraries of screen end point samples and sgRNA plasmid pool was performed as previously described[80] and sequenced on a HiSeqV4 Illumina platform using SR50 mode.

Virus production for transduction of human cells

HEK293T cells were co-transfected with transfer plasmid and packaging plasmids (VSV-G and D8.9 for lentiviral production, VSV-G and Gag-pol for retroviral production), using calcium phosphate transfection. Viral supernatants were collected 24–32 h later and concentrated by ultracentrifugation at 21,000*g* for 2 h at 4 °C. Concentrated viruses were resuspended in Opti-MEM (Gibco) and stored at −80 °C if not used immediately. Cells were transduced by spinfection with virus at 800*g* for 1 h at 32 °C, in the presence of 8 µg ml^{-1} Polybrene.

Alternatively for lentiviral production, Lenti-X cells were co-transfected with 1 µg pMD2.G (Addgene, #12259), 2 µg psPAX2 (Addgene, #12260) and 4 µg transfer vector using polyethyleneimine. Viral supernatants were collected 48 h after transfection, filtered with 0.45-µm filters and stored at 4 °C. Target cells were infected using virus dilutions (1:3–1:10) in the presence of Polybrene (10 µg ml^{-1}) and spinoculated for 90 min at 900*g* at room temperature.

shRNA-mediated gene silencing

For constitutive shRNA-mediated gene silencing, oligonucleotide pairs encoding shRNAs were annealed and cloned into pSICOR-mCherry-puro (Addgene, #31845) or pSICOR-GFP. Knockdowns were confirmed by qRT–PCR.

The following shRNAs were used:

DDX6 shRNA #1: GATCTGTTTACCCGAGGTA

DDX6 shRNA #2: GTATGACCACCACTATTAA

EIF4ENIF1 shRNA: GAAAGAAGATGACTTAGAT

The *LSM14A* shRNA was obtained from the Molecular Profiling Laboratory of the MGH Cancer Center[8]. The shERWOOD UltramiR Lentiviral shRNAs targeting the mouse *Ddx6* gene[8] were purchased from Transomic technologies.

For inducible shRNA-mediated gene silencing, oligonucleotide pairs encoding shRNAs targeting *DDX6*, *RPL17* (positive control) and a non-targeting control were cloned into EcoRI/XhoI-digested pRRL-TRE3G-iRFP670-miR-PGK-Neo backbone (Supplementary Table 2). Human AML cells expressing rtTA3-Puro were transduced with viruses and selected with puromycin (1 µg ml^{-1}) and G418 (0.5 mg ml^{-1}). *DDX6* knockdown was induced with doxycycline (1 µg ml^{-1}) for 72 h and confirmed by qRT–qPCR.

CRISPR/Cas9 knockout in AML cells

An oligonucleotide pair encoding a *DDX6*-targeting gRNA (GTATAA CAGGGTTCTCTGTTC)[81] was annealed and cloned into BsmBI-digested lentiCRISPRv2-puro with FE modification[82]. AML cells were transduced with lentiCRISPRv2-puro viruses and subjected to puromycin selection 2 d later. *DDX6* knockout was confirmed by measuring *DDX6* mRNA and protein.

Oligonucleotide pairs encoding *KDM5B*-targeted gRNAs (sgKDM5B #1: GCAGTGGGCTCACATATCAG, sgKDM5B #2: GAAGGGG-GAGTGCAAATATG) were annealed and cloned into BsmBI-digested lentiCRISPRv2-puro. HL-60 cells were transduced with lentiCRISPRv2-puro viruses and subjected to puromycin selection 2 d later. *KDM5B* knockout was confirmed by measuring KDM5B protein.

Inducible CRISPRi-mediated *DDX6* silencing in HEL cells

Oligonucleotide pairs encoding a non-targeting gRNA (TCGATC GAGGTTGCATTCGG) or a *DDX6*-silencing gRNA (CAGCCAGGCGGC GACTTCGG)[8] were annealed and cloned into BsmBI-digested PB_rtTA_BsmBI (Addgene, #126028).

HEL cells were co-transfected with PB-rtTA-BsmBI, PB_tre_dCas9_KRAB (#126030) and PBase (VectorBuilder) using the Neon Transfection System (Life Technologies). Electroporation parameters used were 1,440 V, 20 ms, two pulses. Cells that stably expressed gRNA, rtTA and dCas9-KRAB were selected with hygromycin B (0.2 mg ml^{-1}) and G418 (0.5 mg ml^{-1}) and were sorted by FACs to generate single-cell clones. *DDX6* silencing was induced by doxycycline (2 μg ml^{-1}) and confirmed by measuring *DDX6* mRNA and protein.

Generation of DDX6 degron AML cells

To replace the endogenous *DDX6* stop codon with a sequence encoding $FKBP12^{F36V}$-HA-2A-mCherry, a donor plasmid was assembled by cloning two 500 bp homology arms of the *DDX6* gene (Twist Biosciences) into pNQL004-SOX2-FKBPV-HA2-P2A-mCherry targeting construct (Addgene, #175552). The donor plasmid and a *DDX6*-targeting sgRNA (AGGGACGUACAUGCUUGUUA, Synthego) were electroporated into Cas9-expressing MOLM-13 and HL-60 cells using the Neon Transfection System. Electroporation parameters used were 1,350 V, 35 ms, one pulse. Cells that stably expressed mCherry were sorted by FACS to generate single-cell clones. Homozygous insertion was confirmed by genotyping PCR using a forward (GGTGGTATGTTCTGTGACTGTTG) and a reverse primer (ATTACCCGGGAAGCTGCATT) in the *DDX6* homology arms and a reverse primer within the mCherry sequence (GCCGTCCT CGAAGTTCATCA). Loss of endogenous DDX6 after dTAG-13 treatment was verified by western blot.

Reversibility of DDX6 loss in AML cells

DDX6-$FKBP12^{F36V}$ MOLM-13 or HL-60 cells were pre-cultured with vehicle (DMSO) or with dTAG-13 (1 μM). These cells were then washed to remove dTAG-13 or were maintained under dTAG-13, while being monitored at the indicated time points for proliferation, DDX6 levels and P-bodies.

Generation of LSM14A-GFP cells

MOLM-13 or HEL cells were co-transfected with PB-rtTA-LSM14A-GFP-BsmBI and PBase using the Neon Transfection System (Life Technologies). Electroporation parameters used were 1,350 V, 35 ms, one pulse (MOLM-13 cells) or 1,400 V, 20 ms, two pulses (HEL cells). Stably transfected cells were selected with puromycin. GFP-labelling of P-bodies was induced by doxycycline (2 μg ml^{-1}) for 6 h.

Rescue of *DDX6* KD AML cells by DDX6 overexpression

shRNA-resistant WT and mutant (E247Q) *DDX6* cDNAs were synthesized as gBlock Gene Fragments (Integrated DNA Technologies) and cloned into pLV-EF1α-IRES-puro (Addgene, #85132) for lentiviral transduction of MOLM-13 cells. After puromycin selection (2 d post-transduction) and recovery, the cells were transduced with control or *DDX6*-targeting shRNA to silence endogenous *DDX6*.

Rescue of *LSM14A* KD AML cells by LSM14A overexpression

WT and mutant FLAG-LSM14A cDNAs (ΔTFG and ΔFFD)[35] were cloned into pMYs-IRES-GFP (Cell Biolabs) for retroviral transduction of HEL cells. shRNA-resistant isoforms were generated by PCR amplification (F-GGATCCCAGTGTGGTGGTAC; R-CAAGaGGGTCCTCTTCATCGG). After sorting for GFP^+ cells (2 d post-transduction) and recovery, the cells were transduced with control or *LSM14A*-targeting shRNA to silence endogenous *LSM14A*.

Disruption of P-bodies using NBDY microprotein

FLAG-NBDY cDNA was cloned into pLV-EF1α-IRES-puro (Addgene, #85132) from FLAG LOC550643 pFCPGW (Addgene, #86853). MOLM-13 and HEL cells were transduced with pLV-EF1α-NBDY-IRES-puro, with pLV-EF1α-IRES-puro empty vector used as a control. After puromycin selection (2 d post-transduction) and recovery, the cells were seeded (3 d post-transduction) for proliferation assays and measurement of P-bodies.

Overexpression of tumour-suppressor genes in AML cells

IDH1, *BACH1*, *TRAF6*, *FBXO30*, *KDM5B* and *ZNF131* cDNAs were PCR-amplified from total MOLM-13 cDNA and cloned into pLV-EF1α-IRES-puro (Addgene, #85132) for lentiviral transduction of MOLM-13 cells, with pLV-EF1α-IRES-puro empty vector used as a control. After puromycin selection (2 d post-transduction) and recovery, the cells were seeded (3 d post-transduction) for proliferation assays.

Rescue of *DDX6* KO AML cells by *KDM5B* knockout

HL-60 cells were subjected to CRISPR/Cas9-mediated double knockout of *KDM5B* and *DDX6*. To measure the effect of the double knockout on cell fitness, we performed a competition-based proliferation assay by infecting HL-60 KDM5B knockout cells (KO #1 and KO #2) with sgDDX6 and sgCTRL linked to an iRFP670 reporter to achieve between 40% and 60% iRFP670-positive cells. The percentage of iRFP670-positive cells was assessed 3 days after lentiviral infection and then measured at regular intervals by flow cytometry. Values were normalized to day 3 after transduction.

Proliferation assays

Cells were plated at 0.5–1 × 10^5 cells per ml, depending on the cell line and counted at the indicated time points via flow cytometry (DAPI or DRAQ7 used as a viability dye) or a haemocytometer (Trypan blue used as a viability dye).

Competition-based proliferation assay

sgRNAs (Supplementary Table 2) were designed using VBC score (vbc-score.org) and cloned into a lentiviral expression vector coupled to iRFP670 (pLenti-hU6-sgRNA-iRFP670). shRNAs (Supplementary Table 2) were designed using SplashRNA (splashrna.mskcc.org) and cloned into either pRRL-SFFV-iRFP670-miR-PGK-Neo (constitutive) or pRRL-TRE3G-iRFP670-miR-PGK-Neo (inducible) backbone. In assays using CRISPR/Cas9 and constitutive shRNA systems, murine and human cell lines stably expressing Cas9 were infected with lentiviral vectors resulting in sgRNA/shRNA-iRFP670 expression. The ratio of iRFP670-positive cells was assessed 3 d after infection and monitored in regular intervals by flow cytometry. Values were normalized to day 3 or day 5 post-transduction. In assays using TRE3G-driven shRNA-iRFP670 expression, human cells expressing rtTA3 were treated with doxycycline (1 μg ml^{-1}) and the fraction of iRFP670-positive cells was determined at 72 h after induction and monitored over time using flow cytometry. Values were normalized to day 3 post-induction. Cytometric measurements were performed using IntelliCyt IQue Screener Plus (BioScience, Sartorius Group).

In vitro chemical treatment

HEL cells were cultured in the presence of 10 nM PMA for 4 d to induce megakaryocytic differentiation. To induce myeloid differentiation, MOLM-13 cells were treated with the anti-leukaemic drug EPZ-5676 (1 μM) for 5 d.

Overexpression of *DDX6* in HPC7 cells

WT *DDX6* cDNA was synthesized as a gBlock Gene Fragment (Integrated DNA Technologies) and cloned into pLV-EF1α-IRES-puro (Addgene, #85132) for lentiviral transduction of HPC7 cells, with pLV-EF1α-IRES-puro empty vector used as a control. After puromycin selection (2 d post-transduction) and recovery, the cells were used for measurement of P-body numbers (10 d post-transduction).

Primary human CD34$^+$ cell transduction and colony-forming unit assay

Primary human bone-marrow CD34$^+$ cells (STEMCELL Technologies, cat. no. 70002.3) were cultured in StemSpan SFEM (STEMCELL Technologies, cat. no 9600) supplemented with StemSpan TM CC100 (STEMCELL Technologies, cat. no 2690). Control or *DDX6* shRNA-expressing viruses were centrifuged onto RetroNectin-coated plates prepared according to manufacturer's instructions. Cells were transduced in virus-coated plates by spinfection in the presence of 8 μg ml^{-1} Polybrene at 800*g* for 1 h at 32 °C. After 3 d, GFP$^+$ cells were sorted for use in experiments.

To assess colony formation, 1,000 cells were plated on MethoCult (STEMCELL Technologies, cat. no. H4434) according to manufacturer´s instructions. Colonies (BFU-E, CFU-M, CFU-G, CFU-GM and CFU-GEMM) were counted and scored at day 13 using standard morphological criteria.

Murine colony-forming assay

Rosa26/Cre-ERT2 or *Rosa26-Cre-ERT2/Ddx6*$^{fl/fl}$ c-Kit$^+$ HSPCs or AML1-ETO9a$^+$ leukaemic cells were plated in StemSpan SFEM (STEMCELL Technologies cat. no. 09600) supplemented with SCF (50 ng ml^{-1}), TPO (10 ng ml^{-1}), Flt-3 (20 ng ml^{-1}), IL-3 (10 ng ml^{-1}) and IL-6 (10 ng ml^{-1}) and treated with 4-hydroxytamoxifen (200 nM) for 2 d. Cells were then plated in MethoCult M3434 (STEMCELL Technologies cat. no. 03434) and colonies were counted at 7 d post-plating.

Xenotransplantation of human AML cell lines and primary AML

MOLM-13 cells transduced with control or *DDX6* shRNA-expressing viruses were selected 30 h later with puromycin (1 μg ml^{-1}). After 2 d of selection, 2.5–5 × 10^5 transduced cells were injected into NSG mice that had been sublethally irradiated (250 cGy) the previous day.

CRISPRi HEL cells (2.5 × 10^6) were injected into NSG mice that had been sublethally irradiated (250 cGy) the previous day. Mice were placed on doxycycline feed 7 d after transplantation to induce *DDX6* silencing.

GFP-expressing primary AML patient cells (1–2 × 10^5) were sorted 2 d after transduction with control or *DDX6* shRNA-expressing viruses and injected directly into the bone marrow of sublethally irradiated (200 cGy) NSG mice. Engraftment was assessed by monitoring the peripheral blood. Mice were closely monitored and killed according to clinical signs of sickness became apparent.

Analysis of steady-state haematopoiesis in vivo

Mx1-Cre or *Mx1-Cre/Ddx6*$^{fl/fl}$ mice were injected with 250 μg of poly (I:C) via i.p. injection (every other day for 6 d) to delete *Ddx6*. After 110 d, mice were killed and peripheral blood, spleen and bone marrow were collected for analysis of haematopoietic stem cells and multipotent progenitors (CD11b$^-$Gr-1$^-$CD3$^-$CD19$^-$ (Lin$^-$)Sca-1$^+$c-Kit$^+$ (LSK)), committed progenitors (Lin$^-$Sca-1$^-$c-Kit$^+$ (LK)), erythroid progenitors (CD71$^+$Ter119$^+$), erythrocytes (CD71$^-$Ter119$^+$), myeloid cells (CD11b$^+$), T cells (CD11b$^-$CD3$^+$) and B cells (CD11b$^-$CD19$^+$).

Serial competitive transplantation

For primary competitive transplants, 1 × 10^6 bone-marrow cells (CD45.2$^+$), isolated from either *Mx1*-Cre or *Mx1-Cre/Ddx6*$^{fl/fl}$ mice 110 d after poly(I:C) treatment, were co-transplanted with 1 × 10^6 CD45.1 competitor bone-marrow cells into lethally irradiated (two doses of 600 cGy, 3 h apart) WT recipient mice (6–8 weeks old).

For secondary competitive transplants, 1 × 10^5 *Ddx6*^{WT} or *Ddx6*^{KO} bone-marrow cells, isolated from primary recipients 122 days post-transplant, were co-transplanted with 1 × 10^5 CD45.1 competitor bone-marrow cells into lethally irradiated WT recipient mice.

Competitive transplantation of HSCs

A total of 200 CD45.1 HS cells and 200 *Mx1-Cre/Ddx6*$^{fl/fl}$ HS cells were co-transplanted with 1 × 10^6 bone marrow filler cells into lethally irradiated WT recipient mice. Recipient mice were treated with poly(I:C) 34 d later to induce *Ddx6* deletion.

Generation and transplantation of pre-leukaemia cells

FLAG-MLL-AF9 was cloned from pMIG-FLAG-MLL-AF9 (Addgene, #71443) into pMYs-IRES-GFP (Cell Biolabs). AML1-ETO9a was cloned from MigR1-AE9a (Addgene, #12433) into IRES-mCherry (Addgene, #80139). For virus production, Platinum-E (PLAT-E) cells (Cell Biolabs) were transfected with pMYs-FLAG-MLL-AF9-IRES-GFP or AML1-ETO9a-IRES-mCherry by calcium phosphate transfection. Viral supernatants were collected 48 h later and centrifuged onto RetroNectin-coated plates prepared according to the manufacturer's instructions (Takara Bio).

HSPCs were enriched from the bone marrow of mice using anti-mouse CD117 magnetic beads (BD Biosciences cat. no. 558620) and cultured for 24 h in StemSpan SFEM (STEMCELL Technologies) supplemented with 10 ng ml^{-1} IL-3, 10 ng ml^{-1} IL-6, 50 μg ml^{-1} SCF, 50 μg ml^{-1} TPO (all from PeproTech) and 50 μg ml^{-1} gentamicin. Cells were transduced in virus-coated plates by spinfection at 800*g* for 1 h at 32 °C and transplanted the following day into sublethally irradiated C57BL/6J mice (600 cGy). Three weeks after transplant, when GFP$^+$ or mCherry$^+$ cells could be detected in the peripheral blood, mice were either injected with 250 μg poly (I:C) via i.p. injection, every other day for 6 days, or 2 mg of tamoxifen, via i.p. injection, every day for 5 days, to delete *Ddx6*. Mice were monitored and killed as soon as clinical signs of sickness became apparent.

Flow cytometry

To detect surface markers, cells were first incubated with Fc blocker (anti-CD16/CD32) for 10 min on ice to prevent background staining. Cells were then stained with appropriate fluorophore-conjugated antibodies on ice, protected from light, for 15 min. After staining, DAPI or DRAQ7 was added where appropriate to mark dead cells.

The following antibodies were used for staining of cell surface markers: APC anti-human CD123 (1:300 dilution) (BioLegend, cat. no. 306011), APC anti-human CD61 (1:300 dilution) (BioLegend, cat. no. 336411), APC anti-rat CD90/mouse CD90.1 (1:200 dilution) (BioLegend, cat. no. 202526), FITC-anti-human CD41 (1:300 dilution) (BioLegend, cat. no. 303703), APC anti-human HLA-ABC (1:300 dilution) (BD Biosciences, cat. no. 555555), FITC-anti-human HLA-ABC (1:300 dilution) (BD Biosciences, cat. no. 560965), PE-anti-human CD33 (1:300 dilution) (BD Biosciences, cat. no. 555333), APC anti-mouse CD45 (1:300 dilution) (BD Biosciences, cat. no. 559864), APC anti-mouse Gr-1 (1:300 dilution) (BioLegend, cat. no. 108411), Pacific Blue anti-mouse CD45.2 (1:300 dilution) (BioLegend, cat. no. 109819), Pacific Blue anti-mouse CD3 (1:300 dilution) (BioLegend, cat. no. 100213), Pacific Blue anti-Gr-1 (1:300 dilution) (BioLegend, cat. no. 108429), Pacific Blue anti-CD19 (1:300 dilution) (BioLegend, cat. no. 115526), Pacific Blue anti-CD11b (1:300 dilution) (BioLegend, cat. no. 101223), Brilliant Violet 711-anti-mouse Sca-1 (1:300 dilution) (BioLegend, cat. no. 108131), APC anti-mouse Ter119 (1:300 dilution) (BioLegend, cat. no. 116211), FITC-anti-mouse CD45.1 (1:300 dilution) (BioLegend, cat. no. 110705), FITC-anti-mouse CD71 (1:300 dilution) (Invitrogen, cat. no. 110711), FITC-anti-CD48 (1:300 dilution) (BioLegend, cat. no. 103403), PE/Cy7-anti-mouse CD11b (1:300 dilution) (BioLegend, cat. no. 101216),

PerCP/Cy5.5-anti-mouse CD19 (1:300 dilution) (BioLegend, cat. no. 1155335), PerCP/Cy5.5-anti-mouse/human CD11b (1:300 dilution) (BioLegend, cat. no. 101227), PerCP/Cy5.5-anti-mouse Gr-1 (1:300 dilution) (BioLegend, cat. no. 108427), PerCP/Cy5.5-anti-mouse CD3 (1:300 dilution) (BioLegend, cat. no. 100217), PE-anti-mouse CD150 (1:300 dilution) (BioLegend, cat. no. 115903), PE-anti-mouse CD3 (1:300 dilution) (BioLegend, cat. no. 100205), APC anti-mouse c-Kit (1:300 dilution) (BioLegend, cat. no. 105811), APC/Fire-750-anti-mouse CD16/32 (1:300 dilution) (BioLegend, cat. no. 101317), Alexa Fluor 700-anti-mouse CD48 (1:300 dilution) (BioLegend, cat. no. 103425) and PE/Cy7-anti-mouse CD34 (1:300 dilution) (BioLegend, cat. no. 152217).

To measure apoptosis, cells were incubated at room temperature and protected from light for 15–30 min with APC anti-annexin V (BioLegend, cat. no. 640920) or Pacific Blue anti-annexin V (Thermo Fisher, cat. no. A35136) (1:300 dilution), according to the manufacturer's instructions and DAPI or SYTOX AADvanced Dead Cell Stain (Thermo Fisher, cat. no. S10349).

For intracellular staining of cytoplasmic proteins, cells were fixed with 4% methanol-free formaldehyde for 15 min at room temperature, then permeabilized and blocked with 0.1% Triton-X containing 2% donkey serum. Cells were labelled with primary antibodies against the desired intracellular markers and then stained with fluorophore-conjugated secondary antibodies if needed. The following antibodies were used for intracellular flow cytometry: APC anti-FLAG (1:300 dilution) (BioLegend, cat. no. 637307), FITC-anti-human CD68 (1:200 dilution) (BioLegend, cat. no. 333805), rabbit anti-human DDX6 (1:400 dilution) (Novus Biologicals, cat. no. NB-200-192), rabbit anti-human KDM5B (1:300 dilution) (Abcam, cat.no. ab181089), Alexa Fluor 488-donkey anti-rabbit IgG (H+L) (1:400 dilution) (Invitrogen, cat. no. A21206), Alexa Fluor 594-donkey anti-rabbit IgG (H+L) (1:400 dilution) (Invitrogen, cat. no. A21207), Alexa Fluor 647-donkey anti-rabbit IgG (H+L) (1:400 dilution) (Invitrogen cat. no. A31573), Alexa Fluor 647-goat anti-rabbit IgG (1:200 dilution) (Invitrogen, cat. no. A21244), Alexa Fluor 594-donkey anti-mouse IgG (1:400 dilution) (Invitrogen, cat. No. A21203). For intracellular staining of Ki-67, cells were fixed and permeabilized using Transcription Factor Buffer Set (BD Biosciences, cat. no. 562574), according to manufacturer's instructions, followed by staining with FITC-anti-mouse/human Ki-67 (1:300 dilution) (BioLegend, cat. no.151211).

Samples were acquired through FACSDiva software on an LSR-II, LSR-Fortessa or FACSCanto II (BD Biosciences), or through CytExpert software on a CytoFLEX S (Beckman Coulter). Samples were sorted on a FACSAria or Influx (BD Biosciences). All flow cytometry data were analysed on FlowJo v.10.8.2 (BD Biosciences) or CytExpert (Beckman Coulter).

Measurement of mitochondrial mass and activity

Ddx6^{WT} and *Ddx6*^{KO} HSCs were incubated in StemSpan SFEM supplemented with SCF (50 ng ml^{-1}), TPO (10 ng ml^{-1}), Flt-3 (20 ng ml^{-1}), IL-3 (10 ng ml^{-1}) and IL-6 (10 ng ml^{-1}), in the presence of 100 nM MitoTracker Green FM (Invitrogen) or 25 nM TMRM (Invitrogen), for 15 min at 37 °C and 5% CO_2. Cells were then analysed by flow cytometry.

Western blot

Samples were lysed in RIPA buffer (50 mM Tris-HCl (pH 8.0), 150 mM NaCl, 0.1% SDS, 0.5% sodium deoxycholate, 1% Triton-X-100, 1 mM EDTA, protease inhibitors and Benzonase). Lysates were subjected to standard western blotting using the following antibodies: rabbit anti-human/mouse DDX6 (1:2,000 dilution) (Novus Biologicals, cat. no. NB-200-192), rabbit anti-human/mouse 4E-T (1:500 dilution) (Thermo Fisher, cat. no. A300-706A), rabbit anti-human LSM14B (1:250 dilution) (Atlas Antibodies, cat. no. HPA061189), rabbit anti-human LSM14A (1:500 dilution) (Proteintech, cat. no. 18336-1-AP), mouse anti-HA (1:24,000 dilution) (BioLegend, cat. no. 901516), rabbit anti-human ATXN2L (1:1,000 dilution) (Bethyl Laboratories, cat. no. A201-370), rabbit anti-human DCP1B (1:1,000 dilution) (Cell Signaling, cat. no. 13233), rabbit anti-human/mouse histone H3 (132000) (Cell Signaling, cat. no. 4499S), rabbit anti-human/mouse vinculin (1:2,000 dilution) (Cell Signaling, cat. no. 13901S), HRP-rabbit anti-human/mouse β-actin (1:3,000 dilution) (Cell Signaling, cat. no. 5125), HRP donkey anti-rabbit IgG (1:3,000 dilution) (BioLegend, cat. no. 406401), HRP-horse anti-mouse IgG (1:3,000 dilution) (Cell Signaling, cat. no. 7076P2).

Subcellular fractionation

Cells were lysed in nuclear isolation buffer (50 mM Tris-HCl (pH 8.0), 60 mM KCl, 15 mM NaCl, 5 mM $MgCl_2$, 1 mM $CaCl_2$, 250 mM sucrose, 0.6% IGEPAL, 1 mM dithiothreitol (DTT), 1× protease inhibitors, 1× phosphatase inhibitors) and subjected to centrifugation (960*g* for 5 min) to separate nuclear and cytoplasmic fractions. Nuclei and cytoplasm were then lysed in RIPA buffer (50 mM Tris-HCl (pH 8.0), 150 mM NaCl, 0.1% SDS, 0.5% sodium deoxycholate, 1% Triton-X-100, 1 mM EDTA, protease inhibitors and Benzonase), sonicated and centrifuged (21,000*g* for 5 min). Enrichment for nuclear and cytoplasmic fractions was confirmed by immunoblotting for histone H3 and vinculin, respectively.

Immunocytochemistry and microscopy for P-bodies

Cells were cytospun onto glass slides, fixed with 4% methanol-free formaldehyde for 15 min at room temperature. Cells were then permeabilized and blocked with 0.1% Triton-X containing 2% donkey serum. Cells were labelled with mouse anti-mouse/human DDX6 (1:200 dilution) (Sigma-Aldrich, cat. no. SAB4200837) and rabbit anti-mouse/human EDC4 (1:200 dilution) (Abcam, cat. no. ab72408) or LSM14A (1:200 dilution) (GeneTex, cat. no. GTX120902) at 4 °C overnight and then stained with Alexa Fluor 594-donkey-anti-mouse IgG (H+L) (1:300 dilution) and Alexa Fluor 488-donkey anti-rabbit IgG (H+L) (1:300 dilution) for 1 h at room temperature. Nuclei were counterstained with DAPI. Slides were mounted with ProLong Diamond (Life Technologies) and allowed to cure at room temperature. Images were acquired by confocal microscopy, via ZEN Blue software (Zeiss), using a ×40 or ×63 objective lens on an LSM 900 with Airyscan 2 (Zeiss) and analysed using ImageJ software.

Single-molecule FISH

For *POLK* smFISH, commercially designed probes were purchased from Stellaris. For *KDM5B* and *RSRC2* smFISH, primary (unconjugated) and secondary probes (Cy5-conjugated) were designed according to the method of Tsanov et al.[83] and purchased from Sigma-Aldrich. GFP-LSM14A^{+}-expressing cells were subjected to smFISH for *POLK*, *KDM5B* and *RSRC2* as previously described[83]. Slides were imaged by epifluorescence microscopy using an Olympus IX83 inverted microscope equipped with a ×60 oil immersion objective lens.

Image quantification was performed by running FISH-Quant[84] in MATLAB R2023a. In brief, cytoplasmic and nuclear boundaries for individual cells were defined through automatic ImageJ-based segmentation, based on diffuse Cy5 and DAPI fluorescence, respectively. Single mRNA molecules and P-bodies were automatically identified as Cy5^{+} punctae and GFP^{+} punctae, respectively, within the cytoplasm. The fraction of mRNA molecules colocalizing with P-bodies was automatically calculated.

Quantification of P-bodies

Following immunocytochemistry and confocal microscopy, images were processed using ImageJ to quantify P-bodies. Specifically, P-bodies were identified as punctae exhibiting colocalization between DDX6 and EDC4 or DDX6 and LSM14A (EDC4^{+}DDX6^{+} or LSM14A^{+}DDX6^{+} punctae). P-bodies were automatically counted using FISH-Quant, combined with manual, blinded counting for corroboration of results.

Quantitative RT–PCR

RNA was prepared from cells using a Monarch Total RNA Miniprep kit (NEB) and reverse transcribed to cDNA using a High-Capacity RNA-to-cDNA kit (Applied Biosystems) or RevertAid first-strand cDNA Synthesis kit (Thermo Fisher Scientific), according to manufacturer's instructions. A master mix consisting of Luna Universal qPCR Master Mix (NEB) or SsoAdvanced Universal SYBR Green Supermix (Bio-Rad) and pre-designed primers (0.5 µM) against target genes (Sigma-Aldrich) was prepared. Each reaction consisted of 5.5 µl master mix and 4.5 µl cDNA diluted ninefold in nuclease-free water. Real-time PCR was performed in 96-well PCR plates (Bio-Rad) on a CFX96 Real-Time PCR Detection System (Bio-Rad). Cycling conditions were as follows: 95 °C for 1 min, then 40 cycles of 95 °C for 15 s and 60 °C for 30 s. *ACTB* or *GAPDH* was used as an internal control. Primers are available upon request.

DNA preparation

DNA was extracted using the DNeasy Blood & Tissue kit (QIAGEN) and quantified using the Qubit dsDNA High Sensitivity kit (Life Technologies).

P-body purification

P-body purification was performed as previously described[9]. In brief, LSM14A-GFP-expressing cells were lysed for 20 min on ice in lysis buffer (50 mM Tris, pH 7.4, 1 mM EDTA, 150 mM NaCl, 0.2% Triton-X-100) supplemented with 65 U ml^{-1} RNaseOut ribonuclease inhibitor (Promega) and EDTA-free protease inhibitor cocktail (Roche Diagnostics). Lysates were centrifuged at 200*g* for 5 min at 4 °C to remove nuclei. Residual DNA was removed by incubation in the presence of 10 mM $MgSO_4$, 1 mM $CaCl_2$ and 4 U ml^{-1} of RQ1 DNase (Promega) for 30 min at room temperature. Following centrifugation at 10,000*g* for 7 min at 4 °C, pellets were resuspended in 40 µl lysis buffer containing 80 U RNaseOut (Promega) to generate the cytoplasmic fraction. From this fraction, P-bodies were sorted on a FACSAria, pelleted by centrifugation at 10,000*g* for 7 min at 4 °C and stored at −80 °C, along with an aliquot of matching, pre-sort cytoplasmic fraction.

RNA-seq

Total RNA was isolated from cells using the miRNeasy Micro kit (QIAGEN), according to the manufacturer's instructions. Polyadenylated RNAs were enriched and cDNA libraries were constructed using the NEBNext Ultra II Directional RNA Library Prep kit for Illumina (New England BioLabs). Libraries were sequenced on a NextSeq 550 (Illumina) with paired-end 75-bp reads or a HiSeq 4000 (Illumina) with paired-end 150 bp reads.

For P-body-seq, RNA was isolated from P-body and cytoplasmic fractions using the miRNeasy Micro kit (QIAGEN). cDNA libraries were constructed using the SMART-Seq V4 ultra+ Nextera XT kit for Illumina (Takara Bio). Libraries were sequenced with paired-end 150-bp reads.

Small RNA-seq

Purified total RNA from CTRL and *DDX6* KD HEL and MOLM-13 cells was mixed with RNA loading dye (New England Biolabs, B0363S) by equal volume and then it was incubated at 75 °C for 5 min. The mixture was loaded into 15% (wt/vol) urea polyacrylamide gel and ran in a 1× TBE running buffer at 200 V until the bromophenol blue reached the bottom of the gel. After staining with SYBR Gold solution (Invitrogen, S11494), the gel that contained 15–50 nucleotides RNAs was excised based on small RNA ladders (New England Biolabs (N0364S) and Takara (3416)) and eluted in 0.3 M sodium acetate (Invitrogen, AM9740) and 100 U ml^{-1} RNase inhibitor (New England Biolabs; M0314L) overnight at 4 °C. The sample was then centrifuged for 10 min at 12,000*g* (4 °C). The aqueous phase was mixed with pure ethanol, 3 M sodium acetate and linear acrylamide (Invitrogen, AM9520) at a ratio of 3:9:0.3:0.01. Then, the sample was incubated at −20 °C for 2 h and centrifuged for 25 min at 12,000*g* (4 °C). After removing the supernatant, the precipitation was resuspended in nuclease-free water, quantified and stored at −80 °C or used for further processing. The size-separated RNAs were incubated in a 50-µl reaction mixture containing 5 µl 10× PNK buffer (New England Biolabs, B0201S), 1 mM ATP (New England Biolabs, P0756S), 10 U T4PNK (New England Biolabs, M0201L) and RNA at 37 °C for 20 min. Then, the mixture was added to 500 µl TRIzol reagent to perform the RNA isolation procedure. After purification, the RNAs were incubated in a 50-µl reaction mixture containing 50 mM HEPES (pH 8.0), 75 µM ferrous ammonium sulfate (pH 5.0), 1 mM α-ketoglutaric acid, 2 mM sodium ascorbate, 50 mg l^{-1} bovine serum albumin (Sigma-Aldrich, A7906-500G), 2,000 U ml^{-1} RNase inhibitor and equal concentrations of AlkB and RNA at 37 °C for 30 min. Then, the mixture was added to 500 µl TRIzol reagent to perform the RNA isolation. Small RNA libraries were constructed using the NEBNext Small RNA Library Prep Set for Illumina (New England Biolabs, E7330S). Libraries were amplified and sequenced using the SE100 strategy on the Illumina system by the University of California, San Diego IGM Genomics Center.

ATAC-seq

ATAC-seq was performed as previously described[85], using MOLM-13 and HEL cells 7 d after transduction with control or *DDX6* shRNA-expressing viruses. Then, 1×10^5 cells were washed once with 100 ml PBS and resuspended in 50 ml lysis buffer (10 mM Tris-HCl, pH 7.4, 10 mM NaCl, 3 mM $MgCl_2$ and 0.2 % IGEPAL CA-630). The suspension of nuclei was then centrifuged for 10 min at 500*g* at 4 °C, followed by the addition of 50 ml transposition reaction mix (25 ml TD buffer, 2.5 ml Tn5 Transposase and 22.5 ml nuclease-free water) and incubation at 37 °C for 30 min. DNA was isolated using MiniElute kit (QIAGEN). Libraries were amplified by PCR (13 cycles). After the PCR reaction, the library was size-selected for fragments between 100 bp and 1,000 bp using AmpureXP beads (Beckman Coulter). Before sequencing, libraries were purified with QiaQuick PCR (QIAGEN) and integrity-checked on a Bioanalyzer.

CUT&RUN

To analyse each histone mark, 100,000 cells were collected in low-binding 1.5-ml tubes. The cells were washed thrice with 1 ml wash buffer consisting of 20 mM HEPES, pH 7.5, 150 mM NaCl, 0.5 mM spermidine (Merck, S0266) and 1× protease inhibitor cocktail (Merck, 11873580001) and then centrifuged at 600*g*. Subsequently, the cells were suspended in 1 ml wash buffer and 10 µl per histone mark of activated concanavalin A-conjugated paramagnetic beads (EpiCypher, 21-1401) were added. To activate the beads, they were previously washed twice with binding buffer consisting of 20 mM HEPES, pH 7.5, 10 mM KCl, 1 mM $CaCl_2$ and 1 mM $MnCl_2$. Finally, they were resuspended in a volume of binding buffer equal to the starting volume. Cells were incubated in rotation at room temperature for 10 min and then were divided into equivalent aliquots in low-binding 1.5-ml tubes. The supernatant was removed and the bead-bound cells were resuspended in 150 µl antibody buffer containing the wash buffer supplemented with 2 mM EDTA and 0.1% digitonin (Merck, 300410). After adding the desired antibody, samples were incubated overnight at 4 °C while rotating. The antibodies used were α-H3K27ac at 1:300 dilution (Diagenode, C15410196), α-H3K4me1 at 1:200 dilution (Diagenode, C15410194) and anti-IgG as a negative control at 1:100 dilution (Diagenode, C15410206). To remove excess antibody, the bead-bound cells were washed twice in digitonin-wash buffer. After that, the cells were suspended in 150 µl digitonin-wash buffer, which was supplemented with 700 ng ml^{-1} pAG-MNase (synthesized in-house) and left to incubate for 1 h at 4 °C while rotating. To remove excess pAG-MNase, the cells bound by beads were washed twice in digitonin-wash buffer. Afterwards, 100 µl digitonin-wash buffer supplemented with 2 mM CaCl2 was used to activate the MNase. This mixture was left to incubate on ice for 30 min, allowing for chromatin cleavage. To stop the enzymatic reaction, 100 µl 2× STOP buffer

(340 mM NaCl, 20 mM EDTA, 4 mM EGTA, 0.05% digitonin, 50 μg m^{-1} RNase A (Thermo Fisher Scientific, EN0531) and 50 μg ml^{-1} glycogen (Sigma, 10901393001)) was added and samples were incubated at 37 °C for 30 min. The supernatants were retrieved and proteins were removed from the DNA by incubating the samples with SDS 10% and proteinase K 10 mg ml^{-1} for 1 h at 50 °C. Then, DNA was purified using phenol:chloroform:isoamyl alcohol 25:24:1 extraction, followed by a chloroform extraction according to the manufacturer's instructions in phase-lock gel tubes to minimize material loss. The purified DNA was ethanol-precipitated, centrifuged at >20,000*g* 4 °C and the dried pellet was resuspended in 50 μl buffer containing 10 mM Tris-HCl, pH 8.0 and 0.1 mM EDTA. Library construction was performed using the Kapa HyperPrep kit (Roche, 07962363001) and Illumina's TruSeq adaptor system. Quantity and quality of the CUT&RUN libraries were assessed by automated electrophoresis using a high-sensitivity DNA ScreenTape Analysis (Agilent, 5067-5584) on an Agilent 2200 TapeStation.

CUT&Tag

CUT&Tag experiments were performed using the iDeal CUT&Tag kit for Histones (Diagenode, cat. no. C01070020) following manufacturer's instructions. In brief, HL-60 cells were treated with doxycycline (1 μg ml^{-1}) for 5 d to induce shRNA expression. Next, HL-60 shDDX6 and shCTRL samples (300,000 cells for each biological replicate) were collected for CUT&Tag. Samples were washed with complete CT Wash Buffer and subsequently incubated with ConA beads on a rotator. Cells were permeabilized with Complete CT Antibody Buffer and incubated with 1 μg of either anti-H3K27ac (ab4729) (Abcam), anti-H3K4me3 (C1541003) (Diagenode), anti-H3K9me3 (C15410193) (Diagenode), anti-H3K27me3 (C15410195) (Diagenode) or anti-rabbit IgG (Antibody Package for CUT&Tag anti-rabbit, Diagenode) antibodies overnight at 4 °C on a rotator. After removing supernatant, anti-rabbit secondary antibody (Antibody Package for CUT&Tag anti-rabbit, Diagenode) was added to samples and incubated for 45 min at room temperature, followed by washing with complete CT Wash Buffer 2. pA-Tn5 transposase was diluted 1:250 in complete CT Wash Buffer 3 and added to samples, followed by 1 h incubation at room temperature. After washing with complete CT Wash Buffer 3, CT Tagmentation Buffer was added to the samples to activate tagmentation and incubated at 37 °C for 1 h at 800 rpm. To stop tagmentation, CT Buffer E, CT Buffer S and proteinase K were added and samples were incubated at 55 °C for 1 h at 800 rpm. DNA isolation was performed using the provided spin columns. For library amplification, isolated DNA was mixed with primer index pairs (24 UDI for Tagmented libraries Set II, Diagenode) and 2× High-Fidelity Mastermix, according to manufacturer's PCR protocol. Library isolation was performed using AMPure XP beads (Beckman Coulter) and measured with an Agilent TapeStation (Agilent Technologies) to assess the quality, size and concentration of the library. Libraries were sequenced on the Illumina NextSeq2000 instrument (Illumina) in PE50 mode.

eCLIP-seq for DDX6

A total of 2×10^7 MOLM-13 cells per replicate were UV-crosslinked (400 mJ cm^{-2}) to stabilize RBP–RNA interactions, then lysed. The whole cell lysates were sonicated and subjected to limited digestion with RNase I (40 U ml^{-1} of lysate), followed by immunoprecipitation for DDX6–RNA complexes using anti-DDX6 antibody (NB-200-192, Novus). Before immunoprecipitation, an aliquot of each extract was set aside and stored at 4 °C to prepare the size-matched input control. Complexes were collected using anti-rabbit magnetic beads, washed, dephosphorylated and 3′-ligated on-bead to custom oligonucleotides. All samples were run on 4–12% polyacrylamide gradient gels and complexes transferred to nitrocellulose membranes. Successful immunoprecipitation was confirmed by parallel western blotting using the same anti-DDX6 antibody as described above. DDX6–RNA complexes were excised from the membrane and RNAs released with proteinase K. Size-matched input samples were dephosphorylated and 3′-ligated. All samples were reverse transcribed and cDNAs 5′-ligated on-bead, quantified by qPCR and PCR-amplified (<18 cycles), followed by size selection (175–350 bp) on agarose gels and sequencing of libraries. Remaining steps of eCLIP, including read processing and peak calling, were performed as previously described[86] for two replicates of DDX6 and one paired size-matched input. Region-level analysis was performed as previously described[87].

Polysome profiling

Doxycycline (1 μg ml^{-1}) was added for 72 h to HL-60 cells to induce shRNA expression. Next, HL-60 shDDX6 and shCTRL cells (10–20 million for each biological replicate) were treated with 100 μg ml^{-1} cycloheximide (CHX) (Sigma-Aldrich) for 5 min at 37 °C. Cells were collected, washed with ice-cold PBS supplemented with 100 μg ml^{-1} CHX and centrifuged. After centrifugation, cell pellets were resuspended in 500 μl lysis buffer (10 mM Tris-HCl, pH 7.4, 100 mM NaCl, 10 mM $MgCl_2$, 1% Triton-X and 10 mM DTT) supplemented with 100 μg ml^{-1} CHX, 1 RNase inhibitor (Thermo Fisher Scientific) and 1× protease inhibitor cocktail (Complete, EDTA-free, Roche), incubated for 5 min on ice and centrifuged for 5 min at 2,000 rpm. Then, 100 μl lysate was reserved for inputs and 400 μl lysate was used for fractionation. For fractionation, a 15–50% sucrose gradient was prepared in polysome buffer (10 mM Tris-HCl, pH 7.4, 100 mM NaCl and 10 mM $MgCl_2$). Samples were loaded on the sucrose gradient and centrifuged at 37,000 rpm with a SW41 rotor (Beckman) for 2 h at 4 °C. Fractions were collected from the bottom and UV absorbance was monitored using Bio-logic LP low-pressure chromatography system (Bio-Rad). Fractions containing monosomes and polysomes were identified based on their UV absorbance and pooled. Total RNA from the inputs and each pool were extracted using TRIzol LS (Thermo Fisher) and validated using TapeStation System and High Sensitivity RNA ScreenTape kit (Agilent Technologies). Eukaryotic strand-specific mRNA sequencing libraries were prepared and validated using Agilent 2100 Bioanalyzer (Agilent Technologies). Libraries were sequenced on the HiSeq 4000 Illumina platform in PE100 mode, resulting in approximately 24 million reads per sample.

LC–MS/MS proteomics

MOLM-13 cells were collected 7 d after transduction with control or *DDX6* shRNA. Cells were resuspended in 100 μl 5.4 M guanidine hydrochloride in 100 mM Tris-HCl, pH 8.0, then gently vortexed at ambient temperature for at least 20 min. A bicinchoninic acid (BCA) protein assay (Pierce) was performed according to the manufacturer's instructions, then sufficient guanidine hydrochloride in 100 mM Tris-HCl, pH 8.0 was added to bring the protein concentration of each resuspended cell pellet to 1 mg ml^{-1}. Then, 50 μg protein from each cell pellet was transferred into separate 1.5-ml microcentrifuge polypropylene tubes. Samples were incubated in a sand bath at 110 °C for 5 min, cooled at room temperature for 5 min, then incubated once more in a sand bath at 110 °C for 5 min. Then, 450 μl liquid chromatography–mass spectrometry (LC–MS)-grade methanol was added to each sample and vortexed for 10 s. Each sample was then centrifuged at 14,000*g* for 2 min at 4 °C to pellet the protein. After the supernatants were carefully discarded, each pellet was resuspended in 50 μl lysis buffer (8 M urea, 100 mM Tris-HCl, pH 8.0, 10 mM TCEP and 40 mM 2-chloroacetamide) and vortexed for 10 min at room temperature to resolubilize the protein. Then, 1 μl 1 mg ml^{-1} LysC prepared as per the manufacturer's instructions (VWR) was added to each sample, then allowed to incubate at room temperature for 4 h while gently rocking. Samples were then diluted with freshly prepared 100 mM Tris-HCl, pH 8.0 to reach a final urea concentration of 2 M, after which 2.5 μl 0.4 mg ml^{-1} trypsin (Promega) was added to each sample. Samples were incubated at room temperature overnight while gently rocking. To stop digestion, 40 μl 10% TFA in water was added to each sample, after which samples were centrifuged at 14,000*g*

for 2 min to pellet insoluble material. The resulting supernatant was desalted using Strata-X 33 µm polymeric reversed phase SPE cartridges (Phenomonex). The desalted peptides were dried in a vacuum centrifuge (Thermo Fisher Scientific). Samples were resuspended in 0.2% formic acid in water, then peptide concentrations were determined with a NanoDrop One Microvolume UV-Vis spectrophotometer (Thermo Fisher Scientific), before being vialed and placed into a 5 °C autosampler for mass spectrometry analysis.

Low-input capture Hi-C

Low-input capture Hi-C (liCHi-C) was performed as described[88] on MOLM-13 cells. One million cells were incubated in lysis buffer (10 mM Tris-HCl, pH 8.0, 10 mM NaCl, 0.2% IGEPAL CA-630 and 1× cOmplete EDTA-free protease inhibitor cocktail (Merck, cat. no. 11873580001)) for 30 min on ice to extract nuclei. Nuclei were centrifuged at 1,000*g* for 10 min at 4 °C and washed with ice-cold NEBuffer 2 (New England Biolabs) twice. Nuclei were then incubated in 10% SDS for 30 min at 37 °C, followed by addition of 10 % Triton-X-100 and further incubation for 30 min at 37 °C. Chromatin was digested overnight at 37 °C with HindIII. Cohesive restriction fragment ends were filled in with Klenow polymerase. Ligation of DNA fragments with T4 DNA ligase was performed for 4 h at 16 °C. DNA ligation products were de-crosslinked overnight at 65 °C using Proteinase K. To purify DNA ligation products, phenol-chloroform-isoamyl alcohol (25:24:1 *v*/*v*) purification, followed by ethanol precipitation in the presence of Glycoblue (Thermo Fisher Scientific, cat. no. AM9515) as a co-precipitant were performed. DNA ligation products were resuspended in nuclease-free water and concentration was measured using a Qubit dsDNA HS Assay kit (Thermo Fisher Scientific, cat. no. Q32851). A Covaris M220 focused ultrasonicator was used to sonicate DNA ligation products (20% duty factor, 50 peak incident power, 200 cycles per burst for 65 s). After shearing, DNA ends were repaired and biotinylated informative DNA ligation products were pulled down using Dynabeads MyOne streptavidin C1 magnetic beads (Thermo Fisher Scientific). After washing the ligation products-beads complexes, blunt DNA fragments on the beads were adenine-tailed, washed and resuspended in ligation buffer. PE Illumina adaptors were ligated to the adenine-tailed DNA fragments and amplified over nine cycles of PCR using Phusion high-fidelity PCR master mix with HF buffer (New England Biolabs, cat. no. M0531L). The amplified library was size-selected (300–800 bp) using CleanNGS SPRI beads (CleanNA, cat. no. CNGS-0050). DNA was quantified on an Agilent TapeStation platform using high-sensitivity D1000 ScreenTape system. Enrichment of promoter-containing ligation products was performed using SureSelectXT Target Enrichment System for the Illumina Platform (Agilent Technologies) according to the manufacturer's instructions and the library was amplified over four cycles of PCR using Phusion high-fidelity PCR master mix with HF buffer. The products were purified using CleanNGS SPRI beads and libraries were sequenced using the HiSeq X 150 + 150PE platform.

Genome-wide CRISPR/Cas9 screen analysis

CRISPR/Cas9 screen reads were processed as previously described[20]. In brief, we applied a publicly available Nextflow pipeline[89] available at https://github.com/ZuberLab/crispr-process-nf for trimming (fastx_trimmer from the fastx-toolkit, v.0.0.14), demultiplexing (fastx_barcode_splitter), alignment (Bowtie2, v.2.3.0) and quantification (featureCounts) of the sequenced reads[90,91]. The results were processed with the second Nextflow pipeline applying MAGeCK (v.0.5.9)[92] available at https://github.com/ZuberLab/crispr-mageck-nf. The data were then normalized to a list of proposed essential and non-essential genes[93]. The final steps included subtracting the median of all non-essential genes per log2 fold change (LFC) and dividing this by the difference between the median of all essential genes and the median of all non-essential genes. To scale the values between 0 and −1, we multiplied the outcome by −1. To identify leukaemia-specific genetic dependencies, genes negatively affecting the fitness of CNC cells (defined by $\log_2 FC \leq -0.5$, $n = 2{,}487$) were intersected with genes dispensable for HPC7 cells survival ($\log_2 FC > 0$, $n = 8{,}924$). This analysis led to the identification of 308 genes whose CRISPR inactivation caused a proliferative disadvantage selectively in leukaemia cells.

ATAC-seq analysis

For ATAC-seq, sequenced reads were aligned against the GRCh38 human reference genome using Bowtie2 v.2.2.6. Alignments were filtered for uniquely mapped non-mitochondrial reads and duplicates were removed. Peak calling was carried out using MACS2 v.2.1.0 (ref. 94). We identified ~110,000–180,000 peaks, which showed high consistency between biological duplicates. The union of these peak sets[95] was used to calculate the ATAC-seq coverage over each peak region across all samples. Differentially accessible peaks were identified using DESeq2 (ref. 96) with at least 1.5-fold difference and $P < 0.05$. Peaks were annotated with the R package ChIPseeker[97] and enrichment analysis was performed using the R package rGreat. Sequence motifs for differentially accessible peaks were identified with the MEME Suite[98] and the JASPAR 2022 database[99].

CUT&RUN analysis

ENCODE standards were followed to process sequencing reads with slight modifications for CUT&RUN. Sequencing adaptors were trimmed using Trim Galore! (v.0.6.6). Reads were mapped to the reference genome (GRCh38.p13) using bowtie2 (v.2.3.2) in the–very-sensitive mode and using the argument–dovetail. Low-quality reads, reads overlapping the ENCODE blacklist and duplicate reads were filtered out using SAMtools (v.1.9). Genome-wide coverage was computed using the function bamCoverage from deepTools (v.3.2.1) to obtain BigWig files for visualization purposes. MACS2 (v.2.2.7.1) was used for peak calling in the narrow mode for H3K27ac and broad mode for H3K4me1, using an IgG sample as control, with default parameters. Consensus peaks were computed for each condition using MACS2 with all replicates and their respective IgG samples as control.

CUT&Tag analysis

Raw files underwent preprocessing using prinseq-lite for quality control and filtering. Alignment against the human reference genome (hg38) was conducted using BWA[100] (v.0.7.17-r1188). Post-processing and sorting of aligned reads were performed using SAMtools (v.1.13). The function bamCoverage from deepTools[101] (v.3.5.1) was utilized to generate BigWig files with a binSize of ten, employing counts per million (CPM) for normalization. Peaks were called using macs2 (ref. 94) (v.2.1.0) with the –broad option. Differential ChIP-seq regions were identified using the R package DiffBind, applying DESeq2. Tornado and profile plots were created using deepTools. Read counts per genes were obtained using featureCounts from the subread package. All scatter-plots were generated using ggplot2 in R. Coverage plots were generated with IGV[102].

RNA-seq analysis

Raw sequencing files (FASTQ format) were aligned to the human reference genome (GRCh38) using STAR (v.2.5.1b or 2.7.9a)[103] with default settings. Duplicates were removed using SAMtools v.1.12 (ref. 104). Differential expression analysis was performed using R package DESeq2 (ref. 96). Differentially expressed genes were defined by 1.5 × FC, $P < 0.05$. Analysis of enriched functional categories among detected genes was performed using EnrichR[105], KEGG and the Gene Ontology Consortium (http://www.geneontology.org).

Analysis of P-body-related gene expression

Expression levels of P-body genes ($\log_2$ mRNA) in AML, normal HSPCs and MDS samples were downloaded from Bloodspot (http://www.bloodspot.eu/). The selected probes were DCP1A (218508_at); DCP2

(212919_at); DDX6 (204909_at); EIF4ENIF1 (242291_at), NUFIP2 (224956_at); TNRC6B (213254_at); XRN2 (233878_s_at); and ZFP36L1 (211965_at). The boxplot was generated using the R package ggplot2 (v.3.3.5).

Transcript length and GC content of P-body-enriched genes

We translated the gene Ensembl-IDs to Entrez-Gene IDs with Bioconductor's[106] TxDb.Hsapiens.UCSC.hg38.knownGene and received the respective transcript length via the transcripts function from GenomicFeatures[107]. The GC content per transcript was calculated using the extractTranscriptSeq function from GenomicFeatures and the alphabetFrequency function from Biostrings.

Small RNA-seq analysis

The raw reads were trimmed and annotated by performing SPORTS1.1.2 (parameters, sports.pl -M 1 -a -x GUUCAGAGUUCUACAGUCCGACGAUC -y AAGATCGGAAGAGCACACGTCT -l 15 -L 45 -s) with the pre-compiled human annotation database (hg38).

Pairwise comparison of differentially expressed sncRNAs among different groups was performed using the R package DEseq2 with a threshold of FC > 2 and adjusted $P < 0.05$.

Proteomics analysis

Sample analysis was performed using an UltiMate 3000 RSLCnano LC system (Dionex) coupled to an Orbitrap Eclipse Tribrid mass spectrometer (Thermo Fisher Scientific). Mobile phase A was water with 0.2% formic acid and mobile phase B was 80:20 *v*/*v* ACN:H_2O with 0.2% formic acid. The gradient elution was carried out with a flow rate of 0.300 µl min^{-1}. Then, 1.5 µg peptides were loaded onto a 75-µm i.d. column with 1.7-µm, 130 Å pore size, Bridged Ethylene Hybrid (BEH) C18 particles (Waters Corp.), packed in-house[108] to a length of 30 cm. The column was heated to 50 °C during analysis. For MS analysis, positive mode ionization was used. MS1 scans were acquired from 0 to 90 min every second at a scan range of 300–1,350 *m*/*z*, with a resolution of 240,000 in the Orbitrap and maximum injection time of 50 ms; normalized AGC target (%) was set to 200, equivalent to 8×10^5 ions and RF lens (%) set to 30. Precursor ions were isolated from a 0.50-Da window in the quadrupole; data-dependent HCD MS2 scans with 25% normalized collision energy and a normalized AGC target (%) of 300, equivalent to 3×10^4 ions, were collected in the ion trap from 150–1,350 *m*/*z*, with a maximum injection time of 14 ms and dynamic exclusion period set to 10 s.

Raw proteomic data files were processed by MaxQuant v.2.1.2.02 (ref. 109). The UniProt database of reviewed proteins and isoforms from *Homo sapiens* was retrieved on 17 June 2022. Default MaxQuant parameters were used for processing, along with the following parameters: label-free quantification calculated with a minimum ratio of 1; match between runs enabled; MS/MS not required for label-free quantification comparisons. In the generated MaxQuant data output, protein identifications were removed that were indicated to be identified by site only, corresponded to reverse sequences and/or to potential contaminants by MaxQuant. Protein identifications that generated an intensity value of zero in 50% or more of the analysed samples were also removed. Missing quantitative values among the remaining protein groups were imputed, log_2-transformed and statistically analysed using Argonaut3 (ref. 110). Analysis of enriched functional categories among detected genes was performed using EnrichR[105] and the Gene Ontology Consortium (http://www.geneontology.org).

Polysome profiling analysis

The raw sequence reads were evaluated for quality with FastQC (v.0.11.8) and aligned against the human reference genome (GRCh38) with STAR (v.2.7.9a). The alignments were processed with SAMtools (v.1.13) and reads per gene were counted with featureCounts (v.2.0.3). The normalization and differential gene expression analysis (input shDDX6 versus input shCTRL) was performed with DESeq2 (v.1.22.2). For the differential translation analysis, Xtail (v.1.2.0)[111] was applied with parameters bins = 10,000 and minMeanCount = 20.

For visual representation, logFC values of P-body enriched RNAs were used, as well as log CPM of polysome counts. The function plot, from the graphics package (v.4.1.3), was used for data visualization and the linear model function was used to include the regression line. The cumulative distribution function and the scatter-plot were created using ggplot2 and sm_statCorr from the smplot2 package was used to include the regression line and the Spearman correlation.

ChIP-seq analysis

For the ChIP-seq analysis of KDM5B (GSM1003586)[22], single-end reads were aligned against the hg38 human reference genome using bowtie2 (v.2.4.4-GCC-11.2.0). The aligned reads were filtered using SAMtools (v.1.13-foss-2021b) to remove low-quality and unmapped reads. Duplicates were marked and removed using Picard (v.2.26.3). Peak calling was performed with MACS2 (v.2.2.7.1). Mitochondrial reads and blacklisted regions were also removed.

For the analysis of enhancer and promoter activity in P-body-related genes (H3K27ac levels), a previously published list of P-body genes was obtained[11]. P-body enhancer regions in MOLM-13 cells and normal HSPCs were defined using promoter capture Hi-C data generated from MOLM-13 cells (this study, GSE224858) and CMPs (EGAD00001008828)[88]. Enhancer and promoter activity in AML cells and normal haematopoietic progenitors at P-body genes was determined by quantifying H3K27ac ChIP-seq signal. In brief, paired-end reads for H3K27ac ChIP-seq in MOLM-13 cells (GSM4685439 and GSM4685440) were aligned against the hg38 human reference genome using bowtie2 (v.2.4.4-GCC-11.2.0). The aligned reads were filtered using SAMtools (v.1.13-foss-2021b) to remove low-quality and unmapped reads. Duplicates were marked and removed using Picard (v.2.26.3). BigWig files for H3K27ac ChIP-seq data in $CD34^+$ HSPCs (GSM772885 and GSM772894) were generated from the provided bam files using deepTools (v.3.5.1-foss-2021b) with the option –normalize using RPKM. RPKM signal was obtained with the R package tracklayer (v.1.54.0) and represented as boxplots with the R package ggplot2 (v.3.3.5).

Low-input capture Hi-C analysis

Raw data were processed using HiCUP and the reference human genome (GRCh38.p13). This pipeline removes all experimental artifacts and PCR duplicates and retains only the captured fragments based on the capture design. Interaction scores were calculated using the CHiCAGO R package (v.1.14.0). In brief, this algorithm implements a two-component (biological and technical noise) statistical model, a normalization and multiple-testing correction. The analysis was performed on merged samples after confirming reproducibility between biological replicates using PCA and hierarchical clustering. Significant interactions (CHiCAGO score ≥5) were used for downstream analysis and visualization. The intersection between the significant interactions and ATAC chromatin state (open and closed chromatin) for each condition (shControl and shDDX6) was carried out with the function intersect from the bedtools package (v.2.30.0). The boxplots were conducted with the geom_boxplot function from the ggplot2 package (v.3.3.5).

Statistics and reproducibility

Details for statistical analyses, including replicate numbers, are provided in the figure legends. Statistical analyses were performed using Prism v.9.3.0 software (GraphPad) or R, unless otherwise indicated. Data distribution was assumed to be normal, but this was not formally tested. Mice were allocated randomly into experimental groups. Randomization was not applicable to experiments involving cultured cells. No statistical method was used to pre-determine sample size and no data were excluded from the analyses. The investigators were not blinded to allocation during experiments and outcome assessment unless otherwise specified.

Reporting summary

Further information on research design is available in the Nature Portfolio Reporting Summary linked to this article.

Data availability

RNA-seq, ATAC-seq, eCLIP-seq, polysome profiling, CUT&RUN and CUT&Tag data that support the findings of this study have been deposited in the Gene Expression Omnibus under accession codes GSE260919, GSE224858, GSE261265 and GSE224643. Raw data and the MaxQuant output for the proteomics have been deposited to the MassIVE database under the accession number MSV000090973. Previously published ChIP-seq data and polysome profiling data that were re-analysed here are available under accession code GSM1003586 (ref. 22) and GSE202227 (ref. 76). The human AML data were derived from the TCGA Research Network at http://cancergenome.nih.gov/. All other data supporting the findings of this study are available from the corresponding author on reasonable request. Source data are provided with this paper.

References

77. Pinto do, O. P., Kolterud, A. & Carlsson, L. Expression of the LIM-homeobox gene LH2 generates immortalized steel factor-dependent multipotent hematopoietic precursors. *EMBO J.* **17**, 5744–5756 (1998).
78. Michlits, G. et al. Multilayered VBC score predicts sgRNAs that efficiently generate loss-of-function alleles. *Nat. Methods* **17**, 708–716 (2020).
79. Schmoellerl, J. et al. EVI1 drives leukemogenesis through aberrant ERG activation. *Blood* https://doi.org/10.1182/blood.2022016592 (2022).
80. de Almeida, M. et al. AKIRIN2 controls the nuclear import of proteasomes in vertebrates. *Nature* **599**, 491–496 (2021).
81. Maeda, R. et al. RNA decay in processing bodies is indispensable for adipogenesis. *Cell Death Dis.* **12**, 285 (2021).
82. Chen, B. et al. Dynamic imaging of genomic loci in living human cells by an optimized CRISPR/Cas system. *Cell* **155**, 1479–1491 (2013).
83. Tsanov, N. et al. smiFISH and FISH-quant - a flexible single RNA detection approach with super-resolution capability. *Nucleic Acids Res.* **44**, e165 (2016).
84. Mueller, F. et al. FISH-quant: automatic counting of transcripts in 3D FISH images. *Nat. Methods* **10**, 277–278 (2013).
85. Buenrostro, J. D., Giresi, P. G., Zaba, L. C., Chang, H. Y. & Greenleaf, W. J. Transposition of native chromatin for fast and sensitive epigenomic profiling of open chromatin, DNA-binding proteins and nucleosome position. *Nat. Methods* **10**, 1213–1218 (2013).
86. Blue, S. M. et al. Transcriptome-wide identification of RNA-binding protein binding sites using seCLIP-seq. *Nat. Protoc.* **17**, 1223–1265 (2022).
87. Conway, A. E. et al. Enhanced CLIP uncovers IMP protein-RNA targets in human pluripotent stem cells important for cell adhesion and survival. *Cell Rep.* **15**, 666–679 (2016).
88. Tomas-Daza, L. et al. Low input capture Hi-C (liCHi-C) identifies promoter-enhancer interactions at high-resolution. *Nat. Commun.* **14**, 268 (2023).
89. Di Tommaso, P. et al. Nextflow enables reproducible computational workflows. *Nat. Biotechnol.* **35**, 316–319 (2017).
90. Langmead, B. & Salzberg, S. L. Fast gapped-read alignment with Bowtie 2. *Nat. Methods* **9**, 357–359 (2012).
91. Liao, Y., Smyth, G. K. & Shi, W. featureCounts: an efficient general purpose program for assigning sequence reads to genomic features. *Bioinformatics* **30**, 923–930 (2014).
92. Li, W. et al. MAGeCK enables robust identification of essential genes from genome-scale CRISPR/Cas9 knockout screens. *Genome Biol.* **15**, 554 (2014).
93. Wang, B. et al. Integrative analysis of pooled CRISPR genetic screens using MAGeCKFlute. *Nat. Protoc.* **14**, 756–780 (2019).
94. Zhang, Y. et al. Model-based analysis of ChIP-seq (MACS). *Genome Biol.* **9**, R137 (2008).
95. Li, Q. & Zhang, F. A regression framework for assessing covariate effects on the reproducibility of high-throughput experiments. *Biometrics* **74**, 803–813 (2018).
96. Love, M. I., Huber, W. & Anders, S. Moderated estimation of fold change and dispersion for RNA-seq data with DESeq2. *Genome Biol.* **15**, 550 (2014).
97. Yu, G., Wang, L. G. & He, Q. Y. ChIPseeker: an R/Bioconductor package for ChIP peak annotation, comparison and visualization. *Bioinformatics* **31**, 2382–2383 (2015).
98. Nystrom, S. L. & McKay, D. J. Memes: a motif analysis environment in R using tools from the MEME Suite. *PLoS Comput. Biol.* **17**, e1008991 (2021).
99. Castro-Mondragon, J. A. et al. JASPAR 2022: the 9th release of the open-access database of transcription factor binding profiles. *Nucleic Acids Res.* **50**, D165–D173 (2022).
100. Li, H. & Durbin, R. Fast and accurate short read alignment with Burrows–Wheeler transform. *Bioinformatics* **25**, 1754–1760 (2009).
101. Ramirez, F., Dundar, F., Diehl, S., Gruning, B. A. & Manke, T. deepTools: a flexible platform for exploring deep-sequencing data. *Nucleic Acids Res.* **42**, W187–W191 (2014).
102. Robinson, J. T. et al. Integrative genomics viewer. *Nat. Biotechnol.* **29**, 24–26 (2011).
103. Dobin, A. et al. STAR: ultrafast universal RNA-seq aligner. *Bioinformatics* **29**, 15–21 (2013).
104. Tarasov, A., Vilella, A. J., Cuppen, E., Nijman, I. J. & Prins, P. Sambamba: fast processing of NGS alignment formats. *Bioinformatics* **31**, 2032–2034 (2015).
105. Xie, Z. et al. Gene set knowledge discovery with Enrichr. *Curr. Protoc.* **1**, e90 (2021).
106. Huber, W. et al. Orchestrating high-throughput genomic analysis with Bioconductor. *Nat. Methods* **12**, 115–121 (2015).
107. Lawrence, M. et al. Software for computing and annotating genomic ranges. *PLoS Comput. Biol.* **9**, e1003118 (2013).
108. Shishkova, E., Hebert, A. S., Westphall, M. S. & Coon, J. J. Ultra-high pressure (>30,000 psi) packing of capillary columns enhancing depth of shotgun proteomic analyses. *Anal. Chem.* **90**, 11503–11508 (2018).
109. Cox, J. & Mann, M. MaxQuant enables high peptide identification rates, individualized p.p.b.-range mass accuracies and proteome-wide protein quantification. *Nat. Biotechnol.* **26**, 1367–1372 (2008).
110. Brademan, D. R. et al. Argonaut: a web platform for collaborative multi-omic data visualization and exploration. *Patterns* **1**, 100122 (2020).
111. Xiao, Z., Zou, Q., Liu, Y. & Yang, X. Genome-wide assessment of differential translations with ribosome profiling data. *Nat. Commun.* **7**, 11194 (2016).

Acknowledgements

We thank all members of the Sardina, Grebien and Di Stefano groups for stimulating scientific discussions. We thank S. Doulatov for the human iPS cell-derived CD34$^+$ cells, D. Lacorazza for the THP-1 cells, D. Nakada for the MOLM-13-Cas9 cells, L. Brunetti for advice on generating the DDX6 degron AML cells, J. Yustein and M. Mamonkin for the NSG mice, M. Fabian for the LSM14 mutant plasmids, F. Stossi and A. Tostado of the BCM Integrated Microscopy Core for help with the smFISH experiments, the BCM GEMC for the generation of *Ddx6* transgenic mice and Z. Ianniello for help with polysome profiling experiments. B.D.S. is a Cancer Prevention and Research Institute of Texas (CPRIT) Scholar in Cancer Research. B.D.S. is supported by the

CPRIT Recruitment of First-Time, Tenure-Track Faculty Member Award RR200079, the American Society of Hematology Scholar Award, the B+ Foundation, the Worldwide Cancer Research Foundation, the Milky Way Research Foundation Investigator Award, the Nancy Chang, PhD Award for Research Excellence and the National Institutes of Health (NIH) MIRA award 1R35GM147126-01. S.K. is supported by NIH 5T32DK060445-19 and NIH 1F32CA288043-01. Research in the F.G. laboratory was supported by the European Union's Horizon 2020 research and innovation programme (Marie Sklodowska-Curie grant agreement no. 813091) and the Austrian Science Fund (projects P-35628, P35298 to F.G.). Research in the J.L.S. laboratory was funded by Worldwide Cancer Research (20-0269) and the grant PID2019-111243RA-I00 funded by MICIU/AEI/10.13039/501100011033. J.L.S. is supported by Instituto de Salud Carlos III (CP19/00176). Research in the B.M.J. laboratory was supported by grant PID2021-125277OB-I00 funded by MICIU/AEI/10.13039/501100011033 and FEDER/EU. B.M.J. is supported by Instituto de Salud Carlos III (CP22/00127). We thank CERCA Programme/Generalitat de Catalunya for institutional support. E.V.N. is a CPRIT Scholar in Cancer Research (RR200040). This project was supported by the Cytometry and Cell Sorting Core at Baylor College of Medicine with funding from the CPRIT Core Facility Support Award (CPRIT-RP180672), the NIH (CA125123 and RR024574) and the assistance of J. M. Sederstrom. We are grateful for support on this project from NIH grant P41 GM108538 (National Center for Quantitative Biology of Complex Systems) to J.J.C.

Author contributions

S.K., L.P., F.G. and B.D.S. conceived the study and wrote the manuscript with input from J.L.S.; S.K., L.P., N.L., P.P., T.E., Y.C., C.S., B.A. and G.M. performed experiments and analysed the data; A.V.L., G.V. and J.L.S. performed and analysed the AML patient-derived xenograft and primary CD34$^+$ experiments; A.P.-R., L.T.-D. and B.M.J. performed liHi-C and CUT&RUN experiments in collaboration with G.V., A.V.L. and J.L.S.; J.S. and Q.C. performed and analysed the small RNA-seq experiments; A.J., E.S. and J.C. performed and analysed the proteomic data; A.S., M.B. and E.V.N. performed and analysed the eCLIP-seq; A.M., T.V. and P.M. helped with the AML patient-derived xenograft and the primary CD34$^+$ experiments; A.F. supervised the polysome profiling experiments; I.M.M. and K.K. helped with HPC7 experiments; R.R. helped with the primary patient AML and CD34$^+$ cells.

Competing interests

E.V.N. is co-founder, member of the Board of Directors, on the SAB, equity holder and paid consultant for Eclipse BioInnovations, on the SAB of RNAConnect and is inventor of intellectual property owned by University of California San Diego. The interests of E.V.N. have been reviewed and approved by the Baylor College of Medicine in accordance with its conflict of interest policies. P.M. is a co-founder, member of the Board of Directors, equity holder and paid consultant for OneChain Immunotherapeutics (Barcelona, Spain). This work has no connection with and is not related to the scientific interests of OneChain Immunotherapeutics. J.J.C. is a consultant for Thermo Fisher Scientific, 908 Devices and Seer. The remaining authors declare no competing interests.

Additional information

Extended data is available for this paper at https://doi.org/10.1038/s41556-024-01489-6.

Supplementary information The online version contains supplementary material available at https://doi.org/10.1038/s41556-024-01489-6.

Correspondence and requests for materials should be addressed to Jose L. Sardina, Florian Grebien or Bruno Di Stefano.

Peer review information *Nature Cell Biology* thanks Anthony Khong and the other, anonymous, reviewer(s) for their contribution to the peer review of this work. Peer reviewer reports are available.

https://doi.org/10.1038/s41556-024-01489-6

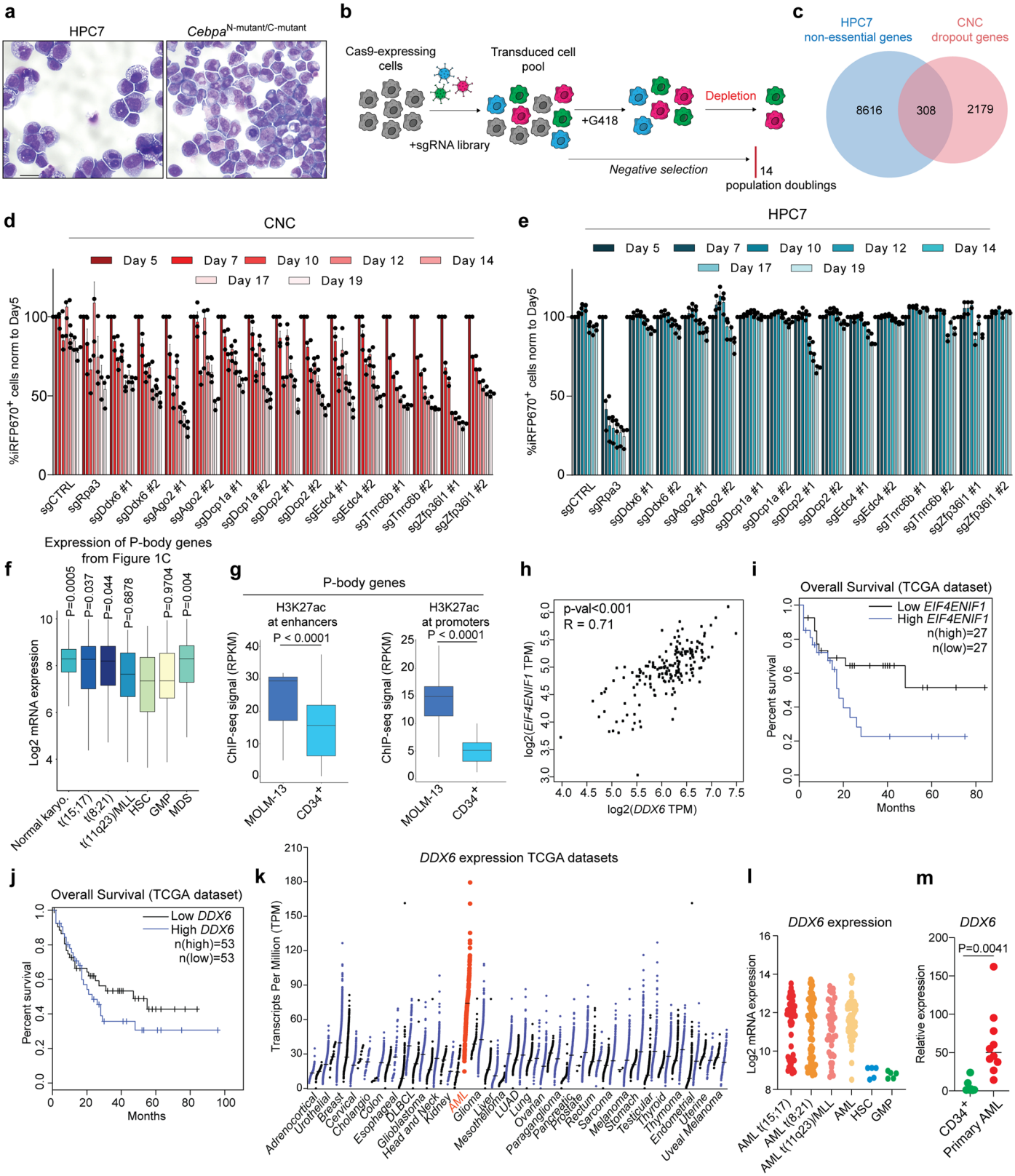

Extended Data Fig. 1 | See next page for caption.

https://doi.org/10.1038/s41556-024-01489-6

Extended Data Fig. 1 | CRISPR screens identify P-body regulators as a selective dependency in AML. (a) Cytospins of HPC7 and *Cebpa*$^{N\text{-}mutant/C\text{-}mutant}$ (CNC) cells. $n = 3$ independent experiments. **(b)** Schematic illustration of pooled genome-wide CRISPR/Cas9 dropout screening strategy. **(c)** Venn diagram showing filtering strategy for the identification of 308 leukaemia-specific genetic dependencies shown in Fig. 1a. **(d, e)** Competition-based proliferation assay in (d) CNC Cas9 cells or (e) HPC7 Cas9 cells, illustrated as colour-coded percentage of iRFP670^{+} cells transduced with indicated sgRNAs over 19 d. The non-targeting sgCTRL is used as a negative control, sgRpa3, targeting essential gene *Rpa3*, is used as a positive control. Results are normalized to day 5 post-infection. Two-way ANOVA with Dunnett's post-hoc test, $n = 3$ biological replicates per group, mean ± s.e.m. **(f)** Boxplots showing the expression levels (log2 mRNA) of P-body related genes (displayed in Fig. 1c) in AML, normal HSPCs, and MDS samples. AML normal karyotype ($n = 28$), AML t(15;17) ($n = 28$), AML t(8;21) ($n = 28$), AML t(11q23)/MLL ($n = 28$), HSC (haematopoietic stem cell) ($n = 6$), GMP (granulocyte monocyte progenitor) (n = 7), MDS (myelodysplastic syndromes) ($n = 28$). Box centre line indicates median, box limits indicate upper (Q3) and lower quartiles (Q1), lower whisker is Q1 − 1.5 × interquartile range (IQR) and upper whisker is Q3 + 1.5 × IQR. Two-tailed t-test with Welch's correction. **(g)** Boxplots showing normalized H3K27ac ChIP-seq signal (RPKM) in MOLM-13 cells (GSM4685439 and GSM4685440) and CD34+ HSPCs at enhancers ($n = 26$ per group) (left panel) and promoter ($n = 214$ per group) (right panel) regions (GSM772885 and GSM772894) of P-body genes. Box centre line indicates median, box limits indicate upper (Q3) and lower quartiles (Q1), lower whisker is Q1 − 1.5 × IQR and upper whisker is Q3 + 1.5 × IQR. Two-tailed t-test with Welch's correction. **(h)** Significant correlation between the expression of *DDX6* and *EIF4ENIF1* in the TCGA-LAML dataset. Pearson's correlation coefficients and corresponding p-values (two-tailed one-sample Student's t-test) are indicated. **(i, j)** Kaplan–Meier survival analysis plots of TCGA data for AML patients with low vs high expression of (i) *EIF4ENIF1* ($n = 27$ patients per group) or (j) DDX6 ($n = 53$ patients per group). **(k)** *DDX6* mRNA expression in AML (red) compared to other cancers, based on data from TCGA database. Data are presented as mean log2 expression with range. Black dots: expression levels in normal cells; Blue dots: expression levels in cancer cells. **(l)** *DDX6* expression in AML patient samples compared to normal HSPCs. AML: $n = 48$, AML t(15;17): $n = 54$, AML inv(16)/t(16;16): $n = 47$, AML t(8;21): $n = 60$, AML t(11q23)/MLL: $n = 43$ patients. HSC (haematopoietic stem cell): $n = 6$, GMP (granulocyte monocyte progenitor): $n = 7$ healthy individuals (BloodSpot data of *DDX6* probe 204909_at). Unpaired two-tailed Student's t-test. **(m)** qRT–PCR for DDX6 in human primary CD34^{+} cells ($n = 7$ healthy individuals) and AML patient cells ($n = 10$ patients). Unpaired two-tailed Student's t-test, mean.

https://doi.org/10.1038/s41556-024-01489-6

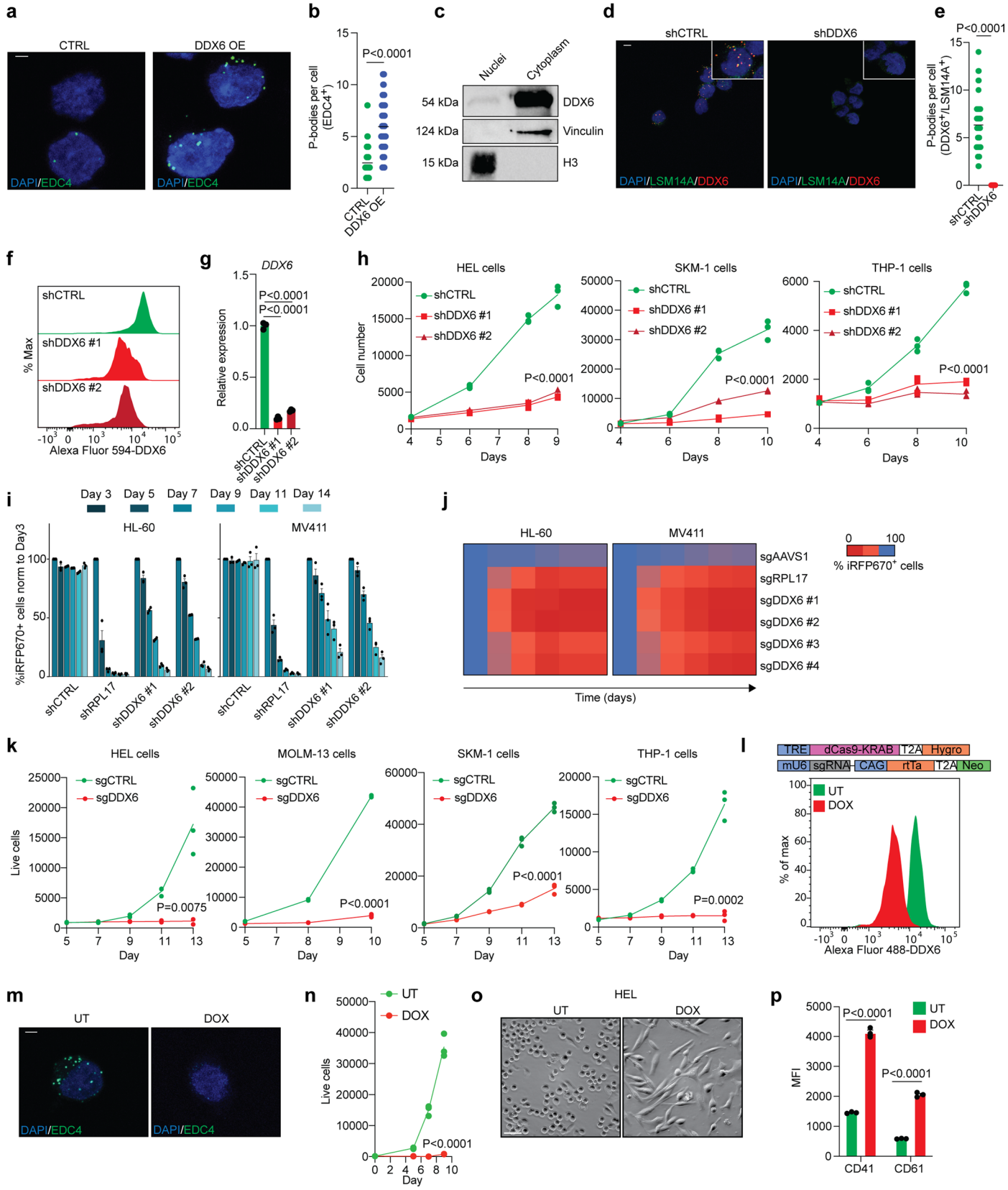

Extended Data Fig. 2 | See next page for caption.

https://doi.org/10.1038/s41556-024-01489-6

Extended Data Fig. 2 | DDX6 is essential for AML cell proliferation and survival *in vitro*. **(a)** Representative IF imaging of EDC4 punctae (green) in control and *DDX6* overexpressing HPC7 cells. Nuclei were counterstained with DAPI (blue). Scale: 2.5 µm. **(b)** Quantification of EDC4 punctae in HPC7 cells overexpressing DDX6 by IF. n = 45-55 cells per group, unpaired two-tailed Student's t-test, mean ± s.e.m. **(c)** Representative Western blot image of DDX6 in the nuclear and cytoplasmic fractions of MOLM-13 cells. n = 3 independent experiments. **(d)** Representative IF imaging of LSM14A (green) and DDX6 (red) punctae in control and *DDX6* KD MOLM-13 cells. Nuclei were counterstained with DAPI. Scale: 10 µm. **(e)** Quantification of LSM14A$^+$DDX6$^+$ punctae in control and *DDX6* KD MOLM-13 cells by IF. Unpaired two-tailed Student's t-test, n = 24–30 cells per group, mean ± s.e.m. **(f)** Representative intracellular flow cytometry plots showing DDX6 levels in shCTRL and shDDX6 MOLM-13 cells. **(g)** qRT–PCR validation of *DDX6* KD in MOLM-13 cells. Unpaired two-tailed Student's t-test, n = 3 biologically independent samples per group, mean ± s.e.m. **(h)** Proliferation assay for shCTRL and shDDX6 AML cell lines at the indicated time points after transduction. Two-way ANOVA with Dunnett's post-hoc test, n = 3 biological replicates per group, mean ± s.e.m. **(i)** Competition-based proliferation assays upon *DDX6* knockdown performed in indicated cell lines. shRPL17, targeting the essential gene *RPL17*, is used as a positive control. Two-way ANOVA with Dunnett's post-hoc test, n = 3 biologically independent samples per group, mean ± s.e.m. **(j)** Heatmap summarizing the competition-based proliferation assays upon *DDX6* knockout in indicated Cas9-expressing cell lines. Data are illustrated as colour-coded percentage of iRFP670$^+$ cells transduced with indicated sgRNAs over 17 d. sgAAVS1 is used as negative control, sgRPL17 is used as positive control. Results are normalized to day 3 post-infection, (n = 3 biologically independent samples per group, mean). **(k)** Proliferation assay for CTRL and *DDX6* KO human AML cell lines at the indicated time points after transduction. Unpaired two-tailed Student's t-test, n = 3 biologically independent samples per group, mean ± s.e.m. **(l)** Schematic of dCas9-KRAB and sgRNA vectors (upper panel). Representative intracellular flow cytometry plots for DDX6 in CRISPRi HEL cells, either untreated (UT) or treated with doxycycline (DOX) for 7 d (lower panel). **(m)** Representative IF imaging of EDC4 punctae (green) in CRISPRi HEL cells, either untreated (UT) or treated with doxycycline (DOX) for 4 d. Nuclei were counterstained with DAPI (blue). Scale: 2.5 µm. **(n)** Proliferation assay for UT or DOX-treated CRISPRi HEL cells at the indicated time points after transduction. Unpaired two-tailed Student's t-test, n = 3 biologically independent samples per group, mean ± s.e.m. **(o)** Representative images of UT or DOX-treated CRISPRi HEL cells. Scale: 10 µm. **(p)** Megakaryocytic differentiation in CRISPRi HEL cells 7 d after DDX6 silencing was quantified by flow cytometry, using CD41 and CD61 as markers. Unpaired two-tailed Student's t-test, n = 3 biologically independent samples per group, mean ± s.e.m.

https://doi.org/10.1038/s41556-024-01489-6

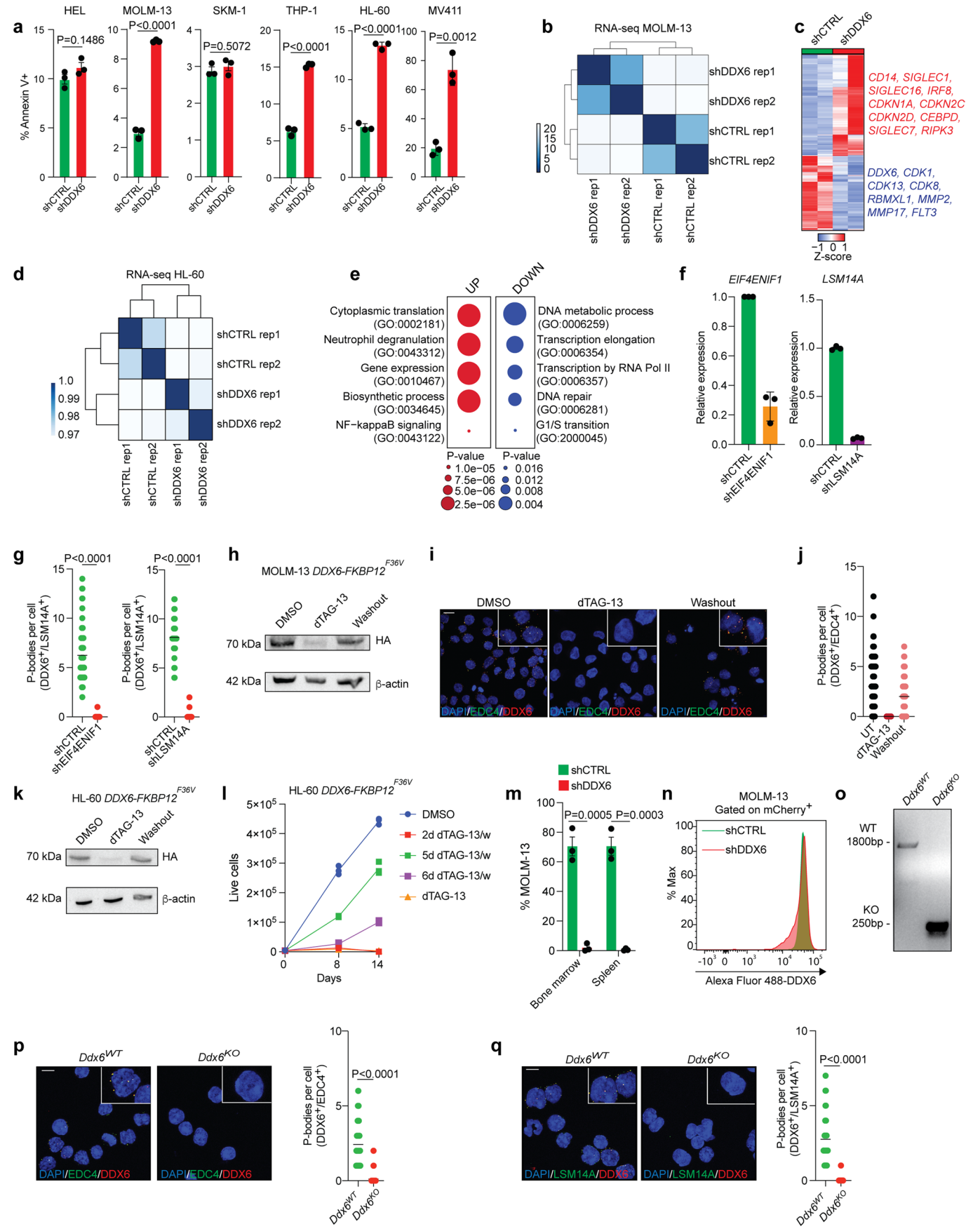

Extended Data Fig. 3 | See next page for caption.

https://doi.org/10.1038/s41556-024-01489-6

Extended Data Fig. 3 | DDX6 is essential for the proliferation and gene expression programme of AML cells. (a) Flow cytometric analysis of cell death (Annexin V$^+$) in shCTRL and shDDX6 AML cell lines. Unpaired two-tailed Student's *t*-test, $n = 3$ biologically independent samples per group, mean ± s.e.m. **(b)** Correlation heatmap showing the correlation (r) values between MOLM-13 RNA-seq samples. Scale bar represents the range of the correlation coefficients (r) displayed. **(c)** Heatmap of RNA-seq data for shCTRL and shDDX6 HL-60 cells ($n = 2$, FC > 1.5; $p < 0.05$). Upregulated genes are depicted in red, while in blue are downregulated genes. **(d)** Correlation heatmap showing the correlation (r) values between HL-60 RNA-seq samples. Scale bar represents the range of the correlation coefficients (r) displayed. **(e)** GO enrichment analysis of differentially expressed genes in control vs. *DDX6* KD HL-60 cells. **(f)** qRT–PCR validation of (left) *EIF4ENIF1* KD and (right) *LSM14A* KD in MOLM-13 cells. Unpaired two-tailed Student's t-test, $n = 3$ biologically independent samples per group, mean ± s.e.m. **(g)** Quantification of LSM14A$^+$DDX6$^+$ punctae in control and (left) *EIF4ENIF1* KD or (right) *LSM14A* KD MOLM-13 cells by IF. Unpaired two-tailed Student's t-test, $n = 17$-31 cells per group, mean ± s.e.m. **(h)** Representative Western blot showing HA-tagged endogenous DDX6 protein levels in DDX6-FKBP12^{F36V} MOLM-13 cells after 2 d of dTAG-13 treatment, followed by washout and culture for 5 d. $n = 3$ independent experiments. **(i)** Representative IF imaging of EDC4 punctae (green) and DDX6 punctae (red) in DDX6-FKBP12^{F36V} MOLM-13 cells after 2 d of dTAG-13 treatment, followed by washout and culture for 5 d. Nuclei were counterstained with DAPI (blue). Scale: 10 µm. **(j)** Quantification of EDC4$^+$DDX6$^+$ punctae in the indicated cells by IF ($n = 47$-87 cells per group, mean ± s.e.m.). **(k)** Representative Western blot showing HA-tagged endogenous DDX6 protein levels in DDX6-FKBP12^{F36V} HL-60 cells after 2 d of dTAG-13 treatment, followed by washout and culture for 5 d. $n = 3$ independent experiments. **(l)** Proliferation of DDX6-FKBP12^{F36V} HL-60 cells, either untreated (UT), continuously treated with dTAG-13, or treated with dTAG-13 for 2, 5, or 6 days, followed by washout and culture ($n = 3$ biological replicates per group, mean ± s.e.m.). **(m)** Percentages of control or *DDX6* KD MOLM-13 cells in the bone marrow and spleens of NSG mice (25 d post-transplant) quantified by flow cytometry. Unpaired two-tailed Student's t-test, $n = 3$ mice per group, mean ± s.e.m. **(n)** Representative intracellular flow cytometry plot for DDX6 in shCTRL and shDDX6 MOLM-13 cells in the bone marrow of NSG mice (45 d post-transplant). **(o)** Genotyping PCR demonstrating poly(I:C)-induced *Ddx6* deletion in c-Kit$^+$ haematopoietic progenitor cells isolated from the bone marrow of *Mx1-Cre/Ddx6*$^{fl/fl}$ mice. $n = 3$ independent experiments. **(p)** Left: Representative IF imaging of EDC4 punctae (green) and DDX6 punctae (red) in *Ddx6*^{WT} and *Ddx6*^{KO} c-Kit$^+$ haematopoietic progenitor cells. Nuclei were counterstained with DAPI (blue), scale: 10 µm. Right: Quantification of EDC4$^+$DDX6$^+$ punctae by IF in *Ddx6*^{WT} and *Ddx6*^{KO} c-Kit$^+$ haematopoietic progenitor cells. Unpaired two-tailed Student's t-test, $n = 60$-63 cells per group, mean ± s.e.m. **(q)** Left: Representative IF imaging of LSM14A punctae (green) and DDX6 punctae (red) in *Ddx6*^{WT} and *Ddx6*^{KO} c-Kit$^+$ haematopoietic progenitor cells. Nuclei were counterstained with DAPI (blue), scale: 10 µm. Right: Quantification of LSM14A$^+$DDX6$^+$ punctae by IF in *Ddx6*^{WT} and *Ddx6*^{KO} c-Kit$^+$ haematopoietic progenitor cells. Unpaired two-tailed Student's t-test, $n = 32$-33 cells per group, mean ± s.e.m.

https://doi.org/10.1038/s41556-024-01489-6

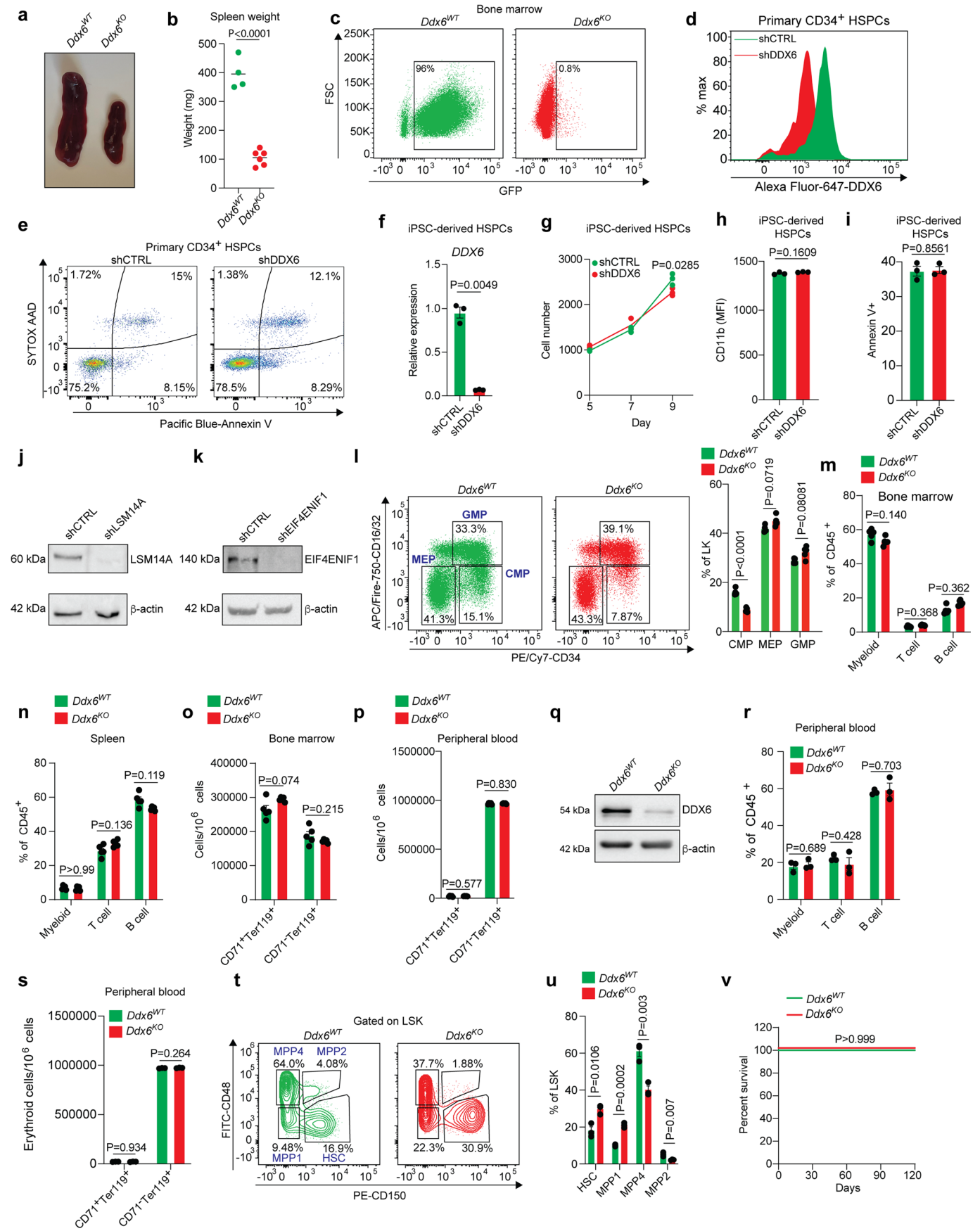

Extended Data Fig. 4 | See next page for caption.

https://doi.org/10.1038/s41556-024-01489-6

Extended Data Fig. 4 | DDX6 loss has little effect on steady-state haematopoiesis. (a) Representative image of spleens from mice 90 d after transplantation with MLL-AF9-transduced *Ddx6*^{WT} and *Ddx6*^{KO} c-Kit^{+} cells. **(b)** Weights of spleens isolated from mice 90 days after transplantation with MLL-AF9-transduced *Ddx6*^{WT} and *Ddx6*^{KO} c-Kit^{+} cells. Unpaired two-tailed Student's t-test, *Ddx6*^{WT} $n = 4$ mice, *Ddx6*^{KO} $n = 6$ mice, mean ± s.e.m. **(c)** Representative flow cytometry plots of leukaemia (GFP^{+}) cells in bone marrow from mice 90 d after transplantation with MLL-AF9-transduced *Ddx6*^{WT} and *Ddx6*^{KO} c-Kit^{+} cells. **(d)** Representative intracellular flow cytometry plot for DDX6 in shCTRL and shDDX6 primary bone marrow human CD34^{+} cells. **(e)** Representative flow cytometry plots showing cell death (Annexin V^{+}/Sytox AAD^{+}) in shCTRL and shDDX6 primary human CD34^{+} cells. **(f)** qRT–PCR analysis to validate *DDX6* KD in human iPSC-derived CD34^{+} HSPCs. Unpaired two-tailed t-test with Welch's correction, $n = 3$ biologically independent samples per group, mean ± s.e.m. **(g)** Proliferation assay for shCTRL and shDDX6 human iPSC-derived HSPCs at the indicated timepoints after transduction. Unpaired two-tailed Student's t-test, $n = 3$ biologically independent samples per group, mean ± s.e.m. **(h)** Flow cytometric analysis for myeloid differentiation (CD11b median fluorescence intensity (MFI)) in shCTRL vs shDDX6 human iPSC-derived HSPCs. Unpaired two-tailed Student's t-test, $n = 3$ biologically independent samples per group. **(i)** Flow cytometric analysis of cell death (Annexin V^{+}) in human iPSC-derived HPCs. Unpaired two-tailed Student's t-test, $n = 3$ biologically independent samples per group, mean ± s.e.m. **(j, k)** Representative Western blots validating (j) *LSM14A* KD and (k) *EIF4ENIF1* KD in primary human CD34^{+} cells. $n = 3$ independent experiments. **(l)** Representative flow cytometry plots and quantification for CMP, GMP, and MEP populations (gated on LK cells) in the bone marrow of *Mx1-Cre* and *Mx1-Cre/Ddx6*$^{fl/fl}$ mice 110 d after *Ddx6* deletion. Unpaired two-tailed Student's t-test, *Ddx6*^{WT} $n = 5$ mice, *Ddx6*^{KO} $n = 5$ mice, mean ± s.e.m. **(m, n)** Quantification of myeloid cells, T cells, and B cells as a percentage of CD45^{+} cells in the (m) bone marrow and (n) spleens of *Mx1-Cre* and *Mx1-Cre/Ddx6*$^{fl/fl}$ mice 110 d after *Ddx6* deletion. Unpaired two-tailed Student's t-test, *Ddx6*^{WT} $n = 5$ mice, *Ddx6*^{KO} $n = 5$ mice, mean ± s.e.m. **(o, p)** Frequency of erythroid cells in the (o) bone marrow and (p) peripheral blood *Mx1-Cre* and *Mx1-Cre/Ddx6*$^{fl/fl}$ mice 110 d after *Ddx6* deletion. Unpaired two-tailed Student's t-test, *Ddx6*^{WT} $n = 5$ mice, *Ddx6*^{KO} $n = 5$ mice, mean ± s.e.m. **(q)** Representative Western blot analysis for DDX6 in bone marrow cells of *Rosa26-Cre* and *Rosa26-Cre/Ddx6*$^{fl/fl}$ mice. $n = 3$ independent experiments. **(r)** Quantification of myeloid cells, T cells, and B cells as a percentage of CD45^{+} cells in the peripheral blood of *Rosa26-Cre-ERT2* and *Rosa26-Cre-ERT2/Ddx6*$^{fl/fl}$ mice 80 d after tamoxifen treatment. Unpaired two-tailed Student's t-test, *Ddx6*^{WT} $n = 3$ mice, *Ddx6*^{KO} $n = 3$ mice, mean ± s.e.m. **(s)** Frequency of erythroid cells in the peripheral blood of *Rosa26-Cre-ERT2* and *Rosa26-Cre-ERT2/Ddx6*$^{fl/fl}$ mice 80 d after tamoxifen treatment. Unpaired two-tailed Student's t-test, *Ddx6*^{WT} $n = 3$ mice, *Ddx6*^{KO} $n = 3$ mice, mean ± s.e.m. **(t)** Representative flow cytometry plots showing percentages of HSC, MPP1, MPP2, and MPP4 populations, gated on LSK cells, in the bone marrow of *Rosa26-Cre-ERT2* and *Rosa26-Cre-ERT2/Ddx6*$^{fl/fl}$ mice after *Ddx6* deletion. **(u)** Quantification of HSC, MPP1, MPP2, and MPP4 populations, as a percentage of LSK cells, in the bone marrow of *Rosa26-Cre-ERT2* and *Rosa26-Cre-ERT2/Ddx6*$^{fl/fl}$ mice after *Ddx6* deletion. Unpaired two-tailed Student's t-test, *Ddx6*^{WT} $n = 5$ mice, *Ddx6*^{KO} $n = 5$ mice, mean ± s.e.m. **(v)** Kaplan–Meier survival curves of *Rosa26-Cre-ERT2* and *Rosa26-Cre-ERT2/Ddx6*$^{fl/fl}$ mice 4 months after tamoxifen treatment. Mantel–Cox test, *Ddx6*^{WT} $n = 3$ mice, *Ddx6*^{KO} $n = 3$ mice.

https://doi.org/10.1038/s41556-024-01489-6

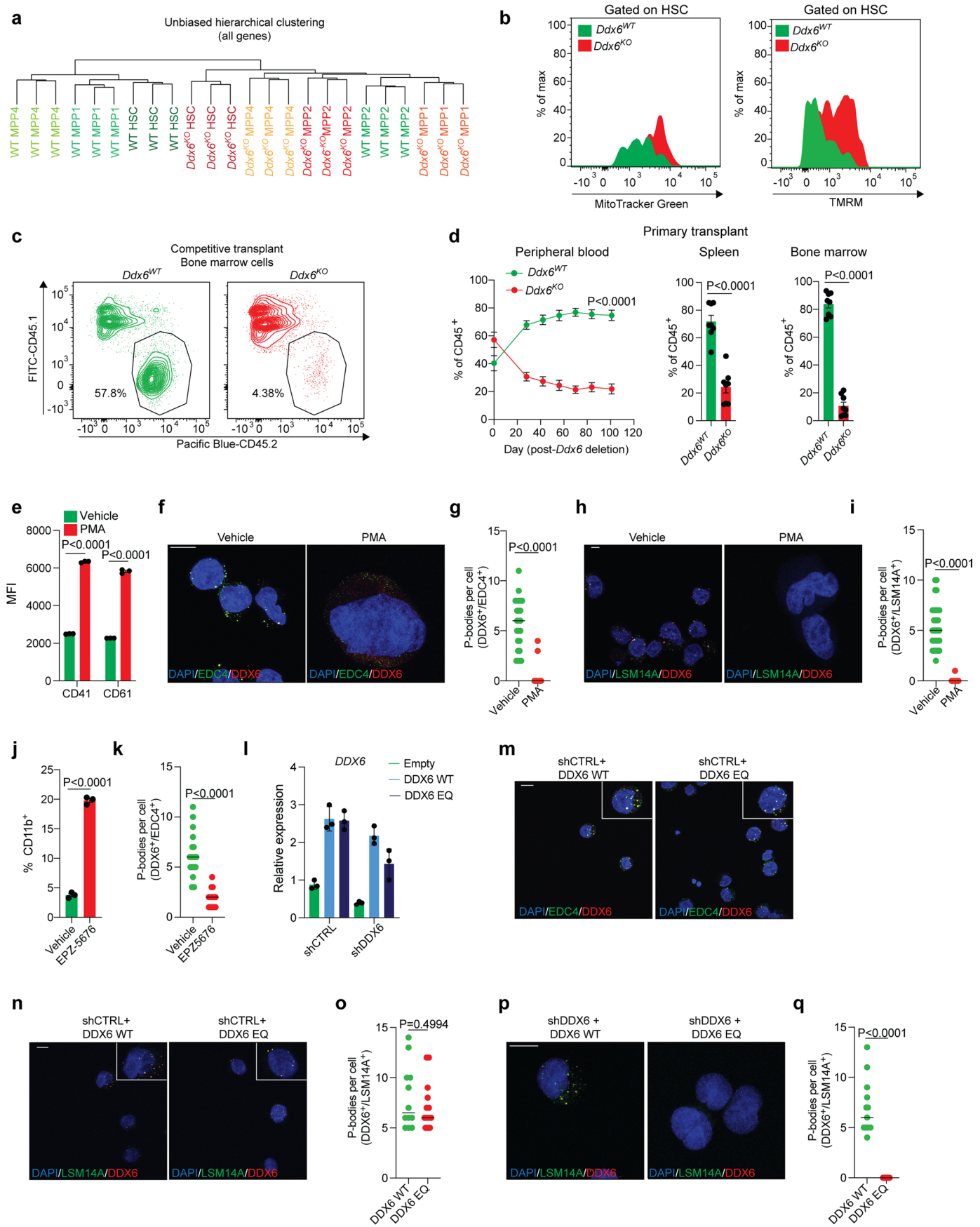

Extended Data Fig. 5 | See next page for caption.

https://doi.org/10.1038/s41556-024-01489-6

Extended Data Fig. 5 | DDX6 regulates HSC quiescence and response to stress. **(a)** Unsupervised clustering of *Ddx6*^{WT} and *Ddx6*^{KO} HSC, MPP1, MPP2, and MPP4 populations subjected to RNA-seq. **(b)** Representative flow cytometry plots of (left) MitoTracker Green FM and (right) TMRM staining in *Ddx6*^{WT} and *Ddx6*^{KO} HSCs, 24 d after *Ddx6* deletion. **(c)** Representative flow cytometry plots of *Ddx6*^{WT} and *Ddx6*^{KO} chimerism within the donor haematopoietic compartment (CD45^{+}) in the bone marrow 187 d after primary competitive transplantation. **(d)** HSCs sorted from CD45.1 and *Mx1-Cre/Ddx6*$^{fl/fl}$ mice were competitively transplanted into lethally irradiated WT recipient mice, followed by poly(I:C) treatment 34 d later. Quantification is shown of *Ddx6*^{WT} and *Ddx6*^{KO} chimerism within the donor haematopoietic compartment (CD45^{+}) in peripheral blood, spleen, or bone marrow, at the indicated timepoints after *Ddx6* deletion. *Ddx6*^{WT} $n = 8$ mice, *Ddx6*^{KO} $n = 8$ mice, two-way ANOVA with Bonferroni's multiple comparisons test, mean ± s.e.m. **(e)** Flow cytometric analysis for the megakaryocytic differentiation markers CD41 and CD61 in HEL cells 4 d after vehicle (DMSO) or PMA treatment. Unpaired two-tailed Student's t-test, $n = 3$ biologically independent samples per group, mean ± s.e.m. **(f)** Representative IF imaging of EDC4 punctae (green) and DDX6 punctae (red) in vehicle-treated and PMA-treated HEL cells. Nuclei were counterstained with DAPI (blue). Scale: 10 µm. **(g)** Quantification of EDC4^{+}DDX6^{+} punctae in vehicle-treated and PMA-treated HEL cells by IF. Unpaired two-tailed Student's t-test, $n = 24$-26 cells per group, mean ± s.e.m. **(h)** Representative IF imaging of LSM14A punctae (green) and DDX6 punctae (red) in vehicle-treated and PMA-treated HEL cells. Nuclei were counterstained with DAPI (blue). Scale: 10 µm. **(i)** Quantification of LSM14A^{+}DDX6^{+} punctae in vehicle-treated and PMA-treated HEL cells by IF. Unpaired two-tailed Student's t-test, $n = 25$-33 cells per group, mean ± s.e.m. **(j)** Flow cytometric analysis for myeloid differentiation (% CD11b^{+}) in MOLM-13 cells 5 d after treatment with the anti-leukaemic drug EPZ-5676. Unpaired two-tailed Student's t-test, $n = 3$ biologically independent samples per group, mean ± s.e.m. **(k)** P-body numbers (EDC4^{+}DDX6^{+} punctae) in MOLM-13 cells treated with EPZ-5676. Unpaired two-tailed Student's t-test, $n = 26$-30 cells per group. **(l)** qRT–PCR analysis of DDX6 expression in *DDX6* KD MOLM-13 cells rescued with DDX6 WT or DDX6 EQ. $n = 3$ biologically independent samples per group, mean ± s.e.m. **(m)** Representative IF imaging of EDC4 punctae (green) and DDX6 punctae (red) in shCTRL MOLM-13 cells with exogenous DDX6 WT and EQ expression. Nuclei were counterstained with DAPI (blue). Scale: 10 µm. **(n)** Representative IF imaging of LSM14A punctae (green) and DDX6 punctae (red) in shCTRL MOLM-13 cells with exogenous DDX6 WT and EQ expression. Nuclei were counterstained with DAPI (blue). **(o)** Quantification of LSM14A^{+}DDX6^{+} punctae in shCTRL MOLM-13 cells by IF. Unpaired two-tailed Student's t-test, $n = 12$-13 cells per group, mean ± s.e.m. **(p)** Representative IF imaging of LSM14A punctae (green) and DDX6 punctae (red) in shDDX6 MOLM-13 cells with exogenous DDX6 WT and EQ expression. Nuclei were counterstained with DAPI (blue). Scale: 10 µm. **(q)** Quantification of LSM14A^{+}DDX6^{+} punctae in shCTRL MOLM-13 cells by IF. Unpaired two-tailed Student's t-test, $n = 13$-33 cells per group, mean ± s.e.m.

https://doi.org/10.1038/s41556-024-01489-6

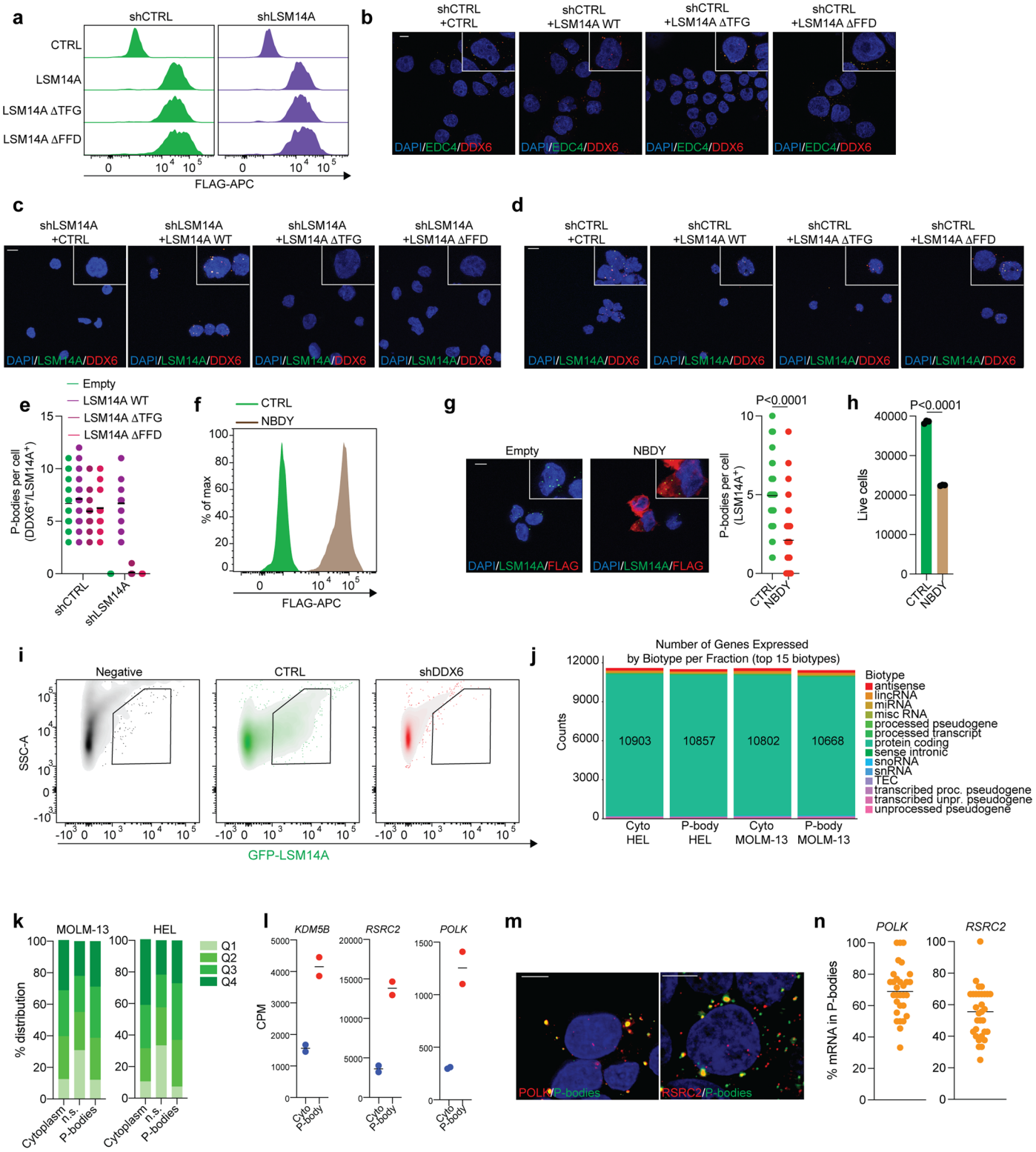

Extended Data Fig. 6 | See next page for caption.

https://doi.org/10.1038/s41556-024-01489-6

Extended Data Fig. 6 | Disrupting P-body assembly abrogates AML cell proliferation. **(a)** Representative intracellular flow cytometry plots showing expression of FLAG-LSM14A WT, FLAG-LSM14A ΔTFG, or FLAG-LSM14A ΔFFD in control and *LSM14A* KD HEL cells. **(b)** Representative IF imaging of EDC4 punctae (green) and DDX6 punctae (red) in control HEL cells expressing LSM14A WT, LSM14A ΔTFG, or LSM14A ΔFFD. Nuclei were counterstained with DAPI (blue). **(c, d)** Representative IF imaging of LSM14A punctae (green) and DDX6 punctae (red) in (c) *LSM14A* KD and (d) control HEL cells expressing LSM14A WT, LSM14A ΔTFG, or LSM14A ΔFFD. Nuclei were counterstained with DAPI (blue). Scale: 10 µm. **(e)** Quantification of LSM14A$^+$DDX6$^+$ punctae in the indicated cells by IF. One-way ANOVA with Dunnett's post-hoc test, n = 16-29 cells per group, mean ± s.e.m. **(f)** Representative intracellular flow cytometry plot showing NBDY expression (FLAG) in MOLM-13 cells. **(g)** Left: Representative IF imaging of LSM14A punctae (green) and FLAG (red) in control and NBDY-expressing MOLM-13 cells, scale: 10 µm. Right: quantification of LSM14A$^+$DDX6$^+$ punctae in control and NBDY-expressing MOLM-13 cells by IF. Unpaired two-tailed Student's t-test, n = 24 cells per group, mean ± s.e.m. **(h)** HEL cell numbers 13 d after forced expression of NBDY. Unpaired two-tailed Student's t-test, n = 3 biologically independent samples per group, mean ± s.e.m. **(i)** Representative flow cytometry plots showing loss of GFP-LSM14A$^+$ P-bodies after *DDX6* silencing. **(j)** Distribution of RNA biotypes within the P-bodies and cytoplasm of HEL and MOLM-13 cells. **(k)** Distribution of P-body-enriched, cytoplasm-enriched, and non-enriched genes within each expression quartile, which range from Q1 (low expression) to Q4 (high expression). **(l)** RNA-seq analysis showing counts per million (CPM) values for the indicated transcripts in the cytoplasm and P-bodies of MOLM-13 cells (n = 2 biologically independent samples per group, mean). **(m)** Representative smFISH images of (left) *POLK* or (right) *RSRC2* mRNA molecules (red) and GFP-LSM14A$^+$ punctae (green). Nuclei were counterstained with DAPI (blue). Scale: 5 µm **(n)** Quantification of the fraction of *POLK* or *RSCR2* transcripts colocalizing with GFP-LSM14A$^+$ punctae in individual cells (*KDM5B*: n = 30 cells, mean = 69.53%, *RSRC2*: n = 31 cells, mean = 55.05%).

https://doi.org/10.1038/s41556-024-01489-6

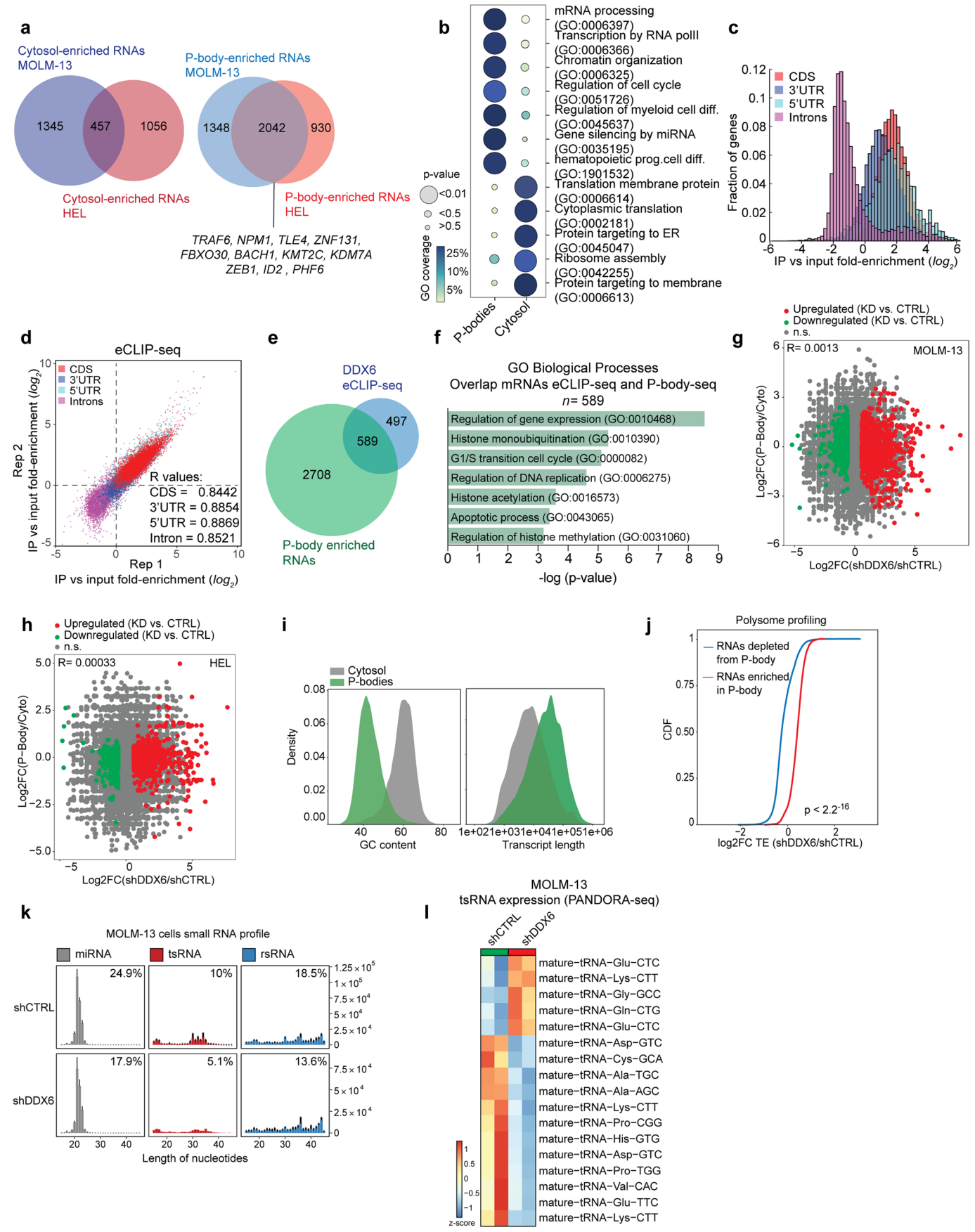

Extended Data Fig. 7 | See next page for caption.

https://doi.org/10.1038/s41556-024-01489-6

Extended Data Fig. 7 | DDX6 sequesters translationally repressed mRNAs in P-bodies. (a) Venn diagrams showing overlap between (left) cytoplasmic mRNAs or (right) P-body-associated mRNAs (FC > 1.5, p < 0.05) in MOLM-13 cells and HEL cells. Shared P-body-enriched transcripts encoding genes with potential tumour-suppressive activity are listed. **(b)** GO enrichment analysis for shared P-body-enriched RNAs in MOLM-13 and HEL cells (n = 2042). Two-sided Fisher's exact test. **(c)** Histogram of region-based FC for DDX6 eCLIP-seq read density over size-matched input (FC > 2, padj < 0.05). **(d)** Scatter-plot indicating correlation between region-based fold enrichment of DDX6 eCLIP-seq datasets across biological replicates (n = 2 biologically independent samples per group). **(e)** Venn diagram showing the overlap between DDX6 eCLIP-seq targets and P-body-enriched RNAs (n = 2 biologically independent samples per group, FC > 2, padj < 0.05, Wald test with Benjamini–Hochberg correction) in MOLM-13 cells. **(f)** GO pathway enrichment analysis of DDX6-bound, P-body-enriched RNAs (n = 589) identified in (e). Two-tailed Fisher's exact test. **(g, h)** Scatter-plots showing lack of correlation between P-body enrichment and expression for transcripts upregulated in *DDX6* KD (g) MOLM-13 or (h) HEL cells. **(i)** GC content and length distribution for P-body-enriched vs cytosolic mRNAs. **(j)** Cumulative distribution function (CDF) plot showing translation rate (log2 FC) of P-body enriched and P-body-depleted mRNAs for shDDX6 vs. shCTRL cells. Two-sided Mann–Whitney U test. **(k)** Dynamic changes in small RNA distribution in MOLM-13 cells following DDX6 suppression (n = 2 biologically independent samples per group). **(l)** Heatmap showing expression levels of selected tsRNAs in control vs *DDX6* depleted MOLM-13 cells (n = 2 biologically independent samples per group).

https://doi.org/10.1038/s41556-024-01489-6

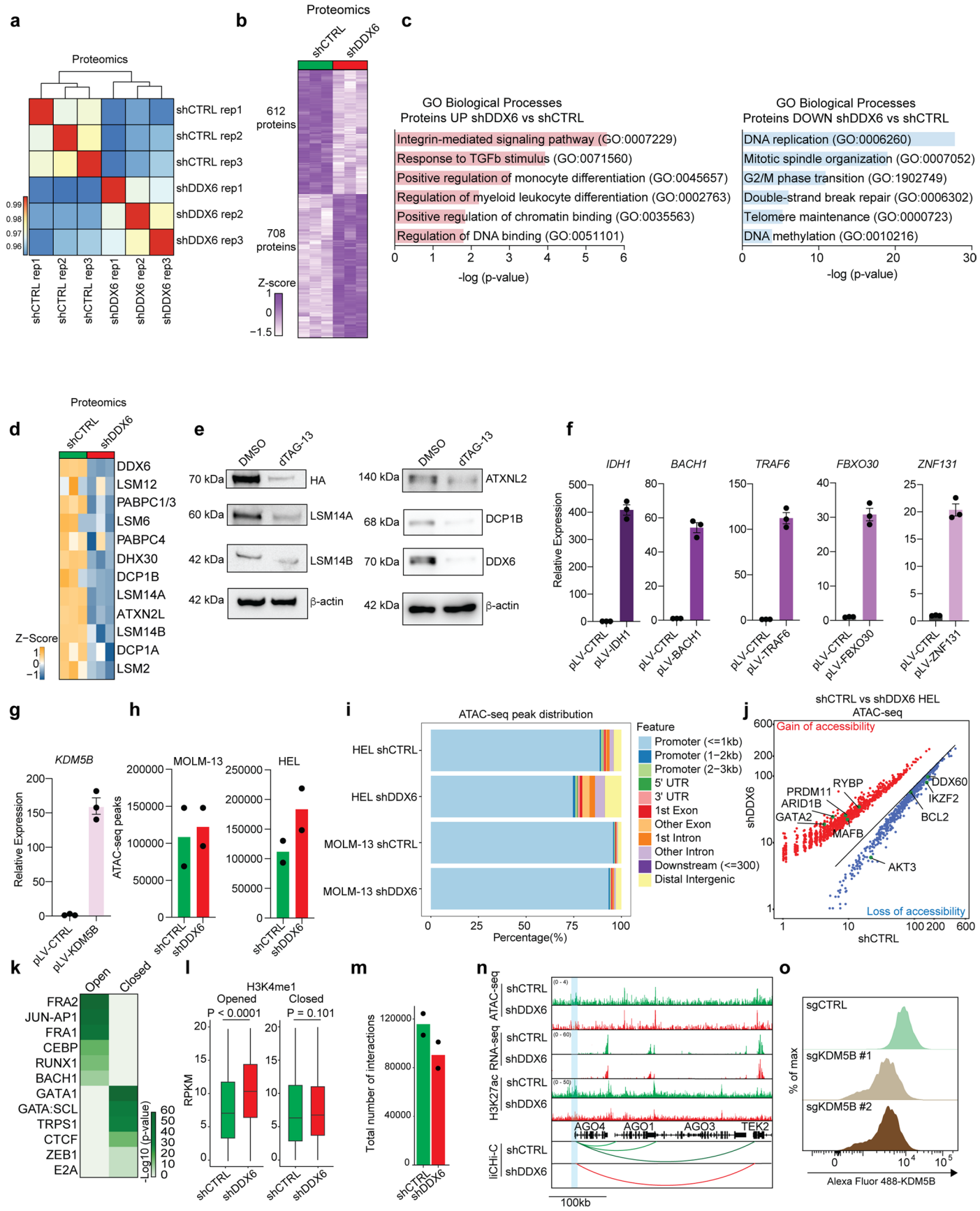

Extended Data Fig. 8 | See next page for caption.

https://doi.org/10.1038/s41556-024-01489-6

Extended Data Fig. 8 | Genome topology rewiring following *DDX6* depletion. **(a)** Correlation heatmap showing the correlation (r) values between proteomic samples ($n = 3$). Scale bar represents the range of the correlation coefficients (r) displayed. **(b)** Heatmap for differentially expressed proteins exhibiting a 1.5-fold or greater difference between control and *DDX6* KD MOLM-13 cells ($n = 3$). **(c)** Gene ontology analysis of upregulated and downregulated proteins (FC > 1.5; $p < 0.05$, Wald test with Benjamini–Hochberg correction) in shDDX6 compared to shCTRL MOLM-13 cells. **(d)** Heatmap showing downregulation of P-body-related proteins in *DDX6* KD MOLM-13 cells ($n = 3$ biologically independent samples per group). **(e)** Representative Western blots showing loss of P-body-related proteins upon DDX6 loss in DDX6-FKBP12^{F36V} MOLM-13 cells. $n = 3$ independent experiments. **(f, g)** qRT–PCR validation of tumour suppressor gene overexpression in MOLM-13 cells. ($n = 3$). **(h)** Total number of ATAC-seq peaks detected in control and *DDX6* KD (left) MOLM-13 or (right) HEL cells. **(i)** Genomic distribution of ATAC-seq peaks in control and *DDX6* KD HEL and MOLM-13 cells. **(j)** Scatter-plot showing ATAC-seq data for shCTRL and shDDX6 HEL cells ($n = 2$ biologically independent samples per group). Blue dots indicate genomic regions showing significantly decreased chromatin accessibility in *DDX6*-depleted cells (FC > 1.5, $p < 0.05$, Wald test with Benjamini–Hochberg correction; $n = 570$); red dots indicate genomic regions showing significantly increased chromatin accessibility in *DDX6*-depleted cells (FC > 1.5, $p < 0.05$; $n = 1044$). **(k)** TF motif enrichment analysis on shDDX6 gained and lost ATAC-seq peaks in HEL cells. **(l)** Increased H3K4me1 levels at loci of genes that gained chromatin accessibility and became upregulated after *DDX6* KD. Wilcoxon rank-sum test, shCTRL open ($n = 2026$), shDDX6 open ($n = 2045$), shCTRL closed ($n = 1024$), shDDX6 closed ($n = 1035$). Box centre line indicates median, box limits indicate upper (Q3) and lower quartiles (Q1), lower whisker is Q1 − 1.5 × IQR and upper whisker is Q3 + 1.5 × IQR. **(m)** Total number of promoter interactions detected by liCHi-C in control ($n = 2$) and *DDX6* KD ($n = 2$) MOLM-13 cells. **(n)** Gene tracks of ATAC-seq, RNA-seq, H3K27ac CUT&Tag, and liCHi-C data for the genomic region surrounding *AGO4*. Blue shadow highlights the gene promoter. Arcs represent significant promoter interactions (CHiCAGO score > 5). **(o)** Representative intracellular flow cytometry plot for KDM5B in control and *KDM5B* knockout MOLM-13 cells.

nature portfolio

Corresponding author(s): Bruno Di Stefano

Last updated by author(s): Jul 11, 2024

Reporting Summary

Nature Portfolio wishes to improve the reproducibility of the work that we publish. This form provides structure for consistency and transparency in reporting. For further information on Nature Portfolio policies, see our Editorial Policies and the Editorial Policy Checklist.

Statistics

For all statistical analyses, confirm that the following items are present in the figure legend, table legend, main text, or Methods section.

n/a	Confirmed	
☐	☒	The exact sample size (*n*) for each experimental group/condition, given as a discrete number and unit of measurement
☐	☒	A statement on whether measurements were taken from distinct samples or whether the same sample was measured repeatedly
☐	☒	The statistical test(s) used AND whether they are one- or two-sided *Only common tests should be described solely by name; describe more complex techniques in the Methods section.*
☐	☒	A description of all covariates tested
☐	☒	A description of any assumptions or corrections, such as tests of normality and adjustment for multiple comparisons
☐	☒	A full description of the statistical parameters including central tendency (e.g. means) or other basic estimates (e.g. regression coefficient) AND variation (e.g. standard deviation) or associated estimates of uncertainty (e.g. confidence intervals)
☐	☒	For null hypothesis testing, the test statistic (e.g. *F*, *t*, *r*) with confidence intervals, effect sizes, degrees of freedom and *P* value noted *Give P values as exact values whenever suitable.*
☒	☐	For Bayesian analysis, information on the choice of priors and Markov chain Monte Carlo settings
☒	☐	For hierarchical and complex designs, identification of the appropriate level for tests and full reporting of outcomes
☐	☒	Estimates of effect sizes (e.g. Cohen's *d*, Pearson's *r*), indicating how they were calculated

Our web collection on statistics for biologists contains articles on many of the points above.

Software and code

Policy information about availability of computer code

Data collection	Software used: FACSDiva v.8.0.1 (BD Biosciences), CytExpert 2.0 (Beckman Coulter), ZEN Blue 3.1 (Zeiss)
Data analysis	Software used: Prism 9.3.0 (GraphPad), FIJI (ImageJ 2.14.0/1.54f), FlowJo 10.8.2 (BD Biosciences), CytExpert 2.0 (Beckman Coulter), R 4.1.2 or higher (packages ggplot2 3.3.5, CHiCAGO 1.14.0, bedtools 2.30.0, DESeq2 1.22.2, ChIPSeeker, rGREAT, memes, JASPAR2022, Bowtie2 2.2.6, rtracklayer 1.54.0, MACS2 2.1.0, Trim Galore! 0.6.6, samtools 1.9, deeptools 3.2.1, STAR (version 2.5.1b or 2.7.9a), Xtail 1.2.0, Picard 2.26.3, featureCounts 2.0.3, MATLAB (R2023a)

For manuscripts utilizing custom algorithms or software that are central to the research but not yet described in published literature, software must be made available to editors and reviewers. We strongly encourage code deposition in a community repository (e.g. GitHub). See the Nature Portfolio guidelines for submitting code & software for further information.

Data

Policy information about availability of data

All manuscripts must include a data availability statement. This statement should provide the following information, where applicable:

- Accession codes, unique identifiers, or web links for publicly available datasets
- A description of any restrictions on data availability
- For clinical datasets or third party data, please ensure that the statement adheres to our policy

RNA–seq, ATAC-seq, eCLIP-seq, CUT&RUN, and CUT&Tag data that support the findings of this study have been deposited in the Gene Expression Omnibus (GEO)

under accession codes GSE224858, GSE261265, and GSE22463. Human data were mapped to the human reference genome (GRCh38). Raw data and the MaxQuant output for the proteomics have been deposited to the MassIVE database under the accession number MSV000090973. The files can be accessed through doi:10.25345/C5C824P7F with the password "proteomics". Previously published ChIP-seq data and polysome profiling data that were re-analyzed here are available under accession code GSM100358636 and GSE20222797. The human AML data were derived from the TCGA Research Network: http://cancergenome.nih.gov/. All other data supporting the findings of this study are available from the corresponding author on reasonable request.

Research involving human participants, their data, or biological material

Policy information about studies with human participants or human data. See also policy information about sex, gender (identity/presentation), and sexual orientation and race, ethnicity and racism.

Reporting on sex and gender	Some human samples were used in this study (please see Methods), obtained from both male and female AML patients. While sex-based differences were not a focus of this study, study findings apply to both sexes. Disaggregated sex and gender data was not collected.
Reporting on race, ethnicity, or other socially relevant groupings	AML patient samples #1, 3, and 4 are derived from females, AML patient sample #2 was derived from a male.
Population characteristics	AML patient #1 Gender: Female NGS mutations: DNMT3A c.2195T>G p.Phe732Cys (VAF45%), FLT3 c.1815_1816ins24 p.Tyr599_Pro606dup (VAF 46%), IDH1 c.394C>T p.Arg132Cys (VAF54%) Cytogenetics: 46, XX,del(7)(q21)[11]/45,XX,+8,-15,-17,-21,+mar[3]/46,XX AML patient #2 Gender: Male NGS mutations: NRAS, DNMT3A, TET2, KRAS, FLT3 (TKD), U2AF1, BCOR Cytogenetics: 46, XY AML patient #3 Gender: Female NGS mutations: DNMT3A (R882H), IDH2 (R140Q), KIT (M541L), KRAS (A146T), RUNX1 (D198N) Cytogenetics: 47, XX AML patient #4 Gender: Female NGS mutations: FLT3 (ITD), KIT (M541L), TET2 (V1718L), WT1 (A382fs) Cytogenetics: 46, XX
Recruitment	Primary AML samples from the peripheral blood or bone marrow were obtained during routine diagnostic procedures from the Hospital Clinic of Barcelona, Barcelona, Spain, or Baylor College of Medicine, Houston, USA, after informed consent from patients. Patients were otherwise not specifically recruited or compensated.
Ethics oversight	This study was approved by the Institutional Ethical Review Board of the Hospital Clinic of Barcelona (HCB/2018/0020) or the Institutional Review Board of Baylor College of Medicine (H-7122/H-3343/H-18245).

Note that full information on the approval of the study protocol must also be provided in the manuscript.

Field-specific reporting

Please select the one below that is the best fit for your research. If you are not sure, read the appropriate sections before making your selection.

☒ Life sciences ☐ Behavioural & social sciences ☐ Ecological, evolutionary & environmental sciences

For a reference copy of the document with all sections, see nature.com/documents/nr-reporting-summary-flat.pdf

Life sciences study design

All studies must disclose on these points even when the disclosure is negative.

Sample size	For all experiments, sample size was determined based on preliminary experiments or similar experiments in previously published literature (e.g. Prieto et al. Nat Cancer. 2021 Jul; 2: 741–757; Chavez et al. Nat Commun. 2023; 14: 2290; Paris et al. Cell Stem Cell . 2019 Jul 3;25(1):137-148.e6.)
Data exclusions	No data were excluded from this study.
Replication	All attempts to independently reproduce experiments were sucessful, (typically reproduced at least 3 times, with multiple biological replicates each time), except for large-scale sequencing assays (e.g., RNA-seq, proteomics, polysome profiling, low input capture Hi-C), which were cost-prohibitive to repeat independently, but were performed using multiple biological replicates.

Randomization	For in vivo experiments, age and gender-matched animals were randomly allocated into experimental groups. Randomization was irrelevant and not performed for in vitro experiments with cultured cells.
Blinding	Investigators were blinded for counting analyses (e.g. P-body counting, smFISH analysis, colony counting). However, in general, blinding was not performed for this study, as investigators who performed experiments were also acquiring and analyzing data.

Reporting for specific materials, systems and methods

We require information from authors about some types of materials, experimental systems and methods used in many studies. Here, indicate whether each material, system or method listed is relevant to your study. If you are not sure if a list item applies to your research, read the appropriate section before selecting a response.

Materials & experimental systems

n/a	Involved in the study
☐	☒ Antibodies
☐	☒ Eukaryotic cell lines
☒	☐ Palaeontology and archaeology
☐	☒ Animals and other organisms
☒	☐ Clinical data
☒	☐ Dual use research of concern
☒	☐ Plants

Methods

n/a	Involved in the study
☒	☐ ChIP-seq
☐	☒ Flow cytometry
☒	☐ MRI-based neuroimaging

Antibodies

Antibodies used	The following antibodies were used for staining of cell surface markers: APC-Annexin V (1:300) (BioLegend cat. no. 640920), APC-anti-human CD123 (1:300) (BioLegend cat. no. 306011), APC-anti-human CD61 (1:300) (BioLegend cat. no. 336411), APC anti-rat CD90/mouse CD90.1 (1:200) (BioLegend cat. no. 202526), FITC-anti-human CD41 (1:300) (BioLegend cat. no. 303703), APC-anti-human-HLA-ABC (1:300) (BD Biosciences cat. no. 555555), FITC-anti-human HLA-ABC (1:300) (BD Biosciences cat. no. 560965), PE-anti-human CD33 (1:300) (BD Biosciences cat. no. 555333), APC-anti-mouse CD45 (1:300) (BD Biosciences cat. no. 559864), APC-anti-mouse Gr-1 (1:300) (BioLegend cat. no. 108411), Pacific Blue-Annexin V (1:300) (Thermo Fisher cat. No. A35136), Pacific Blue anti-mouse CD45.2 (1:300) (BioLegend cat. no. 109819), Pacific Blue-anti-mouse CD3 (1:300) (BioLegend cat. no. 100213), Pacific Blue-anti-Gr-1 (1:300) (BioLegend cat. no. 108429), Pacific Blue-anti-CD19 (1:300) (BioLegend cat. no. 115526), Pacific Blue-anti-CD11b (1:300) (BioLegend cat. no. 101223), Brilliant Violet 711-anti-mouse Sca-1 (1:300) (BioLegend cat. no. 108131), APC-anti-mouse Ter119 (1:300) (BioLegend cat. no. 116211), FITC-anti-mouse CD45.1 (1:300) (BioLegend cat. no. 110705), FITC-anti-mouse CD71 (1:300) (Invitrogen cat. No. 110711), FITC-anti-CD48 (1:300) (BioLegend cat. no. 103403), PE/Cy7-anti-mouse CD11b (1:300) (BioLegend cat. no. 101216), PerCP/Cy5.5-anti-mouse CD19 (1:300) (BioLegend cat. no. 1155335), PerCP/Cy5.5-anti-mouse/human CD11b (1:300) (BioLegend cat. no. 101227), PerCP/Cy5.5-anti-mouse Gr-1 (1:300) (BioLegend cat. no. 108427), PerCP/Cy5.5-anti-mouse CD3 (1:300) (BioLegend cat. no. 100217), PE-anti-mouse CD150 (1:300) (BioLegend cat. no. 115903), PE-anti-mouse CD3 (1:300) (BioLegend cat. no. 100205), APC-anti-mouse c-Kit (1:300) (BioLegend cat. no. 105811), APC/Fire-750-anti-mouse CD16/32 (1:300) (BioLegend cat. no. 101317), Alexa Fluor 700-anti-mouse CD48 (1:300) (BioLegend cat. no. 103425), and PE/Cy7-anti-mouse CD34 (1:300) (BioLegend cat. no. 152217). The following antibodies were used for intracellular flow cytometry: APC-anti-FLAG (1:300) (BioLegend cat. no. 637307), FITC-anti-human CD68 (1:200) (BioLegend cat. no. 333805), rabbit anti-human DDX6 (1:400) (Novus Biologicals cat. no. NB-200-192), rabbit anti-human KDM5B (1:300) (Abcam cat.no. ab181089), Alexa Fluor 488-donkey anti-rabbit IgG (H+L) (1:400) (Invitrogen cat. no. A21206), Alexa Fluor 594-donkey anti-rabbit IgG (H+L) (1:400) (Invitrogen cat. no. A21207), Alexa Fluor 647-donkey anti-rabbit IgG (H+L) (1:400) (Invitrogen cat. no. A31573), Alexa Fluor 647-goat anti-rabbit IgG (1:200) (Invitrogen cat. no. A21244), Alexa Fluor 594-donkey anti-mouse IgG (1:400) (Invitrogen cat. No. A21203). For intracellular staining of Ki-67, cells were fixed and permeabilized using Transcription Factor Buffer Set (BD Biosciences cat. no. 562574), according to manufacturer's instructions, followed by staining with FITC-anti-mouse/human Ki-67 (1:300) (BioLegend cat. no.151211).
Validation	All antibodies used had validation data shown on the manufacturer's website, showing target species, target protein, and application. Additionally, BioLegend antibodies came with the promise that "each lot of this product is quality control tested by immunofluorescent staining with flow cytometric analysis". Abcam antibodies had a "Product promise tested" guarantee. Novus antibodies were backed by a "100% guarantee". In many cases, the antibodies were also used by others in previous peer-reviewed publications. In some cases (e.g., DDX6), we validated antibodies using genetic knockout or knockdown of the protein target (e.g., CRISPR KO, CRISPRi, shRNA).

Eukaryotic cell lines

Policy information about cell lines and Sex and Gender in Research

Cell line source(s)	HEL DSMZ # ACC 11), SKM-1 (DSMZ # ACC 547), MOLM-13 (DSMZ # ACC 554), MV411 (DSMZ # ACC 102), HL-60 cells (DSMZ # ACC 3), and HEK293T (DSMZ # ACC 635) were purchased from DSMZ cell line bank. Platinum-E cells were purchased from Cell Biolabs (RV-101). Lenti-X cells were purchased from Takara Bio (632180). We thank S. Doulatov for the hiPSC-derived CD34+ cells, D. Lacorazza for the THP-1 cells (ATCC # TIB-202), and D. Nakada for the MOLM-13-Cas9 cells.

Authentication	HEL, SKM-1, MOLM-13, MV411, HL-60, and 293T cells were authenticated by DSMZ through short tandem repeat (STR) DNA typing. THP-1 cells were authenticated at the Cytogenetics and Cell Authentication Core at M.D. Anderson Cancer Center, also through STR DNA typing. We did not authenticate the other cell lines used in this study (i.e. Platinum-E cells, HPC7 cells, hiPSC-derived CD34+ cells, Lenti-X cells, MOLM-13-Cas9 cells).
Mycoplasma contamination	Cells were confirmed negative for mycoplasma contamination weekly using a Mycoplasma PCR Detection Kit (Applied Biological Materials).
Commonly misidentified lines (See ICLAC register)	No commonly misidentified cell lines were used in this study.

Animals and other research organisms

Policy information about studies involving animals; ARRIVE guidelines recommended for reporting animal research, and Sex and Gender in Research

Laboratory animals	Ddx6fl/fl mice were generated using CRISPR/Cas9-initiated HDR in C57BL/6J background mouse embryos. LoxP sequences were inserted in introns 2 and 3 of the Ddx6 locus using single-stranded oligodeoxynucleotides. The following sgRNAs were used for targeting: sgRNA intron2: GGGTACTGCGCCAAACTAGA and sgRNA intron3: TAAGGTTATGATATGCAGCT. Ddx6fl/fl mice were crossed with Mx1-Cre mice (Jackson Laboratory strain # 003556) or Rosa26-ERT2-Cre mice (Jackson Laboratory strain # 008463) to generate mice with inducible knockout of Ddx6 in hematopoietic cells (Mx1-Cre/Ddx6fl/fl) or in all tissues (Rosa26-ERT2-Cre/Ddx6fl/fl), respectively. To induce Mx1-Cre-mediated Ddx6 deletion in vivo, 250 µg of poly (I:C) (Sigma-Aldrich cat. no. P1530-100MG) was administered to mice via intraperitoneal (i.p.) injection, every other day for 6 days. To induce Rosa26-ERT2-Cre-mediated Ddx6 deletion, 2 mg of tamoxifen was administered to mice via i.p. injection, every day for 5 days. C57BL/6J (Jackson strain # 000664), CD45.1 (Jackson strain # 002014), and NSG (Jackson strain # 005557, kind gift of Jason Yustein lab and Maksim Mamonkin lab) mice were used as recipients for transplantation experiments. All mice used in this study were 6-12 weeks old at the start of experiments. Mice were maintained under a standard 12 h/12 h light/dark cycle, at ambient temperature and humidity.
Wild animals	Study did not involve wild animals.
Reporting on sex	Experiments were performed using sex and age-matched mice (mice of both sexes were used, sex was determined by visual examination of genital regions), ranging from 6-12 weeks old.
Field-collected samples	Study did not involve samples collected from the field.
Ethics oversight	All mice were maintained in specific pathogen-free (SPF) animal facilities, approved, and overseen by the Institutional Animal Care and Use Committee (IACUC) of Baylor College of Medicine (IACUC #AN-8464) or the Animal Care Committee of the Barcelona Biomedical Research Park (AMM2-17-0030/Daam 9667 and AMM2-22-0031/Daam11883).

Note that full information on the approval of the study protocol must also be provided in the manuscript.

Flow Cytometry

Plots

Confirm that:

☒ The axis labels state the marker and fluorochrome used (e.g. CD4-FITC).

☒ The axis scales are clearly visible. Include numbers along axes only for bottom left plot of group (a 'group' is an analysis of identical markers).

☒ All plots are contour plots with outliers or pseudocolor plots.

☒ A numerical value for number of cells or percentage (with statistics) is provided.

Methodology

Sample preparation	To detect surface markers, cells were first incubated with Fc blocker (anti-CD16/CD32) for 10 min on ice to prevent background staining. Cells were then stained with appropriate fluorophore-conjugated antibodies on ice, protected from light, for 15 min. After staining, DAPI or DRAQ7 was added where appropriate to mark dead cells. To measure apoptosis, cells were incubated at room temperature, protected from light, for 15-30 min with APC or Pacific Blue anti-Annexin V and DAPI or SYTOX AADvanced Dead Cell Stain. For intracellular staining, cells were fixed with 4% methanol-free formaldehyde for 15 min at room temperature, then permeabilized and blocked with 0.1% Triton-X containing 2% donkey serum. Cells were labeled with primary antibodies against the desired intracellular markers and then stained with fluorophore-conjugated secondary antibodies if needed.
Instrument	Samples were acquired on LSR-II, LSR-Fortessa, FACSCanto II (BD Biosciences), or CytoFLEX S (Beckman Coulter) or sorted on a FACSAria or Influx (BD Biosciences). All flow cytometry data were analyzed on FlowJo 10.8.2 (BD Biosciences) or CytExpert (Beckman Coulter).
Software	All data were acquired on flow cytometers or sorters using FACSDiva, then analyzed using FlowJo 10.8.2 (BD Biosciences) or

Software	CytExpert 2.0 (Beckman Coulter).
Cell population abundance	Post-sort purity of sorted cell populations was > 95%, and was determined by analyzing the sample on the same instrument immediately after sorting, using the same gates set for sorting.
Gating strategy	Cells were first gated to exclude dead cells, doublets, and debris on the basis of FSC and SSC. Viability dyes (i.e. DAPI or DRAQ7) were used to further exclude dead cells. Cells were therafter gated based on expression of marker(s) of interest. Gates indicating positive and negative are based on isotype controls and single color controls.

☒ Tick this box to confirm that a figure exemplifying the gating strategy is provided in the Supplementary Information.